

# Design, Optimization, and Experimental Characterization of a Novel Magnetically Actuated Finger Micromanipulator

by

**Mohammad Al Mashagbeh**

A thesis  
Presented to the University of Waterloo  
in Fulfillment of the  
Thesis Requirement for the Degree of  
**Doctor of Philosophy**  
in  
**Mechanical and Mechatronics Engineering**

Waterloo, Ontario, Canada, 2018

© Mohammad Al Mashagbeh 2018

## **Author's Declaration**

I hereby declare that I am the sole author of this thesis. This is a true copy of the thesis, including any required final revisions, as accepted by my examiners.

I understand that my thesis may be made electronically available to the public.

## Abstract

The ability of external magnetic fields to precisely control micromanipulator systems has received a great deal of attention from researchers in recent years due to its off-board power source. As these micromanipulators provide frictionless motion, and precise motion control, they have promising potential applications in many fields. Conversely, major drawbacks of electromagnetic micromanipulators, include a limited motion range compared to the micromanipulator volume, the inability to handle heavy payloads, and the need for a large drive unit compared to the size of the levitated object, and finally, a low ratio of the generated magnetic force to the micromanipulator weight. To overcome these limitations, we designed a novel electromagnetic finger micromanipulator that was adapted from the well-known spherical robot.

The design and optimization procedures for building a three Degree of Freedoms (DOF) electromagnetic finger micromanipulator are firstly introduced. This finger micromanipulator has many potential applications, such as cell manipulation, and pick and place operations. The system consists of two main subsystems: a magnetic actuator, and an electromagnetic end-effector that is connected to the magnetic actuator by a needle. The magnetic actuator consists of four permanent magnets and four electromagnetic coils that work together to guide the micromanipulator finger in the  $xz$  plane. The electromagnetic end-effector consists of a rod shape permanent magnet that is aligned along the  $y$  axis and surrounded by an electromagnetic coil.

The optimal configuration that maximizes the micromanipulator actuation force, and a closed form solution for micromanipulator magnetic actuation force are presented. The model is verified by measuring the interaction force between an electromagnet and a permanent magnet experimentally, and using Finite Element Methods (FEM) analysis. The

results show an agreement between the model, the experiment, and the FEM results. The error difference between the FEM, experimental, and model data was  $0.05 N$ .

The micromanipulator can be remotely operated by transferring magnetic energy from outside, which means there is no mechanical contact between the actuator and the micromanipulator. Moreover, three control algorithms are designed in order to compute control input currents that are able to control the position of the end-effector in the  $x$ ,  $y$ , and  $z$  axes. The proposed controllers are: PID controller, state-feedback controller, and adaptive controller. The experimental results show that the micromanipulator is able to track the desired trajectory with a steady-state error less than  $10 \mu m$  for a payload free condition.

Finally, the ability of the micromanipulator to pick-and-place unknown payloads is demonstrated. To achieve this objective, a robust model reference adaptive controller (MRAC) using the MIT rule for an adaptive mechanism to guide the micromanipulator in the workspace is implemented. The performance of the MRAC is compared with a standard PID controller and state-feedback controller. For the payload free condition, the experimental results show the ability of the micromanipulator to follow a desired motion trajectory in all control strategies with a root mean square error less than  $0.2 mm$ . However, while there is payload variation, the PID controller response yields a non smooth motion with a large overshoot and undershoot. Similarly, the state-feedback controller suffers from variability of dynamics and disturbances due to the payload variation, which yields to non-smooth motion and large overshoot. The micromanipulator motion under the MRAC control scheme conversely follows the desired motion trajectory with the same accuracy. It is found that the micromanipulator can handle payloads up to  $75$  grams and it has a motion range of  $\pm 15 mm$  in all axes.

## Acknowledgements

I would like to take this opportunity to first and foremost thank God for being my strength and guidance in the completion of this work. I thank him for the gift of life and health. Without him I would not have had the physical ability to successfully complete this thesis.

I would like to express my deep and sincere gratitude to my supervisor, Prof. Mir Behrad Khamesee for the continuous and positive support during my Ph.D study. His patience, guidance and effort were very crucial to keep me focused and motivated. I attribute the level of my Doctoral degree to his encouragement, effort, and kind support. Besides my advisor, I would like to thank the rest of my thesis committee: Prof. William Melek, Prof. Soo Jeon, Prof. Eihab Abdel-Rahman, and Prof. Arun Misra for reviewing and offering insightful comments on this thesis.

I owe a debt of gratitude to my colleagues and office mates at the University of Waterloo for their encouragement and support throughout my studies. To my friends scattered around the world, thank you very much for being there whenever I needed a friend.

Lastly, a special thanks to my parents for all the moral support and the amazing chances they have given me during my life. I would not be where I am today and who I am today without their love, care, help and support. You are the best parents in this world and I always owe my success to you. Another special thanks to my wife, Heba, and to my little angel, my daughter Katya, for inspiring me and for their patience and tolerance during this journey and for being the greatest motivation for finishing this dissertation. Another big thanks for my parents-in-laws who took care of my daughter during my and my wife Ph.D comprehensive exams. To my brothers, sisters and family, thank you so much for being so supportive during my study and pushing me towards achieving my goals. You are my inspiration, and I hope to make you all proud.

## Examining Committee

The following served on the examining committee for this thesis. The decision of the examining committee is by majority vote.

	Name	Title
External Examiner:	Arun Misra	Professor
Supervisor:	Mir Behrad Khamesee	Professor
Internal Member:	William Melek	Professor
Internal Member:	Soo Jeon	Associate Professor
Internal-external Member:	Eihab Abdel-Rahman	Professor

## Dedication

I dedicate my dissertation work to my family and friends. A special feeling of gratitude to my loving parents, my lovely daughter *Katya*, and my special wife, who have supported me during my PhD journey. I hope that this accomplishment makes you very proud of me.

# Table of Contents

<b>List of Tables</b>	<b>xii</b>
<b>List of Figures</b>	<b>xiii</b>
<b>1 Introduction</b>	<b>1</b>
1.1 Background . . . . .	1
1.2 Shortcomings and Motivation . . . . .	3
1.3 Objectives . . . . .	4
1.4 Thesis Contributions . . . . .	5
1.5 Thesis Outline . . . . .	5
<b>2 Micromanipulation Using Electromagnetic Actuation</b>	<b>7</b>
2.1 Introduction to Micromanipulation . . . . .	7
2.2 Electromagnetic Micromanipulation . . . . .	12
2.3 Introduction to Magnetic Field and Magnetic Force . . . . .	14
2.4 Magnetic Levitation . . . . .	16



2.4.1	Magnetic Levitation Benchmark . . . . .	17
2.5	Finger Mechanism . . . . .	21
<b>3</b>	<b>System Overview</b>	<b>24</b>
3.1	Introduction . . . . .	24
3.2	System Overview . . . . .	24
3.3	Micromanipulator Design Components . . . . .	26
3.3.1	Magnetic Drive Rotational Actuator . . . . .	26
3.3.2	Magnetic Drive Linear Actuator . . . . .	30
3.4	Micromanipulator Kinematics . . . . .	30
3.5	Micromanipulator Jacobian . . . . .	32
3.6	Micromanipulator Dynamics . . . . .	33
3.7	Micromanipulator Workspace Calculations . . . . .	35
3.8	Conclusion . . . . .	37
<b>4</b>	<b>Analytical Modeling and Optimization</b>	<b>38</b>
4.1	Introduction . . . . .	38
4.2	Magnetization Configuration . . . . .	39
4.3	Magnetic Field Calculations . . . . .	40
4.3.1	Magnetic Field Calculations Generated by Electromagnetic Coils . . . . .	40
4.3.2	Magnetic Field Calculations Generated by Permanent Magnets . . . . .	42

4.4	Magnetic Force Calculations . . . . .	43
4.5	Optimization . . . . .	44
4.6	Magnetic Force Modeling . . . . .	50
4.7	Conclusion . . . . .	57
<b>5</b>	<b>Controller Design</b>	<b>58</b>
5.1	Introduction . . . . .	58
5.2	PID Controller . . . . .	60
5.2.1	Electromagnetic Force linearization . . . . .	61
5.2.2	PID Controller Design in the $z$ Axis . . . . .	63
5.2.3	PID Controller Design in the $x$ Axis . . . . .	64
5.2.4	PID Controller Design in the $y$ Axis . . . . .	67
5.3	State-Feedback Controller . . . . .	68
5.4	Adaptive Controller . . . . .	70
<b>6</b>	<b>Results and Validations</b>	<b>73</b>
6.1	Model Validations . . . . .	73
6.2	Force Measurement Results . . . . .	75
6.3	Design Advantages . . . . .	78
6.4	Position Tracking without payload variations . . . . .	79
6.4.1	Simulation Results . . . . .	79

6.4.2	Experimental Setup . . . . .	81
6.4.3	PID Controller Experimental Results . . . . .	82
6.4.4	Workspace Analysis . . . . .	87
6.4.5	Frequency Domain Analysis . . . . .	87
6.5	Position Tracking with payload variations . . . . .	90
6.5.1	PID Controller Experimental Results . . . . .	90
6.5.2	State-Feedback Controller Experimental Results . . . . .	92
6.5.3	Adaptive Controller Experimental Results . . . . .	95
6.5.4	Comparison . . . . .	96
6.5.5	Adaptive Controller using the MIT Rule . . . . .	97
6.6	Load Capacity Analysis . . . . .	100
<b>7</b>	<b>Conclusions and Recommendations</b>	<b>102</b>
7.1	Conclusions . . . . .	102
7.2	Recommendations . . . . .	105
	<b>APPENDICES</b>	<b>106</b>
<b>A</b>	<b>The Shell Method Calculations</b>	<b>107</b>
<b>B</b>	<b>The Micromanipulator CAD Drawing</b>	<b>109</b>
	<b>Letter of Copyright Permissions</b>	<b>110</b>
	<b>References</b>	<b>111</b>

# List of Tables

2.1	Summary of advantages and disadvantages of the actuation methods used to drive micromanipulators. . . . .	11
4.1	Summary of the optimization results . . . . .	50
6.1	Dimension and specifications of experimental setup. . . . .	76
6.2	Performance comparison in $x$ , $y$ , and $z$ motion. . . . .	87
6.3	Comparison of performance criteria using PID and MRAC controllers. . . . .	98

# List of Figures

2.1	Several actuation methods for driving micromanipulators. . . . .	9
2.2	Cylindrical frameless VCA. . . . .	13
2.3	Magnetic levitation ball system . . . . .	18
2.4	Schematic representation of the Maglev wrist proposed by Salcudean . . .	19
2.5	PowerMouse, a desktop magnetically levitated haptic interface . . . . .	20
2.6	Schematic of a magnetic drive unit developed at MagLev Microrobotics Laboratory. . . . .	20
2.7	Structure of the finger mechanism proposed by Nakamura in 2000. . . . .	22
3.1	CAD drawing of the proposed micromanipulator. . . . .	25
3.2	Photograph of the proposed micromanipulator. . . . .	26
3.3	Main components of the proposed micromanipulator. . . . .	27
3.4	Different configurations of the magnetic actuator. . . . .	28
3.5	Magnetic flux density norm ( <i>Tesla</i> ) for different materials configurations. .	29
3.6	Schematic of the magnetic drive linear actuator. . . . .	30

3.7	Kinematic of the proposed micromanipulator (Right view). . . . .	30
3.8	Kinematic of the proposed micromanipulator (Top view). . . . .	31
3.9	Free body diagram of the finger micromanipulator mechanism. . . . .	34
3.10	Three dimensional workspace representation of the finger micromanipulator mechanism. . . . .	36
4.1	Magnetization vector configuration. . . . .	40
4.2	Magnetic field calculation generated by electromagnetic coil. . . . .	41
4.3	Magnetic field calculation generated by permanent magnet. . . . .	42
4.4	Schematic diagram of electromagnetic coil and permanent magnet configu- ration. . . . .	44
4.5	Magnetic force versus magnet ( $\alpha$ ) and coil ( $\gamma$ ) geometry ratios. . . . .	46
4.6	Magnetic force versus coil geometry ratios $\alpha$ and $\beta$ . . . . .	48
4.7	Magnetic force versus air gap for AWG26 at 1 A. . . . .	51
4.8	Magnetic force versus air gap for AWG22 at 2.52 A. . . . .	52
4.9	Magnetic force error for AWG26 at 1 A. . . . .	53
4.10	Magnetic force error for AWG22 at 2.52 A. . . . .	53
4.11	Magnetic force versus axial air gap and excitation current. . . . .	54
4.12	Magnetic force versus axial air gap for different excitation currents. . . . .	55
4.13	Magnetic force versus excitation current at different axial air gaps. . . . .	56
5.1	Schematic of the position control loop. . . . .	60

5.2	Electromagnetic force experimental results. . . . .	62
5.3	Magnetic flux simulation. . . . .	62
5.4	Free body diagram in the $x$ axis. . . . .	64
5.5	Free body diagram in the $y$ axis. . . . .	67
5.6	Schematic of the control system including the PID controller. . . . .	68
5.7	Schematic of the MRAC. . . . .	72
6.1	Magnetic force versus axial air gap and excitation current. . . . .	74
6.2	Configuration of the magnetic actuator at all axial air gaps. . . . .	75
6.3	Force measurement experimental setup. . . . .	76
6.4	A comparison of magnetic force versus excitation current for different axial air gaps based on experimental, analytical, and FEM results. . . . .	77
6.5	General magnetic levitation system. . . . .	78
6.6	Simulation results in the $z$ axis for the whole workspace. . . . .	80
6.7	Simulation results in the $x$ axis for the whole workspace. . . . .	80
6.8	Simulation results in the $y$ axis for the whole workspace. . . . .	81
6.9	Schematic of the experimental setup. . . . .	82
6.10	Experimental results in the $z$ axis for the whole workspace. . . . .	83
6.11	Experimental results in the $z$ axis for a ramp input ( $2\text{ mm}$ increase). . . . .	83
6.12	Experimental results in the $z$ axis for a ramp input ( $4\text{ mm}$ increase). . . . .	84
6.13	Experimental results in the $x$ axis for the whole workspace. . . . .	84

6.14	Experimental results in the $z$ axis for a ramp input ( $2\text{ mm}$ increase).	85
6.15	Experimental results in the $x$ axis for a ramp input ( $4\text{ mm}$ increase).	85
6.16	Experimental results in the $y$ axis for the whole workspace.	86
6.17	Experimental results in the $z$ axis for $0.5\sin(\omega t)$ input.	88
6.18	Experimental results in the $z$ axis for $1\sin(\omega t)$ input.	88
6.19	Experimental results in the $z$ axis for $2\sin(\omega t)$ input.	89
6.20	Experimental Bode plot in the $z$ axis for $0.5\sin(\omega t)$ input.	89
6.21	Experimental Bode plot in the $z$ axis for $1\sin(\omega t)$ input.	90
6.22	Experimental Bode plot in the $z$ axis for $2\sin(\omega t)$ input.	90
6.23	Experimental results showing the performance of the PID controller without payload.	91
6.24	Experimental results showing the performance of the PID controller when payload is $25\text{ g}$ .	91
6.25	Experimental results showing the performance of the PID controller when payload is $75\text{ g}$ .	92
6.26	Experimental results showing the performance of the state-feedback control algorithm without payload.	93
6.27	Experimental results showing the performance of the state-feedback control algorithm when payload is $25\text{ g}$ .	94
6.28	Experimental results of the performance of the state-feedback control algorithm when payload is $75\text{ g}$ .	94



6.29	Experimental results showing the performance of the adaptive controller without payload. . . . .	95
6.30	Experimental results showing the performance of the adaptive controller when payload is 25 <i>g</i> . . . . .	96
6.31	Experimental results showing the performance of the adaptive controller when payload is 75 <i>g</i> . . . . .	96
6.32	Experimental results of MRAC and MRAC with modified MIT rule subjected to a sinusoidal input. . . . .	99
6.33	Pick-and-place experimental results when payload is 25 <i>g</i> . . . . .	100
6.34	Load capacity comparison. . . . .	101
B.1	Schematic CAD drawing of the micromanipulator. . . . .	109

# Chapter 1

## Introduction

### 1.1 Background

Micromanipulation is the technique of using small devices called micromanipulators to move and manipulate small objects. Micromanipulator systems have been proposed to address several applications and needs, especially those requiring high-precision, such as industrial and medical fields. There are several important design factors that need to be taken into consideration in order to develop effective and robust micromanipulation systems. These factors can be summarized as follows:

- Actuator type: choosing of actuator type is one of the important design factors in order to obtain the required force and motion at the micromanipulator end-effector. Micromanipulator systems can be driven using several actuation methods. The most common methods include: Motorized micromanipulators, hydraulic and pneumatic micromanipulators, piezoelectric micromanipulators, and electromagnetic micromanipulators. When selecting an actuator to drive micromanipulator systems, many

factors need to be taken into consideration such as coupling method, generated force, workspace (the micromanipulator workspace is defined as the set of all three dimensional points that can be reached by a reference point located on the micromanipulator end-effector), and motion accuracy.

- Actuation force: actuation force is an important design parameter and it plays a very important role in determining the micromanipulators applications and tasks.
- Workspace volume: although micromanipulator systems are used to interact with miniature objects, having a larger space of interaction is always preferable. In eye surgery for example, it is required to have a workspace of a  $25\text{ mm}$  diameter sphere, which corresponds to the interior volume of a human eye [1]. Similarly other surgeries require even larger workspace. Industrial micromanipulations in hazardous environments, on the other hand, require a manipulator with larger workspace. As a result, the volume of the workspace has a significant effect on the range and variety of applications that these micromanipulators can work with [2].
- Portability and weight: In many applications, a portable and light micromanipulator design is preferable to accomplish given tasks, therefore a large and bulky design is not desired.
- Controllability: controllability is a useful design tool, which means the micromanipulator can go from one point to another point smoothly, and follow the desired motion trajectory with almost the same accuracy. Controlling electromagnetic systems is not an easy task, due to the inherent nonlinearity of the magnetic field and force. As found in literature, one of the greatest challenges in development of electromagnetic systems is designing a robust control strategy.

## 1.2 Shortcomings and Motivation

Micromanipulator systems that are driven by electromagnetic actuators have several advantages over other types of actuation methods. Electromagnetic micromanipulators, on the other hand, suffer from the fact that they are difficult to model and control, in addition to limited motion range compared to the micromanipulator volume, and the requirement for a large drive unit compared to other types of actuation methods. The design of a portable magnetically actuated micromanipulator with a large workspace area and high output force is still a significant challenge for the development of these actuators for potential applications. This problem has motivated exploration of the possibility of building a novel magnetically actuated micromanipulator that is small and portable, produces no backlash, can move rapidly in different environments, and still has a large working space. In this work, the design and optimization procedures for building a portable magnetically actuated manipulator are presented. The development and experimental characterization for building the system are also introduced.

The proposed magnetic micromanipulator has 3 DOF, and consists of a combination of electromagnetic coils and permanent magnets that can move the micromanipulator to perform specific tasks. The magnetic force between a cylindrical permanent magnet and a cylindrical thick coil is usually found using the finite element method (FEM) or using numerical integration methods. In real-time applications, the use of complex numerical and integration calculations might affect the controller performance, especially in a magnetic system that has a fast response time. Therefore, part of this study focuses on finding the closed form model of the magnetic actuation force symbolically, so that the controller can execute the magnetic force faster and more efficiently. The magnetic force can be calculated faster, then fed back to the controller to find the required excitation current. Finally, as

controlling electromagnetic systems is very challenging, the last part of this work focuses on designing a robust control strategy to guide the micromanipulator in the workspace.

## 1.3 Objectives

This research project has been motivated by the increasing needs for multi-degree of freedom (M-DOF) electromagnetic micromanipulators that are capable of providing a precise force and motion control. The overall goal of the project is to design, optimize, and build a portable M-DOF magnetically actuated finger micromanipulator. This goal is accomplished by fulfilling the following research objectives:

- To develop a finger micromanipulator that can handle objects up to 75 *grams* at the end-effector.
- To design and fabricate a portable finger micromanipulator with a large workspace area compared to the micromanipulator volume.
- To optimize the design and the dimensions in order to maximize the generated magnetic force at the end-effector.
- To find the closed form model of the magnetic actuation force symbolically, so that the controller can execute the magnetic force faster and more efficiently.
- To develop a real-time control strategy to guide the micromanipulator in the workspace in the presence of payload at the end-effector tip.
- To investigate the use of the proposed micromanipulator in industrial applications.

## 1.4 Thesis Contributions

Designing and developing a novel and portable finger micromanipulator using electromagnetic actuation principles is the main goal of this thesis. The novelty of this work lies in the coupling of magnetic levitation systems with small-scale industrial manipulators. The design has many advantages over other designs presented in the literature as it has a smaller drive unit and larger workspace. In addition, the micromanipulator can be remotely operated by transferring magnetic energy from outside, which means there is no mechanical contact between the drive unit and the micromanipulator.

Use of complex numerical and integration calculations affects the controller performance especially in magnetic systems. Therefore, the second contribution of this thesis is developing a closed form model of the magnetic actuation force symbolically, so that the controller can execute the magnetic force faster and more efficiently.

For the third contribution of this thesis, a robust manipulator has been developed in which it can handle various payloads with unknown masses to address pick-and-place operations. By implementing an adaptive control algorithm, the controller guides the micromanipulator in the workspace smoothly, precisely, and independently of the payload.

## 1.5 Thesis Outline

This proposal is divided into seven chapters, structured as follows: Chapter 1 presents an overview of micromanipulation in general, with more focus on electromagnetic micromanipulation. Chapter 2 provides a literature review concerning micromanipulation using electromagnetic actuation. Chapter 3 provides detailed information about the system and the different components of the integrated system. In addition, this chapter outlines the

kinematic, jacobian and dynamic of the proposed micromanipulators. Chapter 4 describes the modeling portion and the optimization procedures for the proposed electromagnetic micromanipulator. Chapter 5 presents the controllers design, while Chapter 6 covers the experimental and simulation results. In addition, this chapter covers the validation of the obtained magnetic force model. Lastly, chapter 7 presents the thesis summary and recommendations.

# Chapter 2

## Micromanipulation Using Electromagnetic Actuation

### 2.1 Introduction to Micromanipulation

There are several actuation methods to drive micromanipulators found in the literature, the most common types include:

- Mechanical micromanipulators.
- Motorized micromanipulators.
- Hydraulic and pneumatic micromanipulators.
- Piezoelectric micromanipulators.
- Electromagnetic micromanipulators.



Mechanical micromanipulators have similar design to large scale robot arms that can move, rotate, and manipulate small objects. An example of mechanical micromanipulators is shown in Figure 2.1a. Motorized or ‘lead screw’ micromanipulators are used to produce incremental movements and rotations in one or more degrees of freedom. A general motorized micromanipulator consists of mechanical arms driven by motors in one or more axes. Position of the micromanipulator is controlled in the  $x$ ,  $y$ , or  $z$  directions using a step movement of a motorized lead screw actuator. Although motorized manipulators have been used to address several applications and needs, they still have some limitations and drawbacks in some applications [3]. An example of motorized micromanipulator is shown in Figure 2.1b. Generally, micromanipulators driven by conventional mechanical actuators and motorized lead screw actuators have some disadvantages, such as backlash, friction, and singularities due to gears and mechanical arms, which makes them non-ideal for use in micro-scale manipulation.

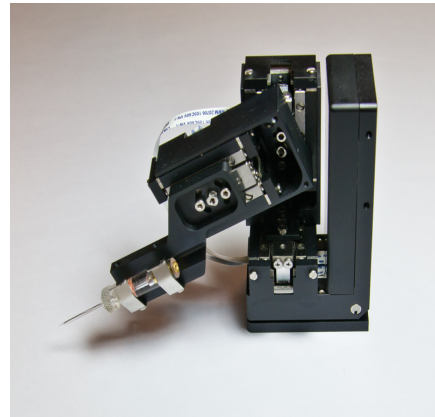
In hydraulic micromanipulators, the hydraulic power is used to guide and control the micromanipulator. Figure 2.1c shows an example of a hydraulic micromanipulator. Hydraulic micromanipulators provide high force to weight ratio [4] but suffer from slow response time and also a temperature drift which makes them less favourable in micro-scale applications. In the same way, micromanipulators driven by pneumatic actuators can provide a high actuation force and travel range [5, 6] but their fabrication is complex and costly, and they are bulky.

Piezoelectric micromanipulators (Figure 2.1d) provide a high actuation force and a fast response time [7], but have a short travel range and exhibit nonlinearity [8]. Also, the control and modeling of piezoelectric actuators is very complex because of their nonlinearity and hysteresis [9, 10]. Other actuation methods that can provide high force-to-weight ratios either suffer from high initial cost or nonlinearity (e.g. shape memory alloy actuators).



(a) Sutter instrument MM-33 micromanipulator. (b) Three-axis Motorized Micromanipulator. Image reproduced from [11].

Image reproduced from [12].



(c) Hydraulic joystick driven micromanipulator. (d) Miniature Piezo Micromanipulator. Image reproduced from [13].

Image reproduced from [14].

Figure 2.1: Several actuation methods for driving micromanipulators.

Electromagnetic micromanipulators composed of a combination of electromagnetic coils and permanent magnets, have been in the spotlight recently because of several advantages: they are small in size, contactless, frictionless, and electric motor-free, they also have low power consumption, and have wireless control features. The most important advantage

of magnetically actuated manipulators is that they can perform tasks in different environments, such as hazardous areas or fluid environments. Table 2.1 summarizes the advantages and disadvantages of the actuation methods used to drive micromanipulators.

Table 2.1: Summary of advantages and disadvantages of the actuation methods used to drive micromanipulators.

	<b>advantages</b>	<b>disadvantages</b>
<b>Mechanical micromanipulators</b>	High output force High output motion range	Backlash Friction
<b>Motorized micromanipulators</b>	High output force High output motion range	Backlash Friction Jumpy Movements
<b>Hydraulic micromanipulators</b>	High output force High travel range	Bulky design Temperature drift Slow response time
<b>Pneumatic micromanipulators</b>	High output force High travel range	Bulky design Fabrication is complex and costly
<b>Piezoelectric micromanipulators</b>	High actuation force Fast response time	Short travel range Nonlinearity and hysteresis Control and modeling is very complex
<b>Electromagnetic micromanipulators</b>	Contactless Frictionless Small in size High output force Fast response time Electric motor-free Low power consumption Wireless control feature	Workspace is small Control and modeling is hard Drive unit is very large compared to the micromanipulator weight

## 2.2 Electromagnetic Micromanipulation

Among all of the actuation methods mentioned before, electromagnetic actuation has advantages in terms of motion accuracy and actuating force [15]. In addition, no mechanical coupling such as gears is required and the micromanipulator can be controlled remotely [16], by applying external magnetic fields [17, 18]. Remotely controlled micromanipulators are more preferable in many applications as there is no contact between power supply and micromanipulator arms [19, 20]. In addition, the lack of mechanical gears eliminates backlash and friction [21], which makes electromagnetic actuation methods very suitable for micro-scale manipulation.

Electromagnetic actuation has been used very successfully in several applications and needs [22, 23, 24, 25, 26]. Generally, the electromagnetic actuator consists of a group of electromagnetic coils and permanent magnets. They might be stationary or moving, however, usually manipulator systems consist of a permanent magnet surrounded by stationary electromagnet coils. Using the electromagnetic actuation method, a magnetic drive unit generates magnetic energy in a small air gap to navigate the manipulator [27]. Foremost problems with this technique are the facts that they have a limited motion range [28], and they require large drive units.

There has been much research on micromanipulators and microrobot systems based on electromagnetic actuation principles in the literature. Choi et al. [29] developed a two dimensional space electromagnetic actuated microrobot using two pairs of Helmholtz and Maxwell coils. Xiao and Li presented an electromagnetic actuated *XY* micromanipulator [30] and an electromagnetic actuator [31] using a microdisplacement module. In similar work by Go et al. [32], an electromagnetic actuated microrobot was designed and fabricated to be used for manipulation of micro-particles. Most of the presented designs in the

literature, however, have limited motion range and low load capacity. Moreover, most of the proposed electromagnetic manipulators have a large drive unit that consists of a group of electromagnetic coils in a planar array, which limits the range of applications of these systems and restricts their use commercially.

Voice Coil Actuators (VCA) which are electromechanical linear devices that work based on Lorentz force, are well known as an example of electromagnetic actuators. VCA consist of two separate parts; the magnetic part and the solenoid part. VCA has one DOF either by moving the magnetic part or by moving the solenoid part. An example of a cylindrical VCA is shown in Figure 2.2.

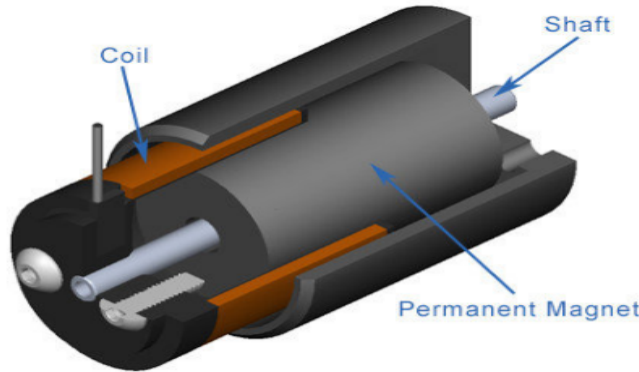


Figure 2.2: Cylindrical Frameless VCA. Image reproduced from [33].

In order to build a micromanipulator with more than one DOF using voice coil actuators, more than one VCA are needed to be linked together. This makes the micromanipulator design very bulky, not frictionless, and might create a backlash problems. In addition, VCA travel range is short which is not suitable for many applications such as pick and place operations. The workspace length of the VCA in Figure 2.2 is around  $0.5\text{ mm}$ , while the output force is around  $0.7\text{ N}$  and the VCA weight is around  $0.01\text{ kg}$ .

## 2.3 Introduction to Magnetic Field and Magnetic Force

Much research has been conducted on the use of external magnetic fields to control micromanipulators in the past decade. Magnetic repulsive or interaction forces can be used as an actuation method for micromanipulators. The main benefit of this technique is that it has no contact with the manipulator; this eliminates the backlash problems associated with gear-actuated manipulators or motorized lead screws actuators, and allows the manipulator to be controlled wirelessly [1, 34]. The magnetic force can be used for micro-scale applications, such as micro-machining, [35] and biomedical applications, such as cell manipulation [36]. On a larger scale, the magnetic force can be used to exert forces into environments or to manipulate large objects [37].

The source of the magnetic force applied to the manipulator (usually a permanent magnet material) can be produced by the use of electromagnetic coils or permanent magnets. In the former, the force is obtained by changing the distance between the electromagnetic coils and the manipulator or by changing the excitation current of the coils. Usually, the distance between the coil and the permanent magnet is fixed, and therefore the force is most commonly controlled by changing the excitation current. In such applications, the magnitude of the force depends on the gradient of the magnetic field and sequentially on the excitation current of the coil. In the latter, the only way to change the magnitude of the magnetic force between permanent magnets is by changing the distance between them. Therefore, this method is not widely used in the industry because of the difficulty associated with changing the distance between any two magnets, which requires mechanical moving parts that are usually driven by a motor for their operation.

The magnetic attraction or repulsive force in the magnetically-actuated manipulators is usually produced by the Lorentz force [38, 39, 40, 41, 42], or the dipole moment prin-

ciple [43]. Voice coil actuators are a well-known example of Lorentz force actuators. Because of these many advantages and potential applications, micromanipulation based on wirelessly-controlled magnetic force has recently become a popular topic in the literature. For example, two-pole magnetic tweezers [44] and three-pole magnetic tweezers [45] were designed to maneuver small magnetic probes inside living cells. Dkhil et al. [46] achieved high speed manipulation using a magnetic field to manipulate micro-objects. Niu et al. [47] used six orthogonally-aligned electromagnetic coils to wirelessly control a single magnetic bead. In [30], a 2 DOF micromanipulator for micro and nano manipulation was proposed. In most of the proposed systems, the manipulator workspace volume is small relative to the manipulator volume, and the ratio of generated magnetic force to manipulator weight is also small. However, a large and growing body of literature focuses on untethered magnetic manipulator systems, especially those that address medical applications. In these applications, a micromanipulator (a permanent magnet material) is guided inside the human body through an external magnetic field. Maxwell coils, which are capable of producing a uniform gradient field in a larger space than other kinds of coils, are usually placed around the human body to generate the required actuation and to guide the micromanipulator. This type of actuation consumes a low amount of energy, but the micromanipulator working area is also small relative to the volume of the system (micromanipulator and electromagnetic coils). Many industrial applications (e.g., tweezers) require non-contact manipulation: the manipulator needs to be able to hold, move, pick, and place small objects in a large working area. The Magnetic Levitation “MagLev” research team at the University of Waterloo has been working toward the goal of building small manipulator systems, based on magnetic principles, that can perform several types of manipulations in large working spaces. Khamesee, et al. [27] built a 3 DOF microrobot that can be remotely operated in an enclosed environment, using an external magnetic field that can



produce translational forces on the microrobot. The same research group proposed a novel magnetic-haptic micromanipulation platform; the authors developed and experimentally verified a mathematical force model of the magnetic actuation mechanism [48]. Motion control of these magnetically-actuated manipulators has been investigated and studied in other works [49, 50, 51]. A major problem associated with magnetically-actuated micromanipulators is that attaching force and motion sensors is impractical because of the size restrictions of these types of manipulators. Therefore, the University of Waterloo MagLev research team has proposed and experimentally verified new methodology to determine the position [52] and contact forces [53]. Furthermore, they have studied the arrangement of electromagnetic coils and the optimum structure of magnetically-actuated manipulators [54].

## 2.4 Magnetic Levitation

In recent years, there has been an increasing interest in the development of magnetic levitation technology. Magnetic levitation systems have demonstrated the capability of this technology in many fields, including medical applications [55, 3, 56], magnetic bearing [57, 58], industrial manipulation [59, 60], high-speed maglev trains [61], and teleoperation [48]. A variety of micromanipulator systems with various designs, applications, and drive types have been reported in the literature [62, 63, 64, 65, 30, 66, 67, 68, 69, 70, 71].

Magnetic levitation systems can be remotely operated, making them suitable for industrial manipulations such as pick-and-place operations which require a smooth motion in the working area without suffering from friction problems and singularities.

Magnetic levitation systems usually consist of a levitated robot in the 3D space that is guided by many electromagnetic coils. In literature, several studies have used the magnetic

levitation ball system which is a benchmark example of freely levitated systems [72, 73, 74]. In this system, electromagnetic coils produce a magnetic force to levitate an iron ball in the air. Although freely levitated robots have been used successfully in many applications, they suffer from some serious drawbacks, including limited manipulation with a motion range less than a few millimeters, the inability to handle heavy payloads more than 10 *grams*, and their incapability of applying large forces. Moreover, they require a large drive unit compared to the size of the levitated object.

One way to overcome these problems is to incorporate magnetically actuated micropositioning stage systems [75, 76, 77, 78]. They have higher payload capabilities and higher motion range but they consist of several moving parts which introduces friction problems and other constraints. To overcome this problem, a design that combines magnetic levitation and small-scale industrial manipulators was implemented. The novelty of this work lies in the coupling of magnetic levitation systems with small-scale industrial manipulators. The design has a levitated rod that was adapted from the well-known spherical robot design, and its lack of gears allows it to be controlled remotely without any contact between the levitated rod and the drive unit. The proposed manipulator consists of a drive unit, a levitated rod with permanent magnets fitted inside, and a position feedback sensor. The main advantage of this magnetically levitated manipulator compared to other magnetic levitation systems is that it can handle payloads up to 75 grams and it has a motion range of  $\pm 15$  *mm* in each axis.

### **2.4.1 Magnetic Levitation Benchmark**

The magnetic levitation ball system, which is a benchmark example of freely levitated systems, is shown in Figure 2.3 below. The system consists of an electromagnetic coil

carrying a current  $I$ , an iron ball with a mass  $m$ , separated by a distance  $h$ , with a position sensor for measuring the position of the iron ball. The system is nonlinear and unstable due to inherent nonlinearity in the electromagnetic force. Motion range of this system is very limited and many works have been reported in the literature to improve this system by adding more electromagnetic coils. Adding more electromagnetic coils increases the motion range but at the cost of additional complexity in terms of the control process and portability.

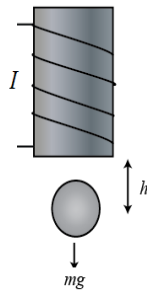
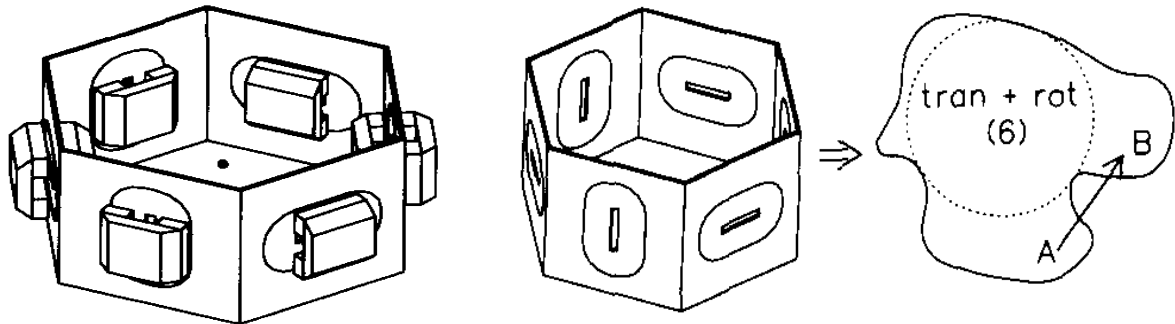


Figure 2.3: Magnetic levitation ball system

Early examples of research into designing magnetically actuated micromanipulators was proposed by [79]. The schematic representation of the ring and the end-effector is shown in Figure 2.4a, while the workspace representation is shown in Figure 2.4b. The system has been developed over time and refinements have been added to it. For example, a haptic interface, called PowerMouse (Figure 2.5) related to the system was proposed by the same research group [80] afterward.



(a) Ring schematic representation.

(b) Workspace representation.

Figure 2.4: Schematic representation of the Maglev wrist proposed by Salcudean [79].

The wrist consists of a hexagonal box structure containing flat copper coils and position sensing structure with mounted magnet assemblies. The device can be mounted to a robot or can be manipulated by hand. This 6 DOF electromagnetic manipulator can provide up to  $1\text{ mm}$  travel range. However, this system was implemented for very few applications due to its small positioning range and the design complexity. In many applications, a portable and light micromanipulator design is preferable to accomplish given tasks, therefore a large and bulky design is not desired.

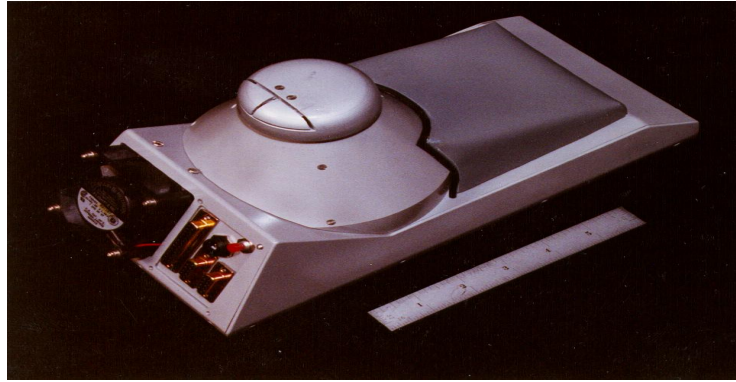


Figure 2.5: PowerMouse, a desktop magnetically levitated haptic interface

Another example of research into design of magnetically actuated micromanipulators was proposed by the magnetic levitation research team at the University of Waterloo [27]. The schematic design of the magnetic drive unit for this magnetically-actuated micromanipulator is shown in Figure 2.6.

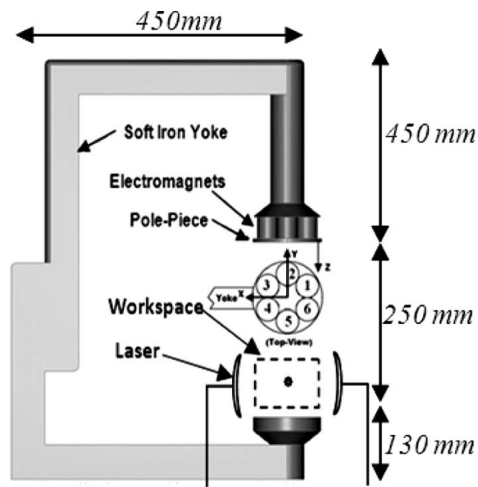


Figure 2.6: MagLev magnetic drive unit [48].

As shown in Figure 2.6, The magnetic drive unit of this magnetically-actuated mi-

micromanipulator is 830 *mm* long, 450 *mm* wide, with approximately 400 *mm* depth. The workspace volume of this magnetically-actuated micromanipulator is  $29 \times 29 \times 25 \text{ mm}^3$ . The system is employed for cell injections and cell micromanipulations. However, the ratio between drive unit volume to the system workspace volume needs to be decreased. In addition, having a large magnetic drive unit restricts the use of this micromanipulator for commercial use.

## 2.5 Finger Mechanism

Machining and handling of small objects are of great interest in the industry. Micromanipulators have proved to be the best choice for such applications. Micromanipulators may be classified according to type of the kinematics arrangement into serial multi-links micromanipulators, parallel multi-link micromanipulators, and finger micromanipulators. Finger design is the only mechanism that is capable of eliminating the backlash problems associated with multi-link micromanipulators. There are different designs proposed in the literature regarding finger mechanism micromanipulators. In (2000), Tatsuya Nakamura proposed the design of a finger micromanipulator (Figure 2.7) with a lever mechanism and magnetic actuators [81]. The finger micromanipulator mechanism is able to handle small mechanical parts.

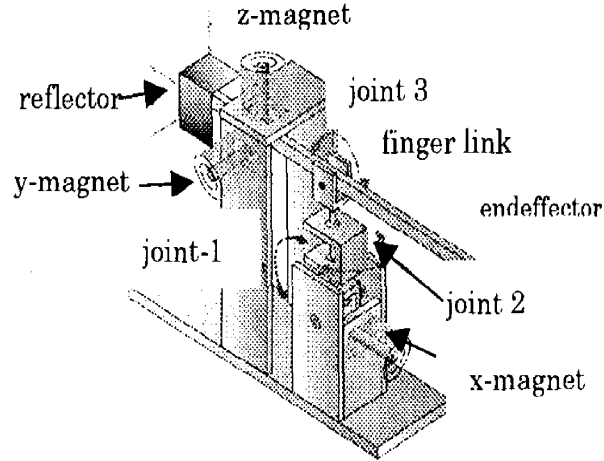


Figure 2.7: Structure of the finger mechanism proposed in [81].

The finger consists of two links, three joints, three electromagnetic coils, and three permanent magnets at each joint. Each permanent magnet and electromagnetic coil drive and rotate the mechanism in one DOF. The weight of the mechanism is  $1\text{ kg}$ , and the workspace is  $5 \times 5 \times 5\text{ mm}^3$ . The size of the mechanism including the magnetic drive unit is  $320 \times 110 \times 175\text{ mm}^3$ . However, there are certain problems with the use of the multi-link and multi-joint design. One of these is that this finger mechanism design is not able to eliminate the backlash problems associated with the joint link mechanism. Hence building a finger mechanism with fewer joints is desirable in the micro scale applications.

In 2007, Krishnan and Saggereet proposed a new design for a micromanipulator with multiple fingers that is capable for both gripping and positioning of micro-scale objects [82]. A major problem with this design is that it has a short travel range and is not capable in assembly of micro-scale components and devices [83].

There are other proposed designs in the literature, but either they are bulky, or have a small workspace, or they are not able to generate the required force at the end-effector tip. Designing a finger mechanism with fewer joints and links while still having a large workspace and large generated force at the end-effector tip is still a challenge for researchers. In this research, the ability of designing a portable finger mechanism that has 3 DOF and is still not bulky, and provides the required force for micro-scale applications in a large workspace is investigated.



# Chapter 3

## System Overview

### 3.1 Introduction

This chapter introduces the components of the micromanipulator system, and how they are organized in the design. Thereafter, the kinematics and dynamics modeling procedures of the micromanipulator are calculated. In addition, the transformation between the micromanipulator end-effector velocity and the joint velocity are presented in this chapter. Finally the micromanipulator workspace is found based on the micromanipulator geometry.

### 3.2 System Overview

The micromanipulator consists of a magnetic actuator and a finger mechanism. The proposed micromanipulator is a three DOF micromanipulator that moves along the  $x$  and  $z$  axes, and also moves linearly along the  $y$  axis. The finger consists of two concentric rods. The main rod is connected to the permanent magnets using a four way connector. Two

revolute joints are connected also to the main rod to allow the micromanipulator finger to rotate around the  $x$  and  $z$  axes. The drive unit consists of four stationary electromagnetic coils aligned with four moving permanent magnets (two permanent magnets with a fixed gap between them in the  $x$  and  $z$  directions). In addition, an axial electromagnetic coil is located around the main rod to allow the smaller rod (which is a permanent magnetic material) to move in the  $y$  direction. A simple CAD drawing and a photograph with all components of the proposed micromanipulator are shown in Figures 3.1 and 3.2 respectively.

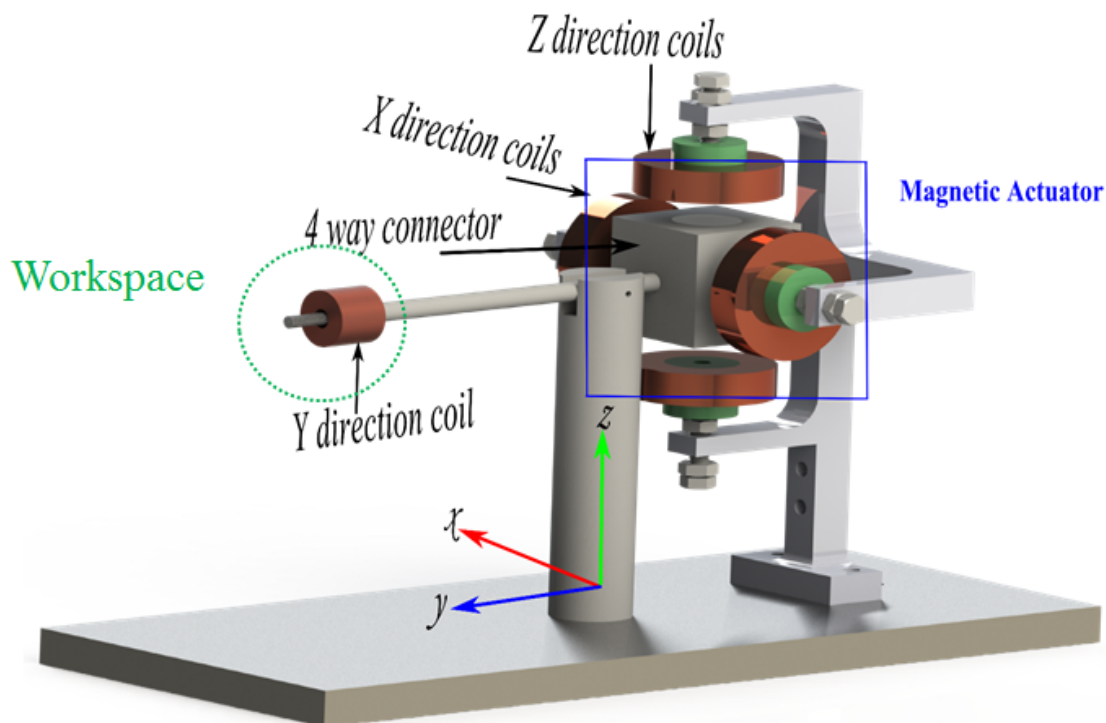


Figure 3.1: CAD drawing of the proposed micromanipulator.

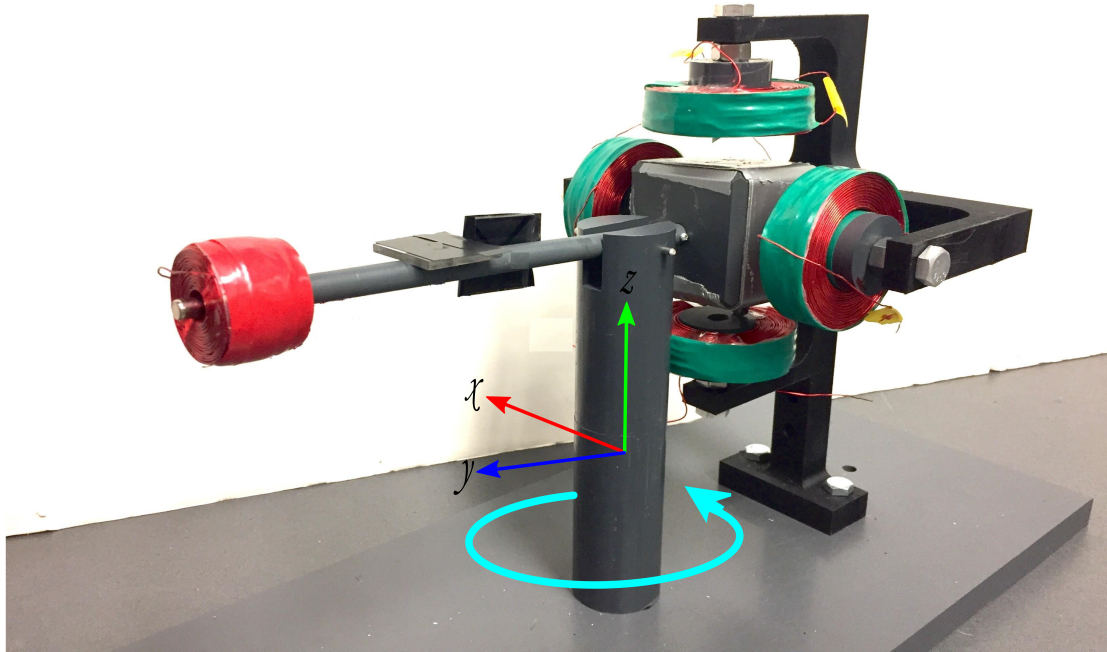


Figure 3.2: Photograph of the proposed micromanipulator.

### 3.3 Micromanipulator Design Components

The proposed micromanipulator with an optimized geometry, shown in Figure 3.3, has two main subsystems: a magnetic actuator and an electromagnetic end-effector connected to the magnetic actuator by a needle with length  $l$ .

#### 3.3.1 Magnetic Drive Rotational Actuator

The rotational magnetic actuator consists of four permanent magnets and four electromagnetic coils to guide the micromanipulator finger in the  $xz$  plane. The main objective of

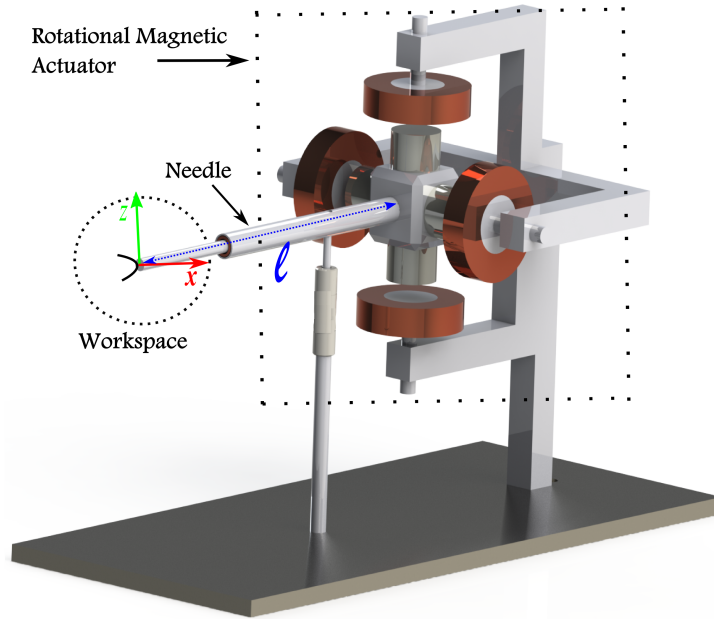
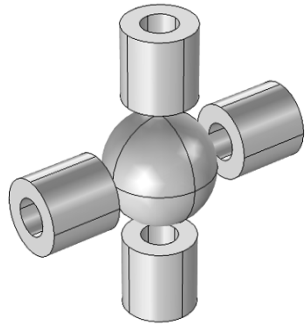


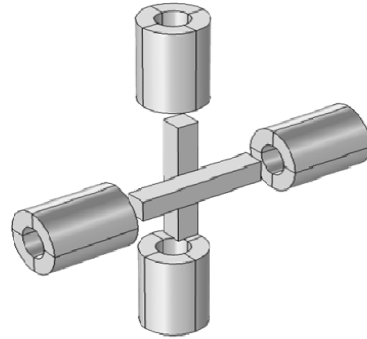
Figure 3.3: Main components of the proposed micromanipulator.

the magnetic actuator design is to produce the magnetic force required to lift and move the manipulator finger in the workspace. Several configurations were tested to find the optimum configuration as shown in Figure 3.4.

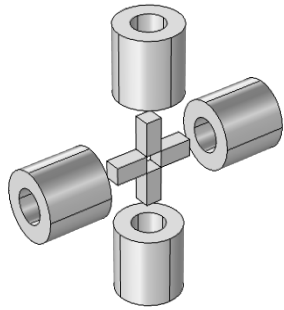
The spherical permanent magnet shown in Figure 3.4a was not suitable for our design because of the complexity of modeling the magnetic force and the magnetic sphere magnetization. The electromagnetic coils in the overlap design (Figure 3.4b) were not symmetric; this would affect the manipulator stability and the magnetic force calculations. The magnetic force in both the rectangular (Figure 3.4c) and cylindrical (Figure 3.4d) permanent magnet design was assessed. As a result of the multiple edges presented in the rectangular design, a higher magnetic force in the cylindrical permanent magnet design was achieved, and therefore it was selected for our design.



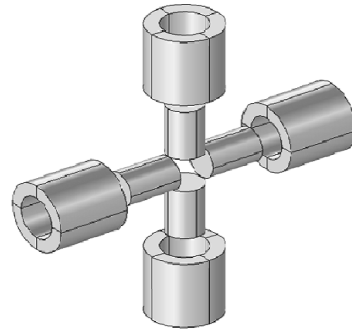
(a) Spherical design.



(b) Overlapping rectangular design.



(c) Rectangular design.

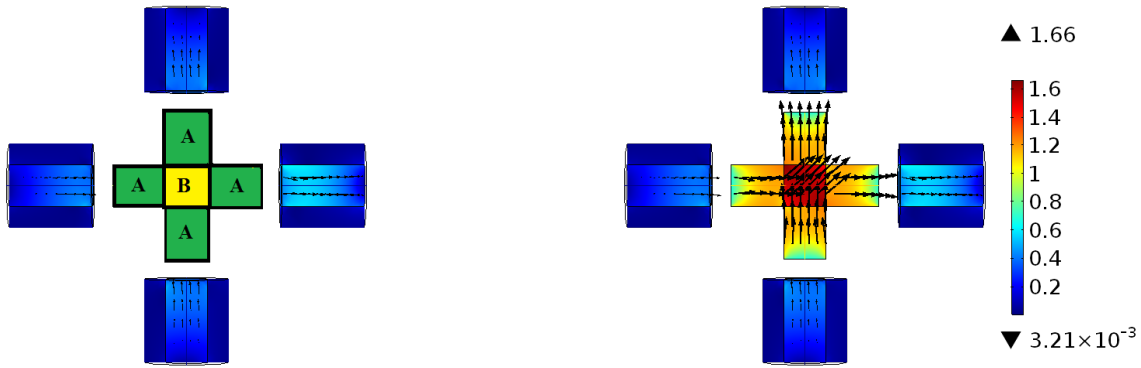


(d) Cylindrical design.

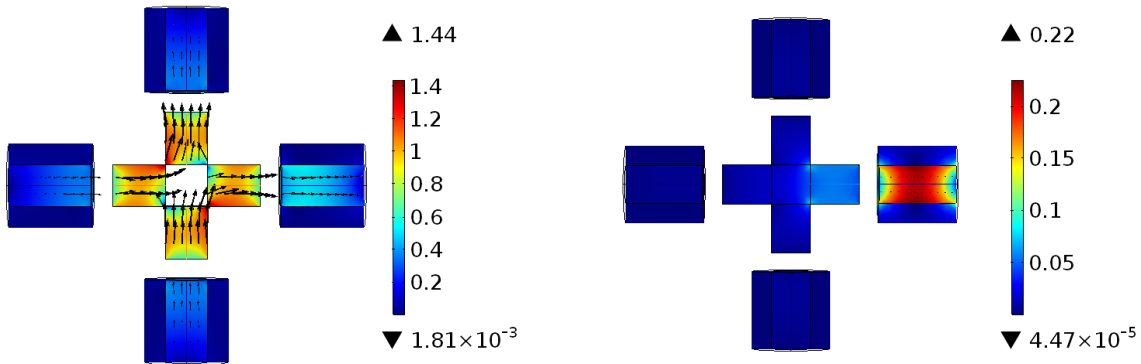
Figure 3.4: Different configurations of the magnetic actuator.

The permanent magnets configuration was simulated in COMSOL multi-physics to obtain the best materials configuration. The two-dimensional geometry of the actuator is shown in Figure 3.5a. Three cases representing three configurations were studied as shown in Figure 3.5: in case 1 (Fig 3.5b), material A is a permanent magnet and material B is an iron material; in case 2 (Figure 3.5c), material A is a permanent magnet and material B is air; in case 3 (Figure 3.5d), materials A and B are both iron. The simulation results for the magnetic field calculation are shown in Figures 3.5b, 3.5c, and 3.5d. The magnetic

flux density norm (*Tesla*) was also simulated for the different configurations of the three cases. The magnetic flux density norm in case 3 was very low compared to cases 1 and 2. The value for case 1 was slightly higher than case 2, but the actuator weight in case 1 was also higher. The magnetic flux density norm difference is less than 0.22 *Tesla*, therefore case 2 was selected for our application.



(a) Two dimensional geometry of the actuator. (b) Case 1 (A=Permanent Magnet, B=Iron).



(c) Case 2 (A=Permanent Magnet, B=Air). (d) Case 3 (A=Iron, B=Iron).

Figure 3.5: Magnetic flux density norm (*Tesla*) for different materials configurations.

### 3.3.2 Magnetic Drive Linear Actuator

The linear magnetic actuator (Figure 3.6) consists of a single electromagnetic coil and a permanent magnetic. Both are aligned and concentric along the  $y$  axis.

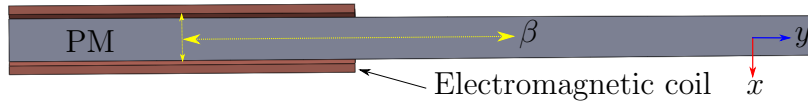


Figure 3.6: Schematic of the magnetic drive linear actuator.

## 3.4 Micromanipulator Kinematics

The position of the end-effector is  $q = [X_q, Y_q, Z_q]$ , while the joint variables are  $\theta = [\alpha, \gamma, \beta]$ . Figures 3.7 and 3.8 depict the relation between the end effector position and joint angles.

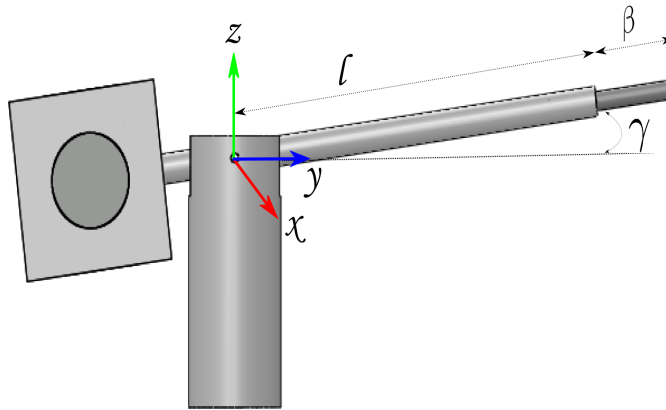


Figure 3.7: Kinematic of the proposed micromanipulator (Right view).

$l$  represents the distance between the center of the revolute joint and the end of the large rod. Joint variables are defined as follows:

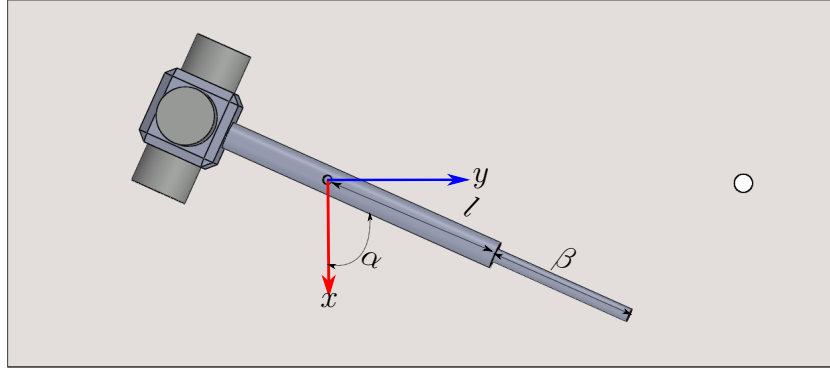


Figure 3.8: Kinematic of the proposed micromanipulator (Top view).

- The angle between the  $x$  axis and the micromanipulator needle is defined as  $\alpha$ .
- The angle between the  $xy$  plane and the micromanipulator needle is defined as  $\gamma$ .
- The prismatic joint displacement along the micromanipulator needle is defined as  $\beta$ .

Based on Figures 3.7 and 3.8, the micromanipulator's forward kinematic equations can be found as follows:

$$X_q = (l + \beta)\cos(\alpha)\cos(\gamma) \quad (3.1)$$

$$Y_q = (l + \beta)\sin(\alpha)\cos(\gamma) \quad (3.2)$$

$$Z_q = (l + \beta)\sin(\gamma) \quad (3.3)$$



### 3.5 Micromanipulator Jacobian

The Jacobian defines the transformation between the micromanipulator end-effector velocity and the joint velocity. In the previous section, we found the relation between the position and orientation of the micromanipulator end-effector with respect to the joint angles; therefore, we can differentiate the position with respect to time to obtain the Jacobian matrix. By differentiating equations (3.1), (3.2), and (3.3) we yield:

$$\dot{X}_q = -(l + \beta)\sin(\alpha)\cos(\gamma)\dot{\alpha} - (l + \beta)\cos(\alpha)\sin(\gamma)\dot{\gamma} + \cos(\alpha)\cos(\gamma)\dot{\beta} \quad (3.4)$$

$$\dot{Y}_q = (l + \beta)\cos(\alpha)\cos(\gamma)\dot{\alpha} - (l + \beta)\sin(\alpha)\sin(\gamma)\dot{\gamma} + \sin(\alpha)\cos(\gamma)\dot{\beta} \quad (3.5)$$

$$\dot{Z}_q = (l + \beta)\cos(\gamma)\dot{\gamma} + \sin(\gamma)\dot{\beta} \quad (3.6)$$

If we rewrite the equations above using matrix notation, we yield the following:

$$\begin{bmatrix} \dot{X}_q \\ \dot{Y}_q \\ \dot{Z}_q \end{bmatrix} = \begin{bmatrix} -(l + \beta)\sin(\alpha)\cos(\gamma) & -(l + \beta)\cos(\alpha)\sin(\gamma) & \cos(\alpha)\cos(\gamma) \\ (l + \beta)\cos(\alpha)\cos(\gamma) & -(l + \beta)\sin(\alpha)\sin(\gamma) & \sin(\alpha)\cos(\gamma) \\ 0 & (l + \beta)\cos(\gamma) & \sin(\gamma) \end{bmatrix} \begin{bmatrix} \dot{\alpha} \\ \dot{\gamma} \\ \dot{\beta} \end{bmatrix} \quad (3.7)$$

Fundamentally  $\dot{q} = J_q(\theta)\dot{\theta}$ ; therefore based on this relationship the Jacobian matrix for the micromanipulator is:

$$J_q(\theta) = \begin{bmatrix} -(l + \beta)\sin(\alpha)\cos(\gamma) & -(l + \beta)\cos(\alpha)\sin(\gamma) & \cos(\alpha)\cos(\gamma) \\ (l + \beta)\cos(\alpha)\cos(\gamma) & -(l + \beta)\sin(\alpha)\sin(\gamma) & \sin(\alpha)\cos(\gamma) \\ 0 & (l + \beta)\cos(\gamma) & \sin(\gamma) \end{bmatrix} \quad (3.8)$$

## 3.6 Micromanipulator Dynamics

The free body diagram of the finger micromanipulator mechanism with all forces applied to the micromanipulator is illustrated in Figure 3.9. The forces in Figure 3.9 are:

- $W_{pm}$ : Weight of permanent magnet including the holder.
- $F_{cx}$ : Magnetic force generated between permanent magnets and electromagnetic coils in the  $x$  direction.
- $F_{cz}$ : Magnetic force generated between permanent magnets and electromagnetic coils in the  $z$  direction.
- $F_J$ : Revolute joint internal forces.
- $W_c$ : Weight of the electromagnetic coil aligned in the  $y$  direction.
- $W_r$ : Weight of the rod including the permanent magnet in the  $y$  direction.
- $F_{ox}$ : The end-effector force in the  $x$  direction.
- $F_{oz}$ : The end-effector force in the  $z$  direction.

$a$ , represents the distance between the center of the permanent magnet and the center of the revolute joint.  $b$  is the distance between the center of the revolute joint and the rod center of mass.  $c$  is the distance between the rod center of mass and the rod end (linear electromagnetic coil center of mass). Finally,  $F_{ox}$  and  $F_{oz}$  are located at the end-effector end which is  $\beta$  away from the edge of the rod. The dynamic model of the proposed micromanipulator can be derived using Newton's law as follows:

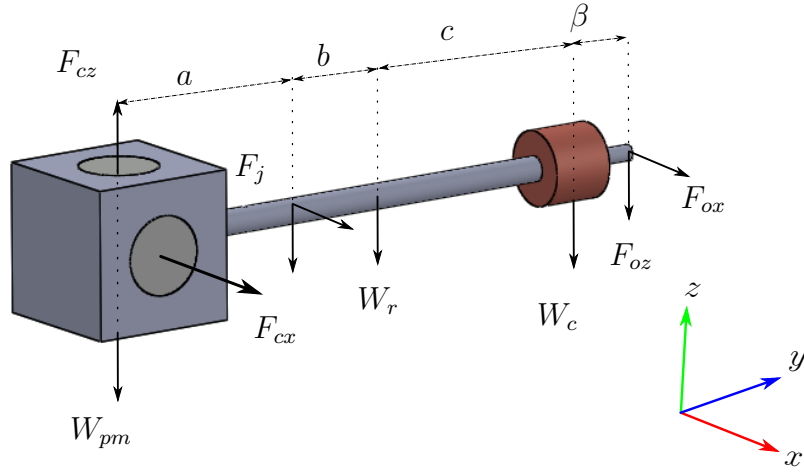


Figure 3.9: Free body diagram of the finger micromanipulator mechanism.

$$\sum T_i = I_i \ddot{\theta}_i \quad (3.9)$$

$$\sum F_i = M \ddot{q}_i \quad (3.10)$$

Where  $I_i$  is the moment of inertia around axis  $i$ ,  $M$  is the total mass,  $T_i$  are the torques around axis  $i$ ,  $F_i$  are the forces in the direction of axis  $i$ ,  $\theta_i$  represents the angular position around axis  $i$ , and  $q_i$  is the position along axis  $i$ . There are no torques along the  $y$  axis, also the finger mechanism has 3 DOF so only three equations are needed in order to obtain the micromanipulator dynamic model. Substituting forces and torques in the previous equations, one can obtain the following dynamic model of the proposed micromanipulator.

$$F_{ox}(b + c + \beta) - F_{cx}(a) = I_z \ddot{\alpha} \quad (3.11)$$

$$\begin{aligned}
F_{oz}(b + c + \beta) + F_{cz}(a) + W_c(b + c) \\
+ W_r(b) - W_{pm}(a) = I_x \ddot{\gamma}
\end{aligned} \tag{3.12}$$

$$\sum F_y = M \ddot{\beta} \tag{3.13}$$

The weight of permanent magnet including the holder  $W_{pm}$  is 7.26  $N$ , the weight of the electromagnetic coil aligned in the  $y$  direction  $W_c$  is 1.39  $N$ , and finally the weight of the rod including the permanent magnet in the  $y$  direction  $W_r$  is 0.5  $N$ . The dimensions of the system are as follows:  $a = 6 \text{ cm}$ ,  $b = 4.5 \text{ cm}$ , and  $c = 10.5 \text{ cm}$ . At equilibrium position, the relation between input and output forces is:

$$F_{ox} = F_{cx} \frac{a}{b + c + \beta} \tag{3.14}$$

$$F_{oz} = \frac{F_{cz}(a) + W_c(b + c) + W_r(b) - W_{pm}(a)}{b + c + \beta} \tag{3.15}$$

It is found that the effect of the Coriolis and centrifugal terms is neglected.

### 3.7 Micromanipulator Workspace Calculations

As mentioned previously, the needle and end-effector dimensions have not been optimized yet. However, the workspace of the micromanipulator can be found based on Figure 3.10.

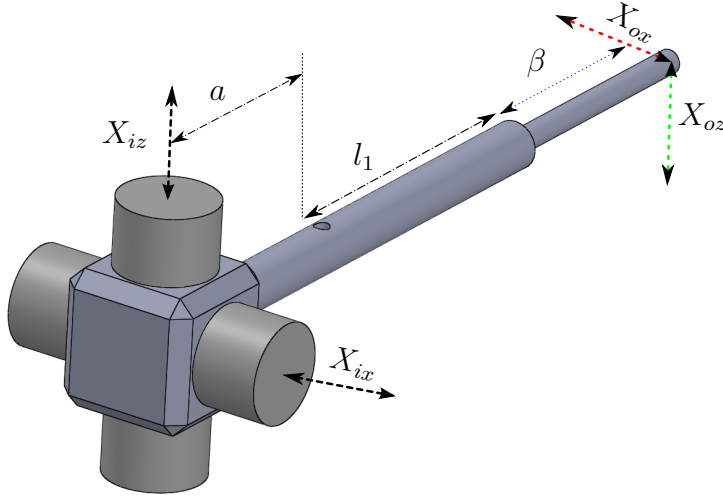


Figure 3.10: Three dimensional workspace representation of the finger micromanipulator mechanism.

$X_{ix}$  and  $X_{iz}$  are the permanent magnets movement in the  $x$  and  $z$  axes respectively. The workspace vector in the  $x$ ,  $y$ , and  $z$  axis respectively is defined by  $[X_{ox}, \beta, X_{oz}]$ . Given that  $a = 6 \text{ cm}$ , and  $l_1 = 15 \text{ cm}$ , the workspace vector components can be found as follows:

$$X_{ox} = X_{ix} \frac{l_1 + \beta}{a} \quad (3.16)$$

$$X_{oz} = X_{iz} \frac{l_1 + \beta}{a} \quad (3.17)$$

$\beta$  can be found by solving the electromagnetic force between the permanent magnet and the electromagnetic coil in the  $y$  direction.

## 3.8 Conclusion

In this chapter the main components of the micromanipulator system and the way they are organized were introduced. In addition, the kinematics, Jacobian, and dynamics models of the micromanipulator were calculated based on the micromanipulator geometry and the applied forces. Lastly, the micromanipulator workspace was found based on the micromanipulator dimensions.

# Chapter 4

## Analytical Modeling and Optimization

### 4.1 Introduction

Electromagnetic force modeling is the first step required to obtain the optimal geometry for the finger micromanipulator. Accordingly, this chapter demonstrates the magnetic field and magnetic force calculations, after that the optimization procedures are presented. The objective of geometry optimization is to find the optimal values for the micromanipulaor design parameters in order to achieve the stated objectives. Lastly, fully symbolic magnetic force modeling is presented.

## 4.2 Magnetization Configuration

The total magnetic actuation force is the vector sum of the generated magnetic forces between any electromagnetic coil and permanent magnet in the actuator. The actuator design has four electromagnetic coils and four permanent magnets, and this resulted in 16 generated forces. The permanent magnet configuration was designed to have an opposite magnetization vector in the same axis (Figure 4.1). As shown in the figure, if coil 2 ( $C_2$ ) is energized, the generated magnetic force between  $C_2$  and permanent magnets 1 and 3 ( $PM_1$  and  $PM_3$  respectively) will have the same magnitude and opposite direction. This magnetization vector configuration reduced the total magnetic force vector sum from 16 to 8. The distance between any coil and the center of the nearest permanent magnet in the same axis was much larger than the distance between that coil and the center of the farthest permanent magnet in the same axis. Therefore the magnetic force between that coil and the nearest permanent magnet was much higher than the magnetic force between that coil and the farthest permanent magnet. As a result, one can consider only the magnetic force between any coil and the nearest permanent magnet in the calculation of the total magnetic force. This also reduced the total magnetic force vector sum from 8 to only 4. The electromagnetic coils could be energized in a way to sum the magnetic force in the same axis, and therefore guide the manipulator finger to any location in the  $xy$  plane, based on the input electromagnetic coil currents  $I_i$ , where  $i$  is coil number  $i$ .



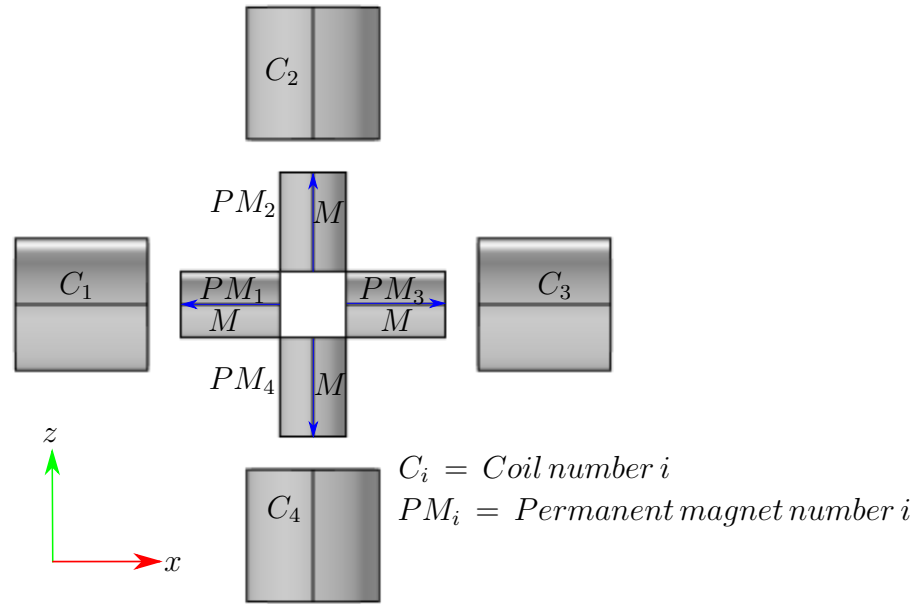


Figure 4.1: Magnetization vector configuration.

## 4.3 Magnetic Field Calculations

### 4.3.1 Magnetic Field Calculations Generated by Electromagnetic Coils

The external magnetic field was produced by using four coreless and theoretically identical electromagnets, and four cylindrical permanent magnets with axial magnetization. All of the components were evenly distributed over the  $xz$  plane (see Figure 4.1). According to the Biot–Savart’s law, the  $z$ -component magnetic field, produced by a thick and coreless solenoid (Figure 4.2), at a point  $P(x, y, z)$  is [52]:

$$B_z(x, y, z) = \frac{\mu_0 \sigma I}{4\pi} \int_{R_{ci}}^{R_{co}} \int_{-0.5l_c}^{0.5l_c} \int_0^{2\pi} \frac{r[(y - y_m - r \sin\phi) \sin\phi + (x - x_m - r \cos\phi) \cos\phi]}{|R_m|^3} d\phi dz dr \quad (4.1)$$

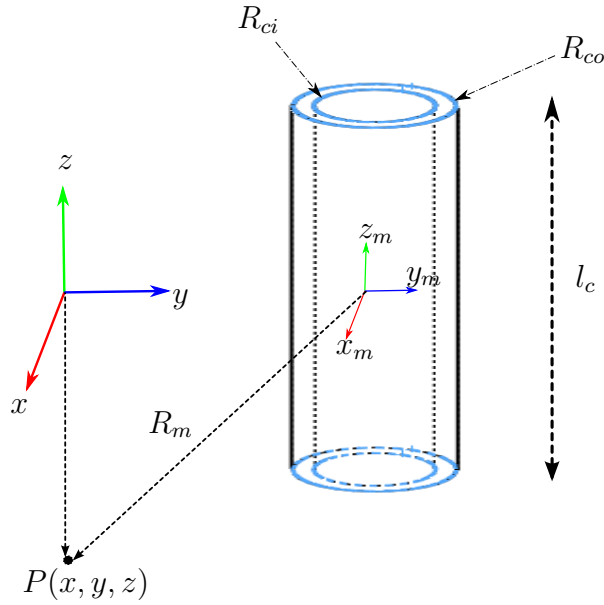


Figure 4.2: Magnetic field calculation generated by electromagnetic coil.

where  $\mu_0$  is the relative permeability of free space,  $\sigma$  is the winding density of the electromagnetic,  $I$  is the current passing through the electromagnetic coil ( $A$ ),  $R_{co}$ ,  $R_{ci}$ , and  $l_c$  are the outer radius, inner radius, and length of electromagnetic coil respectively,  $x_m$  and  $y_m$  are the  $x$  and  $y$  locations respectively of the electromagnetic center point, and  $R_m$  is the distance between the point  $P(x, y, z)$  and the center point of the electromagnetic coil. The  $x$ -component magnetic field can be calculated in a similar way as in equation(4.1).

### 4.3.2 Magnetic Field Calculations Generated by Permanent Magnets

The magnetic field, produced by a permanent magnet (Figure 4.3) at a point  $P(x, y, z)$  is [84]:

$$B(x, y, z) = \frac{\mu_0 Q_m}{4\pi} \left[ \frac{\vec{r}_2}{|r_2|^3} - \frac{\vec{r}_1}{|r_1|^3} \right] \quad (4.2)$$

where  $Q_m$  is the surface magnetic charge, and  $r_1$  and  $r_2$  are the distances to the point  $P(x, y, z)$  from the top and bottom of the permanent magnet respectively.

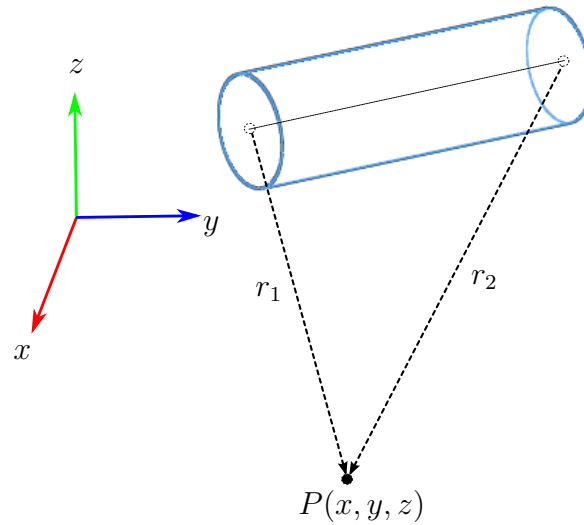


Figure 4.3: Magnetic field calculation generated by permanent magnet.

The total magnetic field at any point at the  $xz$  plane can be found by the superposition principle:

$$B(x, y, z) = \sum_{n=1}^{n=4} \{B_{M_n}(x, y, z) + B_{C_n}(x, y, z)\} \quad (4.3)$$

where  $B_{M_n}$  is the magnetic field generated by permanent magnet number  $n$ , and  $B_{C_n}$  is the magnetic field generated by electromagnetic coil number  $n$ ,  $n = 1, 2, 3, 4$ .

## 4.4 Magnetic Force Calculations

In this section, the magnetic force between any coil and the nearest permanent magnet is calculated. As discussed in the literature, a closed form solution for the magnetic force between two cylindrical magnets or electromagnetic coils is very difficult to obtain. Several approaches have been used by scholars to model the magnetic force between two cylindrical magnets or electromagnetic coils, including numerical integration [85] and numerical discretization [86, 87]. Ravaud et al. [88] used elliptic integrals to find a closed form solution for the magnetic forces between radially-aligned cylindrical magnets. Robertson et al. [89] proposed a simplified solution for the Ravaud elliptic integral method, that can be executed faster in real time applications to find the attractive or repulsive magnetic forces between cylindrical magnets and thin coils [89], or the axial attractive or repulsive magnetic force between a coaxial cylindrical magnet and a thick electromagnetic coil that consists of many radial and axial turns [90]. In this work, the “shell method” discussed in [90] is used. By this method, the axial attractive or repulsive magnetic force between a thick electromagnetic coil and a cylindrical magnet can be found by representing each radial layer of turns as a separate thin coil. The total magnetic force between them is the summation of the forces between each thin coil and the cylindrical magnet.

## 4.5 Optimization

The axial magnetic force  $F_m$  between a cylindrical permanent magnet and electromagnetic coil, as shown in Figure 4.4, is a function of many parameters (Appendix A):

$$F_m = f(B_r, I, N_r, N_z, R_m, l_m, R_{ci}, R_{co}, l_c, z, R_w, l_w, \rho) \quad (4.4)$$

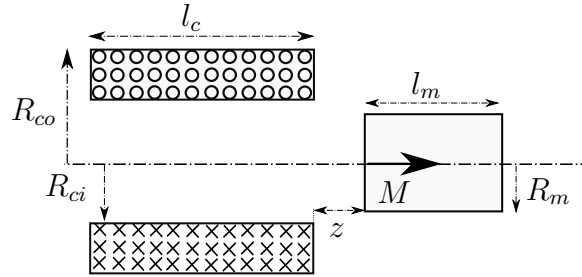


Figure 4.4: Schematic diagram of electromagnetic coil and permanent magnet configuration.

where  $B_r$  is the residual flux density ( $T$ ),  $I$  is the current passing through the electromagnetic coil ( $A$ ),  $N_r$  and  $N_z$  are the number of turns in the radial and axial directions respectively,  $R_m$  and  $l_m$  are the radius and length of the permanent magnet in meters,  $R_{co}$ ,  $R_{ci}$  and  $l_c$  are the outer radius, inner radius, and length, respectively, of the electromagnetic coil in meters,  $z$  is the axial air gap distance between the edges of electromagnetic coil and the cylindrical magnet ( $m$ ),  $R_w$  and  $l_w$  are the radius and length respectively of the wire used to wind the electromagnetic coil ( $m$ ), and  $\rho$  is the resistivity of the wire ( $\Omega.m$ ). The proposed actuator was expected to move in the  $xz$  plane to a maximum distance of  $1\text{ cm}$ ; therefore the axial air gap distance  $z$  between the edges of the electromagnetic coil and the cylindrical magnet was fixed at  $1\text{ cm}$  to decrease the complexity of the optimization

process. Similarly, the number of turns was kept constant at 1760 turns ( $N_r \times N_z = 1760$ ). This number could subsequently be adjusted slightly to fit the electromagnetic coil dimensions. The wire parameters ( $R_w$ ,  $l_w$ , and  $\rho$ ) could be calculated after the optimization based on the total number of turns and the standardized American Wire Gauge (AWG).  $B_r$  is constant and depends on the type of the permanent magnets. To obtain a large magnetic force, Neodymium magnets of a higher grade were used, therefore  $B_r$  was fixed at 1.32 *Tesla*, which matched a Neodymium magnet grade of N42. After removing the fixed parameters, the axial magnetic force  $F_m$  between a cylindrical permanent magnet and electromagnetic coil in (4.4) is:

$$F_m = f(R_m, l_m, R_{ci}, R_{co}, l_c) \quad (4.5)$$

To optimize eq 4.5, the volume of the permanent magnet was fixed at  $V_m = 20 \text{ cm}^3$ , the volume of the electromagnetic coil at  $V_c = 47 \text{ cm}^3$ , and the difference between the coil outer and inner radii at 0.5 *cm*. The optimization parameters were the magnetic geometry ratio:

$$\alpha = \frac{l_m}{R_m} \quad (4.6)$$

and the coil geometry ratio:

$$\gamma = \frac{R_{co}}{l_c} \quad (4.7)$$

The simulation result is shown in Figure 4.5. The maximum magnetic force  $F_m$  was 10.7*N*. The optimized magnetic and coil geometry ratios  $\alpha$  and  $\gamma$  were 0.25 and 1 respectively. Solving for the actuator geometry, the following dimensions were obtained:

$$(l_m R_m l_c R_{co} R_{ci}) = (0.73 \ 2.94 \ 4 \ 4 \ 3.5) \text{ cm} \quad (4.8)$$

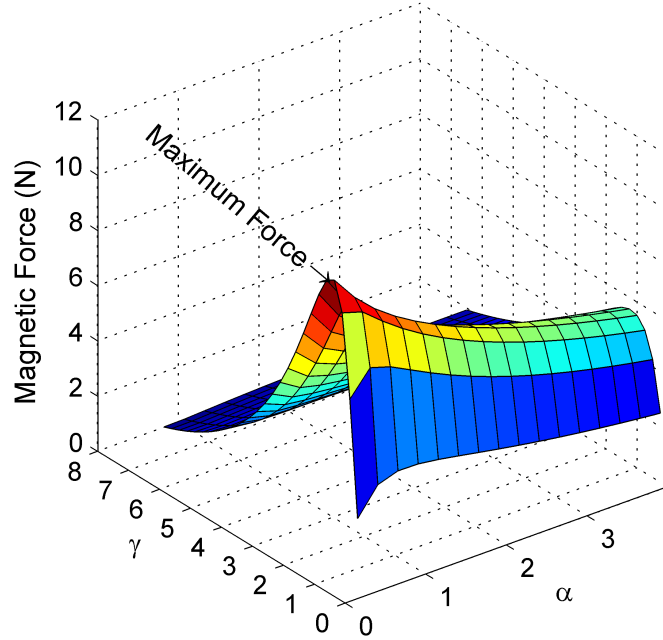


Figure 4.5: Magnetic force versus magnet ( $\alpha$ ) and coil ( $\gamma$ ) geometry ratios.

A notable problem with this design was its bulkiness, since the permanent magnet had a diameter of approximately  $6 \text{ cm}$ . Additionally, it was very difficult to obtain commercially a permanent magnet with these dimensions. The optimization process was changed so that the dimensions of the permanent magnet were fixed and only the coil dimensions were changed to obtain the required force. To obtain the required coil geometry, a permanent magnet (which was available commercially) was used with a length and radius of  $3.17$  and  $1.58 \text{ cm}$ , respectively. The volume of this permanent magnet was  $V_m = 25 \text{ cm}^3$ , and the

volume of the electromagnetic coil in this new optimization was also fixed at  $V_c = 47 \text{ cm}^3$ . The new optimization parameters consist of the coil geometry ratios as follows:

$$\alpha = \frac{R_{co}}{R_{ci}} \quad (4.9)$$

$$\beta = \frac{l_c}{2R_{co}} \quad (4.10)$$

Assuming the number of turns is also constant, the axial magnetic force  $F_m$  between a cylindrical permanent magnet and electromagnetic coil in eq 4.5 is:

$$F_m = f(R_{ci}, R_{co}, l_c, R_m = 1.58 \text{ cm}, l_m = 3.17 \text{ cm}) \quad (4.11)$$

The simulation result is shown in Figure 4.6. The maximum magnetic force  $F_m$  is approximately  $14.4 \text{ N}$ . The optimal values for the optimization parameters  $\alpha$  and  $\beta$  were 2 and 0.25 respectively. Solving for the actuator geometry, the following dimensions were obtained:

$$(l_c \ R_{co} \ R_{ci}) = (1.7 \ 3.4 \ 1.7) \text{ cm} \quad (4.12)$$



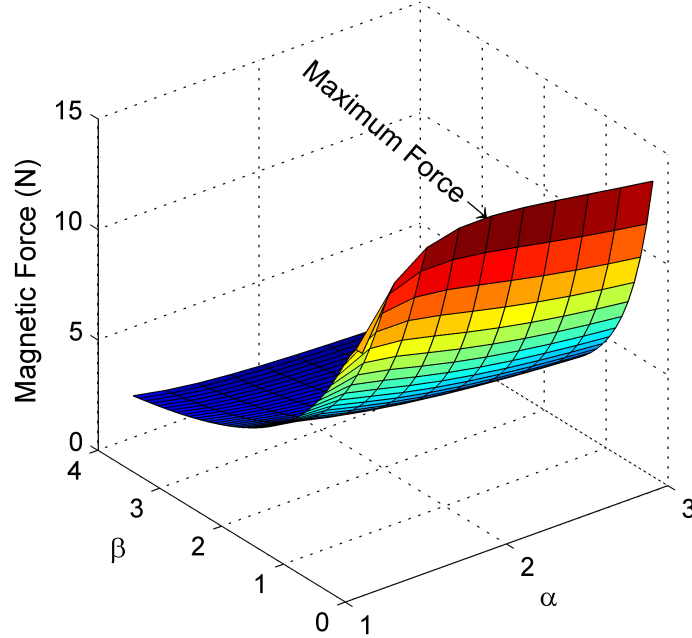


Figure 4.6: Magnetic force versus coil geometry ratios  $\alpha$  and  $\beta$ .

The generated magnetic force ( $14.4N$ ) was large enough compared to the end-effector desired force (approximately  $2N$ ). Additionally, the manipulator needle length  $l$  in Figure 3.3 could be adjusted to create a large workspace area and large force ratio. In order to build the electromagnetic coil with the previous dimensions, several parameters needed to be determined. Given that the current passing through the coil was fixed at  $1A$ , and the total number of turns was fixed at 1760 turns, the only AWG wire that can fit these dimensions is AWG26. In this case, the radius  $R_w$  of the AWG26 wire is  $0.2025\text{ mm}$ ; this value was used to solve for the wire length  $l_w$  required to allow 1760 turns in the following equation:

$$l_w = 2\pi N(R_{ci} + N_r R_w) \quad (4.13)$$

The wire length  $l_w$  was calculated to be 282  $m$ . The number of turns in the radial ( $N_r$ ) and axial ( $N_z$ ) directions was 42 turns. Finally, given that the resistivity of copper  $\rho$  is  $1.68 \times 10^{-8} \Omega \cdot m$ , the DC resistance  $R$  was calculated to be 36.8  $\Omega$  using the equation:

$$R = \frac{\rho l_w}{\pi(R_w)^2} \quad (4.14)$$

The AWG26 wire cannot handle more than approximately 1  $A$ , and that limits the subsequent actuator controlling process. Therefore, the number of ampere-turns was changed to allow a smaller AWG that can handle a larger current (e.g., AWG22 can handle up to 3.5  $A$ ). The radius  $R_w$  of the AWG22 wire is 0.322  $mm$ . In this case, the number of turns in the radial ( $N_r = (R_{co} - R_{ci}) / (2R_w)$ ) and axial ( $N_z = l_c / (2R_w)$ ) directions that can fit the coil dimensions is 26 turns. Solving for the wire length  $l_w$  using eq 4.13 gives  $l_w = 111 m$ , and the DC resistance  $R$  is 5.57  $\Omega$ . To find the current  $I$  that passes through the electromagnetic coil, the power in both AWGs (26 and 22) needs to be the same. Using the following energy equation:

$$I_1^2 R_1|_{AWG=26} = I_2^2 R_2|_{AWG=22} \quad (4.15)$$

where,  $I_1$  is the current passing through AWG26 (1 $A$ ), resistance  $R_1$  is 36.8 $\Omega$ , and resistance  $R_2$  is 5.57 $\Omega$ , we can solve for the new current that will produce the same interaction magnetic force ( $F_m = 14.4N$ ):  $I_2 = 2.52A$ . The optimization results are summarized in Table 4.1.

Table 4.1: Summary of the optimization results

Axial interaction magnetic force $F_m$		14.4 N	
Axial distance $z$		1 cm	
Coil specifications		Permanent magnet specifications	
$l_c$	1.7 cm	$l_m$	3.17 cm
$R_{ci}$	1.7 cm	$R_m$	1.58 cm
$R_{co}$	3.4 cm	$B_r$	1.32 Tesla
$V_c$	47 cm <sup>3</sup>	$V_m$	25 cm <sup>3</sup>
Wire and winding specifications			
		AWG26	AWG22
$R_w$		0.2025 mm	0.322 mm
$N_z$		42 turn	26 turn
$N_r$		42 turn	26 turn
$N$		1764 turn	676 turn
$l_w$		282 meter	111 meter
$R$		36.8 $\Omega$	5.57 $\Omega$
$I$		1 A	2.52 A

## 4.6 Magnetic Force Modeling

The axial interaction magnetic force  $F_m$  was plotted for different axial distances  $z$  between the edges of the electromagnetic coil and the cylindrical permanent magnet using Ansys Maxwell FEM software. For both wire gauges, AWG22 and AWG26, the interaction mag-

netic force  $F_m$  was plotted for a range of 1 to 5 cm between the edges of the electromagnetic coil and the cylindrical permanent magnet. The simulation results are shown in Figures 4.7 and 4.8.

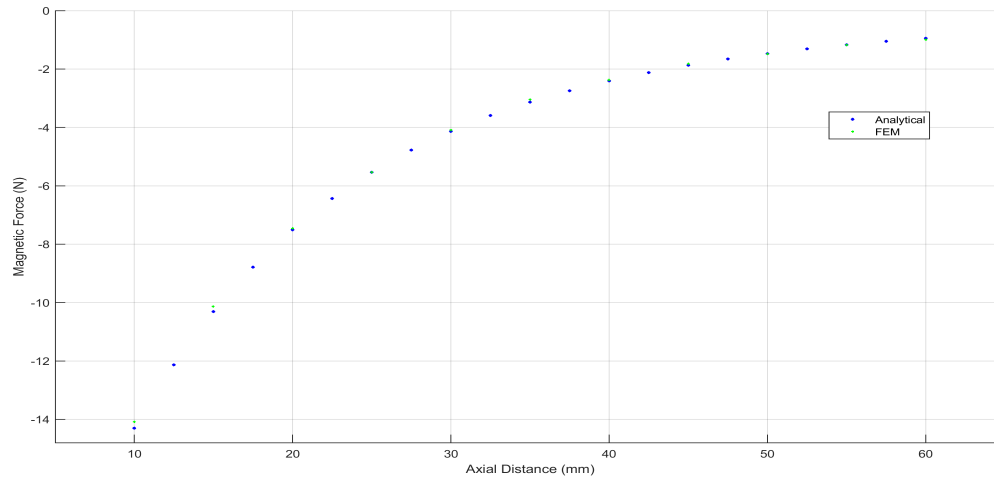


Figure 4.7: Magnetic force versus air gap for AWG26 at 1 A.

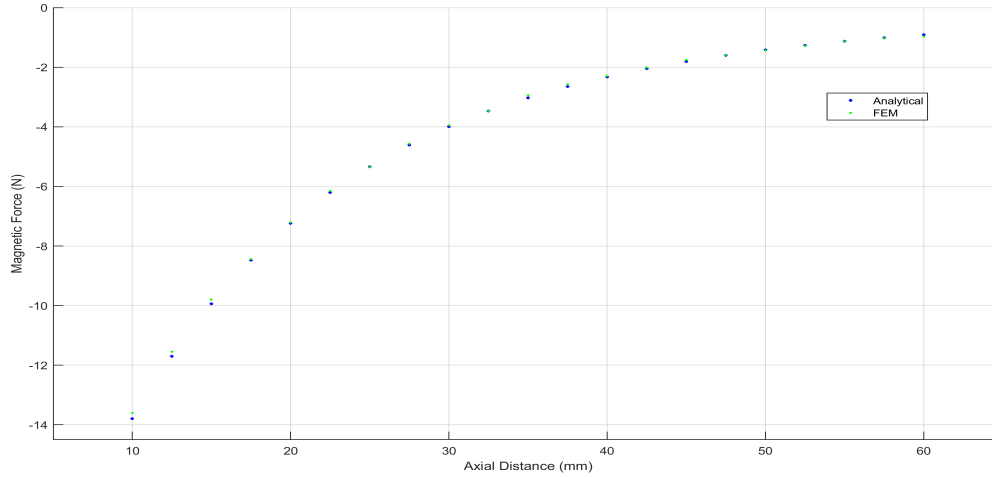


Figure 4.8: Magnetic force versus air gap for AWG22 at 2.52 A.

It can be seen from Figures 4.7 and 4.8 that both AWG results are in agreement. The error between the analytical and FEM is plotted in Figure 4.9 for AWG26 and in Figure 4.10 for AWG22.

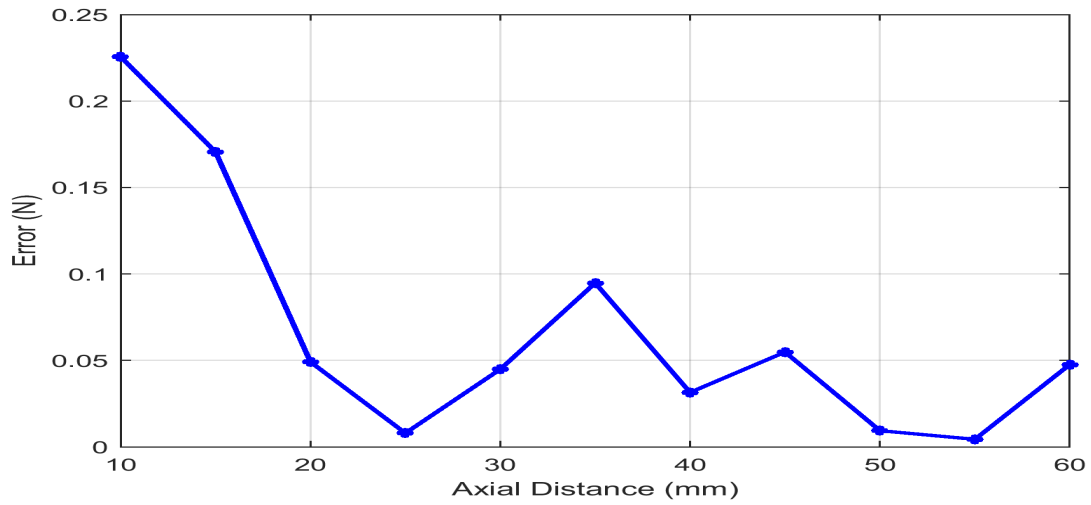


Figure 4.9: Magnetic force error for AWG26 at 1 A.

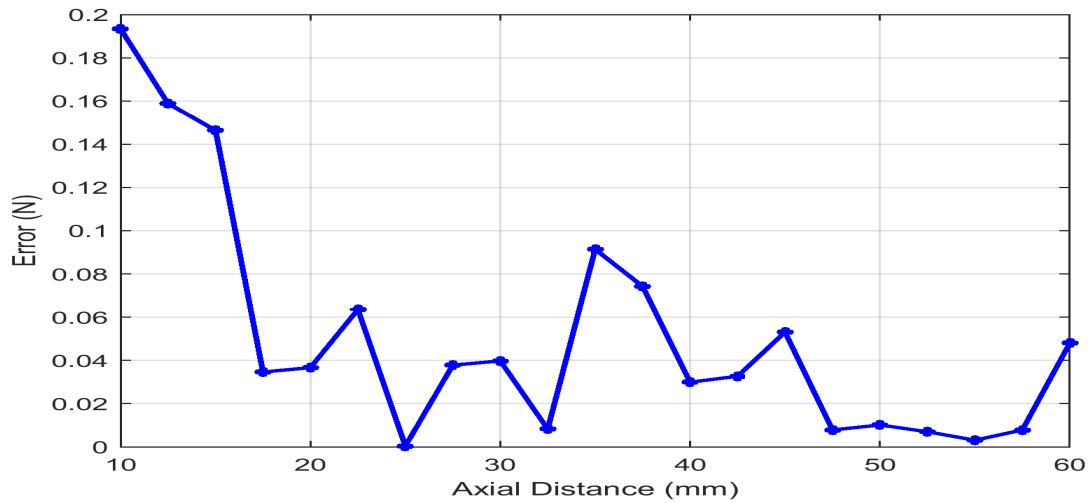


Figure 4.10: Magnetic force error for AWG22 at 2.52 A.

Using the AWG22 wire gauges, the magnetic force  $F_m$  was obtained using the "shell method" for the following ranges: current  $I$  from 0 to 5 A, and axial gap  $z$  from 10 to

60 mm. The magnetic force is plotted in Figure 4.11.

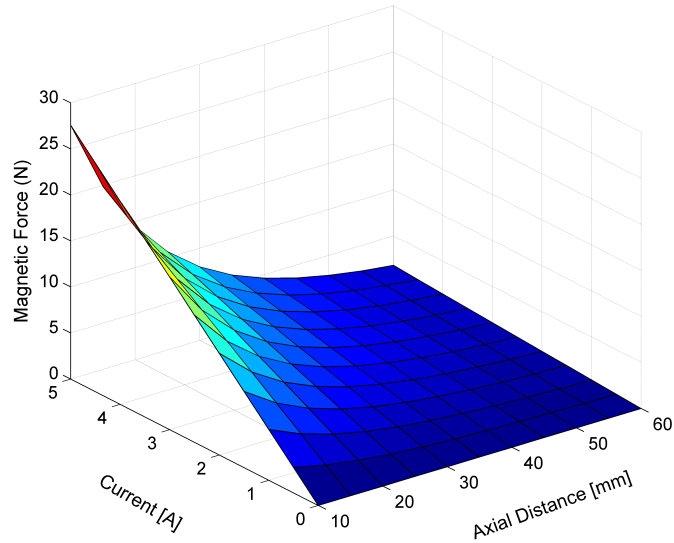


Figure 4.11: Magnetic force versus axial air gap and excitation current.

It was observed that it is possible to model magnetic force and axial distance relationship at different current values; therefore the relationship between magnetic force and axial distance at current values between 0 and 5 A was plotted in Figure 4.12.

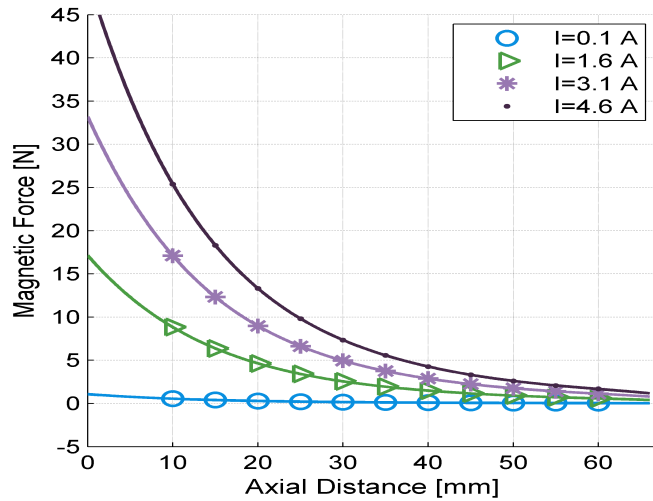


Figure 4.12: Magnetic force versus axial air gap for different excitation currents.

Additionally, we can model the relationship between the magnetic force and the axial distance by a sum of decaying exponential functions:

$$F_m(z) = Ae^{bz} + De^{dz} \quad (4.16)$$

This equation is valid for an axial distance range of 0 to 60 *mm*. We plotted the relationship between the magnetic force and the excitation current at different axial distances between 0 and 60 *mm* (Figure 4.13).



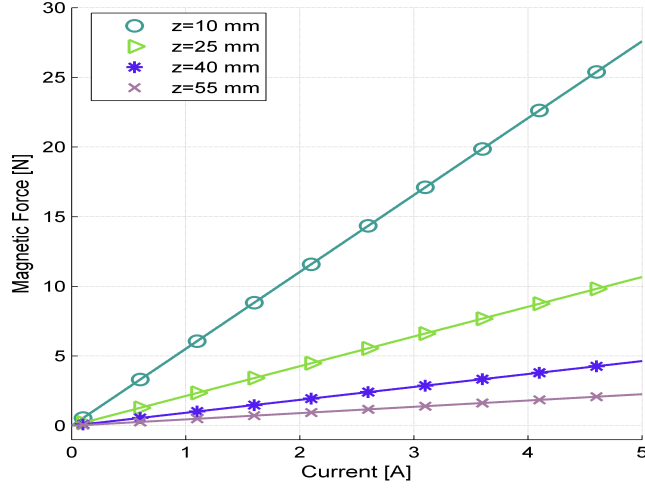


Figure 4.13: Magnetic force versus excitation current at different axial air gaps.

The relationship between the magnetic force and the excitation current can be modeled by a linear function:

$$F_m(I) = k_1 I + k_0 \quad (4.17)$$

For the purposes of controlling the actuator, a symbolic representation of the magnetic force as a function of the axial distance and the excitation current  $F_m(z, I)$  is required. Based on eqs 4.16 and 4.17,  $F_m(z, I)$  can be modeled by a nonlinear function:

$$F_m(z, I) = (Ae^{bz} + Ce^{dz})I + (A_2e^{b_2z} + C_2e^{d_2z}) \quad (4.18)$$

To find the coefficients in eq 4.18, a linear fit between the given current and axial distance ranges was performed. The coefficients are:

$$A = -10.03, b = -0.07127, C = -0.7159, d = -0.01854, A_2 = -4.664 \times 10^{-14}, \\ b_2 = -0.06019, C_2 = -3.511 \times 10^{-17}, d_2 = 0.1111.$$

## 4.7 Conclusion

This chapter focused on the analytical modeling and optimization procedures for building the micromanipulator. First, the magnetic field and magnetic force were calculated, then the optimization procedures were presented. Lastly, a fully symbolic magnetic force model was found.

# Chapter 5

## Controller Design

### 5.1 Introduction

Controlling magnetic levitation systems is not an easy task. Due to the inherent non-linearity of magnetic levitation systems, one of the greatest challenges in development of these systems is designing a robust control strategy. In addition, working in unknown environments with unknown parameters such as payloads makes the controller process even more difficult. A considerable amount of literature has been published on designing robust controllers for magnetic levitation systems. The well-known PID control method has been successfully implemented to control various magnetically levitated systems [91, 92, 93, 94].

Controlling a nonlinear system using a PID control strategy requires linearizing the dynamic model around an operating point, which limits the PID control strategy to a small working area. The sliding mode control technique has also been used to control magnetic bearings and magnetic levitation systems [95, 96, 97, 98]. Using this approach, researchers have been able to control several magnetic systems for various applications.

Conversely, previous experimental work indicated that the sliding mode control method has a key problem regarding the need for a high sampling frequency [99]. Thus, the main limitation with sliding mode control in magnetic levitation systems is that magnetic systems in general have inherent delays. Such delays affect the sliding mode control action, which may result in an undesired response and chattering [100].

A considerable body of literature has grown up around the use of the state-feedback linearization control method to control magnetic levitation systems [101, 102, 103, 104, 105]. The purpose of the state-feedback linearization is to transform the dynamics of a nonlinear system to behave like a linear system [106]. In order to convert a nonlinear dynamic model into a linear one, state-feedback linearization requires full pre-knowledge of the system's dynamic model. In most magnetic levitation systems, the dynamic model changes in real-time. This is either because of the process of operation as magnetic levitation systems are commonly used in industry to levitate unknown payloads with unknown masses [107], or because of the disturbance in the magnetic field which affects the magnetic force modeling. This problem means that the feedback linearization is not the best option for magnetic levitation systems. To overcome the problem of unknown parameters in the dynamic model of magnetic levitation systems, researchers have used adaptive control algorithms [108, 109, 110, 111, 112, 113]. Adaptive control techniques do not need pre-knowledge of the system's dynamic model, as they adapt and learn the unknown dynamic and sequentially adjust the control signal to overcome the issue of variation in the system's dynamic model.

Due to the nonlinear dynamic of the actuator electromagnetic force, the manipulator motion in all axes is non-linear. Hence, it is crucial that the proposed controller should be designed with robust performance. An overview of the position control loop is presented in simplified form in Figure 5.1. The plant model is non-linear. In addition it changes in

real time with the payload variation. In the following sections, the proposed controllers are presented. The proposed controllers are: PID controller, state-feedback controller, and adaptive controller.

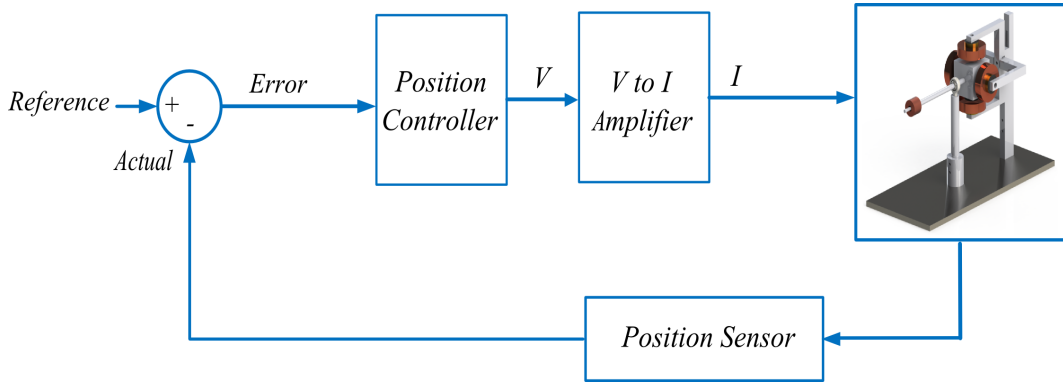


Figure 5.1: Schematic of the position control loop.

## 5.2 PID Controller

The motion of the micromanipulator will not be accurate and stable without a control strategy. Therefore a linear PID controller is designed in order to regulate and control the micromanipulator end-effector position in the workspace. The PID controller is implemented with the general form shown in (5.1).

$$I_{PID}(t) = K_t [K_p e(t) + K_i \int_0^t e(t) dt + K_d \dot{e}] + K_W \quad (5.1)$$

where  $I_{PID}$  is the output of the PID controller that represents the excitation current.  $e(t)$  is the error signal at time  $t$ ,  $K_W$  is the weight compensation gain, and  $K_t$  is the

position to current gain.  $K_p$ ,  $K_i$  and  $K_d$  represent proportional, integral, and derivative gains, respectively. The PID controller gains can be tuned using standard methods such as Ziegler-Nichol tuning rules.

### 5.2.1 Electromagnetic Force linearization

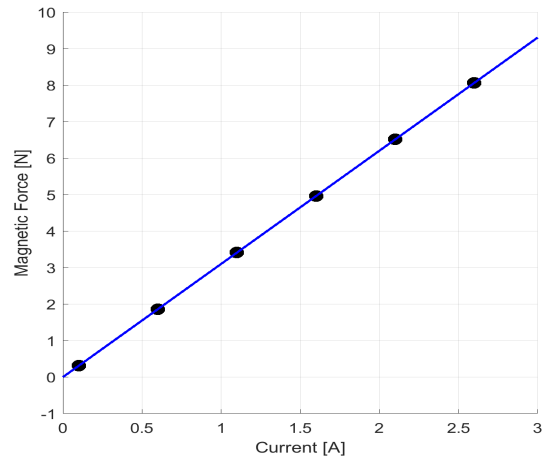
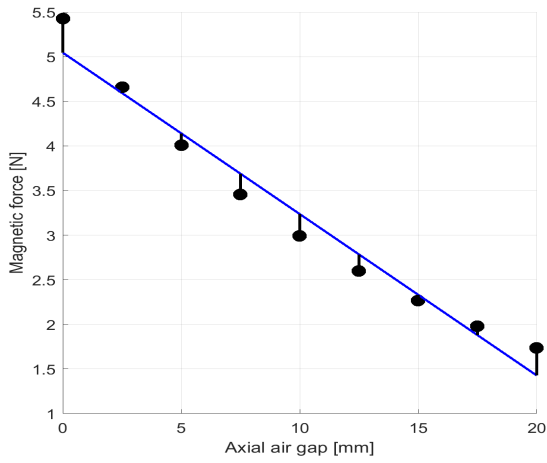
When the rod is centered with the drive unit, the axial air gap between any pair of permanent magnets and electromagnetic coils is  $10\text{ mm}$ . The maximum motion range for the permanent magnets in the  $x$  and  $z$  directions is  $\pm 10\text{ mm}$ . The electromagnetic force between one electromagnetic coil and one permanent magnet was measured using an ATI force sensor for different excitation currents and different axial air gaps. First, the electromagnetic force versus the axial air gap was measured when the excitation current was  $1\text{ Ampere}$ . The results are shown in Figure 5.2a. The root-mean-square error value was  $0.2\text{ N}$  and the coefficient of determination  $R^2$  was  $0.96$ . As seen in this Figure, the electromagnetic force in the controlled area can be approximated as a linear function. In addition, the magnetic force was measured versus the excitation current when the axial air gap was  $10\text{ mm}$ . The results provided in Figure 5.2b show that the relation between the magnetic force and the excitation current is linear.

Based on these results, the electromagnetic force  $F_m(z, I)$  as a function of the axial air gap distance  $z$  and the excitation current  $I$  can be modeled by:

$$F_m(z, I) = (\alpha_1 z + \beta_1)I \quad (5.2)$$

where  $\alpha_1$  and  $\beta_1$  are numerical constants.

In addition, to show that the linearization is valid in the controlled region, a 2D Ansys simulation for the magnetic flux density was added in that region as shown in Figure 5.3.



(a) Electromagnetic force vs axial air gap. (b) Electromagnetic force vs excitation current.

Figure 5.2: Electromagnetic force experimental results.

As seen, the magnetic flux density is almost uniform in the region between the coil and the permanent magnet.

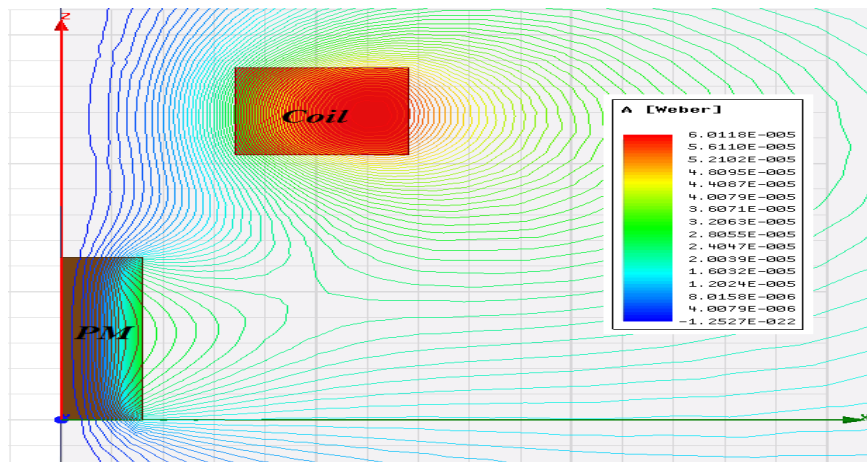


Figure 5.3: Magnetic flux simulation.

### 5.2.2 PID Controller Design in the $z$ Axis

The dynamic equation in the  $z$  axis was already found in eq (3.12). For a small  $\gamma$ , and assuming no contact force at the end-effector, eq (3.12) can be rewritten as:

$$F(z, I)(a) + W_c(b + c) + W_r(b) - W_{pm}(a) = I_x a \ddot{z} \quad (5.3)$$

The equation of the magnetic force that was found earlier in eq (5.2), can be rewritten as:

$$F(z, I) = f_1(z)I \quad (5.4)$$

where:

$$f_1(z) = \alpha_1 z + \beta_1 \quad (5.5)$$

rearranging the dynamic model in eq (5.3), the feed-forward current  $I_{ff}$  at saturation position  $z_0$  is:

$$I_{ff} = \frac{W_c(b + c) + W_r(b) - W_{pm}(a)}{f_1(z_0)a} \quad (5.6)$$

This model is not linear, and in order to design a PID controller, the system needs to be linearized around an operating point. A linearized model is valid only when the system operates in a sufficiently small range around an equilibrium point. Linearizing the dynamic motion equation in eq (5.3) at  $(z_0, I_0)$ , the linearized model will follow:



$$\begin{aligned}\ddot{z} &= g(z_0, I_0) + \frac{\partial g}{\partial z}(z - z_0) + \frac{\partial g}{\partial I}(I - I_0) \\ &= \frac{\frac{\partial f_1(z_0)}{\partial z} I_0}{I_x}(z - z_0) + \frac{f_1(z_0)}{I_x}(I - I_0)\end{aligned}\tag{5.7}$$

which represents a linear model:

$$\ddot{z} = k_1(z_0, I_0)(z - z_0) + k_2(z_0, I_0)(I - I_0)\tag{5.8}$$

where  $k_1$  and  $k_2$  are constants that depend on the desired position  $z_0$ .

### 5.2.3 PID Controller Design in the $x$ Axis

As found in eq (3.11), and assuming no contact force at the end-effector, the equation of dynamic motion in the  $x$  axis is:

$$-F_{cx}(a) = I_z \ddot{\alpha}\tag{5.9}$$

Using both electromagnetic coils in the  $x$  axis as shown in Figure 5.4:

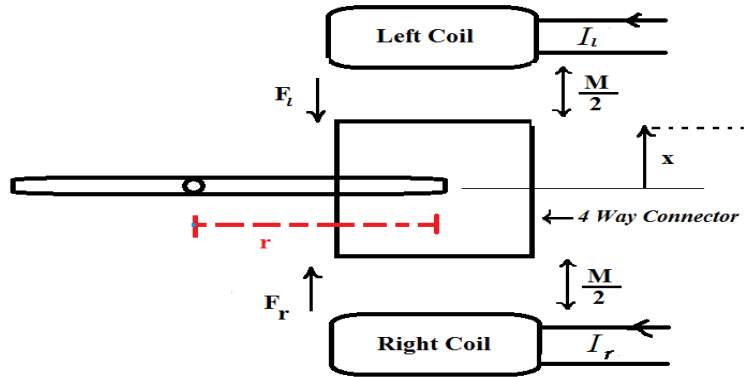


Figure 5.4: Free body diagram in the  $x$  axis.

where  $M/2$  is the distance between coils and permanent magnets when  $x = 0$ ,  $I_r$  and  $I_l$  are the excitation currents in the right and left coils respectively. Based on that, the dynamic equation becomes:

$$I_z \ddot{\alpha} = F_l r - F_r r \quad (5.10)$$

The equation of the right and left magnetic forces ( $F_r$  and  $F_l$ ) respectively were found before in eq (5.2). Rewriting here for a small  $\alpha$ :

$$I_z r \ddot{x} = I_l f_1(x_l) r - I_r f_1(x_r) r \quad (5.11)$$

As it is shown in Figure 5.4, the distance between the finger and right and left electromagnetic coils ( $x_r$  and  $x_l$  respectively) depends on  $M/2$ . After inserting these in the previous equation, the dynamic equation in the  $x$  axis results as:

$$\ddot{x} = \frac{I_l}{I_z} f_1\left(\frac{M}{2} + x\right) - \frac{I_r}{I_z} f_1\left(\frac{M}{2} - x\right) \quad (5.12)$$

Each coil has a bias current  $I_0$  plus a controlling current  $I$ . The relation between left and right currents can be found as:

$$I_l = I_0 + I \quad (5.13)$$

$$I_r = I_0 - I \quad (5.14)$$

Substituting eq (5.13) and eq (5.14) in eq (5.12), the dynamic model becomes:

$$\ddot{x} = \frac{I_0 + I}{I_z} f_1\left(\frac{M}{2} + x\right) - \frac{I_0 - I}{I_z} f_1\left(\frac{M}{2} - x\right) \quad (5.15)$$

Similar to the motion in the  $z$  axis, the motion in the  $x$  axis is also not linear. Therefore, the first step in linearizing the equation is to approximate  $I$  and  $x$  around the saturation point  $(x_{ss}, I_{ss})$  as follows:

$$\hat{x} = x - x_{ss} \quad (5.16)$$

$$\hat{I} = I - I_{ss} \quad (5.17)$$

Substitute these in the dynamic equation:

$$\ddot{\hat{x}} = \frac{I_0 + \hat{I} + I_{ss}}{I_z} f_1\left(\frac{M}{2} + \hat{x} + x_{ss}\right) - \frac{I_0 - \hat{I} - I_{ss}}{I_z} f_1\left(\frac{M}{2} - \hat{x} - x_{ss}\right) \quad (5.18)$$

At  $(x, I) = (0, 0)$ , the linearized model will follow:

$$\begin{aligned} \ddot{\hat{x}} = & \left( \frac{I_0 + I_{ss}}{I_z} \frac{\partial f_1\left(\frac{M}{2} + x_{ss}\right)}{\partial \hat{x}} + \frac{I_0 - I_{ss}}{I_z} \frac{\partial f_1\left(\frac{M}{2} - x_{ss}\right)}{\partial \hat{x}} \right) \hat{x} \\ & + \left( \frac{f_1\left(\frac{M}{2} + x_{ss}\right) + f_1\left(\frac{M}{2} - x_{ss}\right)}{I_z} \right) \hat{I} \end{aligned} \quad (5.19)$$

which represents a linear model:

$$\ddot{\hat{x}} = K_1 \hat{x} + K_2 \hat{I} \quad (5.20)$$

where  $K_1$  and  $K_2$  are constants that depend on the desired position  $x_{ss}$ .

### 5.2.4 PID Controller Design in the $y$ Axis

The permanent magnets in the  $x$  and  $z$  directions are not moving inside the electromagnetic coils, while the permanent magnet in the  $y$  axis moves inside the electromagnetic coils that surround the finger. The dynamic equation in the  $y$  axis can be found based on the free body diagram shown in Figure 5.5 as follows:

$$F_m - F_f = M\ddot{y} \quad (5.21)$$

where  $F_m$  and  $F_f$  are the electromagnetic and friction force respectively, and  $M$  is the mass of the permanent magnet.

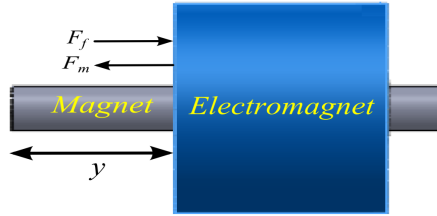


Figure 5.5: Free body diagram in the  $y$  axis.

The equation of the magnetic force in the  $y$  axis was found in (4.18). When eq (5.21) is rearranged to obtain the dynamic equation in the  $y$  axis, we have:

$$\ddot{y} = \frac{f_1(y)I}{M} - \frac{F_f}{M} \quad (5.22)$$

This model is not linear since it includes product of a state variable with the input excitation current. The system therefore is linearized around an operating point in order to design the control law. A linearized model is valid only when the system operates in

a sufficiently small range around an equilibrium point at  $(y_0, I_0)$ . After linearizing the dynamic motion equation in eq (5.22), we have a linear model as follows:

$$\ddot{y} = k_y(y_0, I_0)(y - y_0) + k_i(y_0, I_0)(I - I_0) \quad (5.23)$$

where  $k_y(y_0, I_0)$  and  $k_i(y_0, I_0)$  are the position and current stiffness respectively, and their values depend exclusively on the parameters of the system.

The block diagram for the system in the  $x$ ,  $y$ , and  $z$  axes with the PID Controller is shown in Figure 5.6.

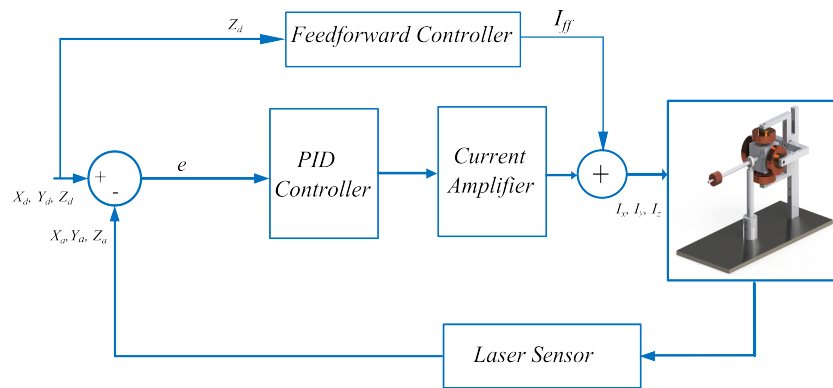


Figure 5.6: Schematic of the control system including the PID controller.

### 5.3 State-Feedback Controller

The manipulator dynamic model in the  $z$  axis as found earlier is:

$$\ddot{z} = f_z(z)I - W \quad (5.24)$$

Defining the state space variables  $x = [x_1, x_2, x_3]$  as the position, velocity, and integration of the error between the desired and actual position of the manipulator, the state space equation of the system is:

$$\begin{bmatrix} \dot{x}_1 \\ \dot{x}_2 \\ \dot{x}_3 \end{bmatrix} = \begin{bmatrix} x_2 \\ -W \\ -x_1 \end{bmatrix} + \begin{bmatrix} 0 \\ f_z(x_1) \\ 0 \end{bmatrix} I \quad (5.25)$$

The output is:

$$y = [1 \ 0 \ 0] x^T \quad (5.26)$$

As seen in this equation, the system's model contains a product of state variables with the input variable; therefore, a state-feedback linearization is required. The purpose of the state-feedback linearization is to transform the dynamics of a nonlinear system to behave like a linear system [106]. By choosing the feedback control law as:

$$I = \frac{W + (K_1 x_1 + K_2 x_2 + K_3 x_3)}{f_z(x_1)} \quad (5.27)$$

the closed loop system is described by the following state differential equation:

$$\begin{bmatrix} \dot{x}_1 \\ \dot{x}_2 \\ \dot{x}_3 \end{bmatrix} = \begin{bmatrix} 0 & 1 & 0 \\ K_1 & K_2 & K_3 \\ -1 & 0 & 0 \end{bmatrix} \begin{bmatrix} x_1 \\ x_2 \\ x_3 \end{bmatrix} \quad (5.28)$$

where  $K = [K_1 \ K_2 \ K_3]$  is a constant state-feedback gain matrix.

The state-feedback gain matrix can be found using any of the state-feedback controller design methods such as the pole placement method, the Linear Quadratic Regulator (LQR),

or an eigenvalue assignment method. The state-feedback gain matrix can be chosen to achieve the desired design requirements.

## 5.4 Adaptive Controller

The dynamic equation of the system in the  $z$  axis was already found in (5.3). Linearizing the system shows that it is a marginally stable system with imaginary poles. The values for the poles depend on the weight constant  $W$ . However, in our application the manipulator is used for pick-and-place operations. Therefore different unknown payloads lead to different unknown values of  $W$ . In this case,  $k_1$ , and  $k_2$  in (5.29) are unknown due to weight parameter variations during operation.

$$\frac{z(s)}{I(s)} = \frac{k_1}{s^2 + k_2} \quad (5.29)$$

In order to adjust for this variation of the payload, a Model Reference Adaptive Control (MRAC) using the MIT rule is implemented. The MRAC scheme uses a reference plant model  $z_m$  that behaves like an ideal plant to adjust the controller parameter. A second order reference model was used, and therefore the following reference model was chosen:

$$\frac{z_m(s)}{z_d(s)} = \frac{\omega_n^2}{s^2 + 2\omega_n\zeta s + \omega_n^2} \quad (5.30)$$

where  $z_d(s)$  is the desired position,  $\omega_n$ , and  $\zeta$  are the natural frequency and the damping ratio, respectively. The MIT rule was used to design the controller with a cost function defined by:

$$J(\theta) = \frac{1}{2}e^2 \quad (5.31)$$

The tracking error  $e$  is the difference between the actual position  $z_a$  and the reference plant model  $z_m$ . The control law for the system excitation current using controller parameters  $\theta = [\theta_1, \theta_2]$  is defined as follows:

$$I = \theta_1 z_d - \theta_2 z_a \quad (5.32)$$

Based on this, the tracking error as a function of  $\theta_1$  and  $\theta_2$  is:

$$e = \frac{\theta_1}{s^2 + k_2 + k_1 \theta_2} z_d - \frac{\omega_n^2}{s^2 + 2\omega_n \zeta s + \omega_n^2} z_d \quad (5.33)$$

The tracking error in (5.33) depends on  $\theta_1$  and  $\theta_2$ , also since the desired position is not a function of both parameters, one can differentiate the tracking error with respect to  $\theta_1$  and  $\theta_2$  as follows:

$$\frac{\partial e}{\partial \theta_1} = \frac{1}{s^2 + k_2 + k_1 \theta_2} z_d \quad (5.34)$$

$$\frac{\partial e}{\partial \theta_2} = \frac{-\theta_1 k_1}{(s^2 + k_2 + k_1 \theta_2)^2} z_d = \frac{-k_1}{(s^2 + k_2 + k_1 \theta_2)} z_a \quad (5.35)$$

As the system characteristics are not known, i.e.  $k_1$ , and  $k_2$  are unknown, and to ensure that the system approaches the reference model, one can substitute the system model in equations (5.34) and (5.35) with the reference model. According to the MIT rule, the change in the parameter  $\theta$  is kept in the direction of the negative gradient of  $J$ ; therefore,

$$\frac{\partial \theta}{\partial t} = -\gamma e \frac{\partial e}{\partial \theta} \quad (5.36)$$

Substituting equations (5.34) and (5.35) in equations (5.36) yields:



$$\frac{\partial \theta_1}{\partial t} = -\gamma e \frac{\omega_n^2}{s^2 + 2\omega_n \zeta s + \omega_n^2} z_d \quad (5.37)$$

$$\frac{\partial \theta_2}{\partial t} = \gamma e \frac{\omega_n^2}{s^2 + 2\omega_n \zeta s + \omega_n^2} z_a \quad (5.38)$$

Figure 5.7 shows the block diagram of the MRAC.

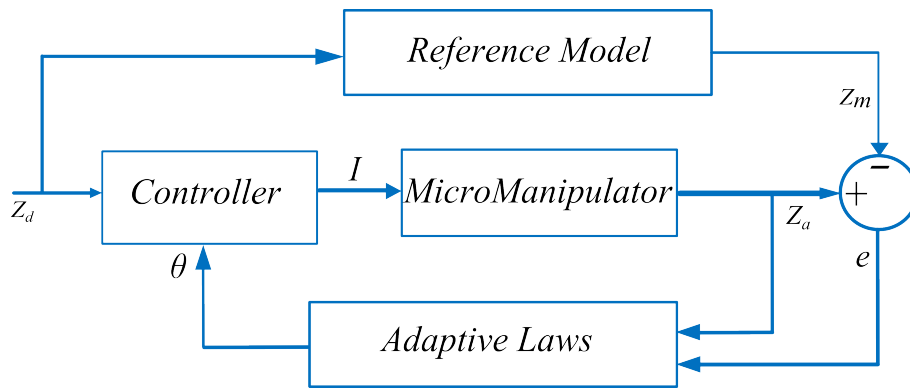


Figure 5.7: Schematic of the MRAC.

# Chapter 6

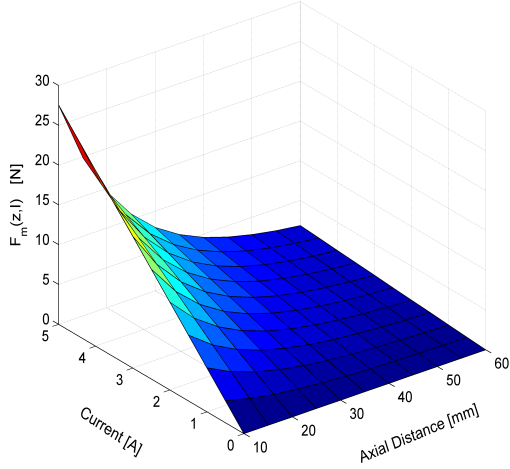
## Results and Validations

Some results regarding the magnetic force modeling were previously presented and discussed in chapter 4. This chapter presents the rest of the results and system validation, including the magnetic force model validation, the experimental results using the control algorithms with and without payload variations, the FEM results, the load capacity analysis at the end-effector tip, and lastly the workspace analysis.

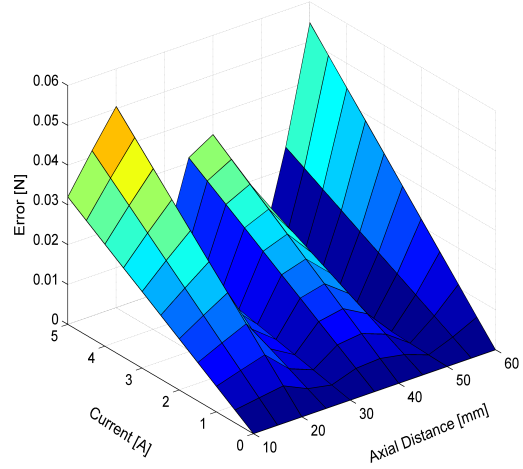
### 6.1 Model Validations

The magnetic force model obtained in eq 4.18 and the absolute error between this model and the initial simulation data previously obtained in Figure ?? are plotted in Figure 6.1.

The error between the model and the simulation data is less than  $0.06\text{ N}$  (Figure 6.1b). Based on the configuration in Figure 6.2 and super-position principle, the total magnetic force on the actuator is the total vector sum of the four magnetic forces.



(a) Model data.



(b) Error between simulation and model data.

Figure 6.1: Magnetic force versus axial air gap and excitation current.

The design was selected to maximize the total magnetic force in each direction. To obtain this, the current in electromagnets in the same axes should have the same magnitude and opposite directions ( $I_1 = -I_3 = I_x$ ) and ( $I_2 = -I_4 = I_z$ ). After inserting these values into eq 4.18, the total magnetic force applied to the actuator can be found using eq 6.1:

$$\begin{aligned}
 F_m(x, z, I_x, I_z) = & (Ae^{bx} + Ce^{dx})I_x + A_2e^{b_2x} + C_2e^{d_2x} + \\
 & (Ae^{b(x-20)} + Ce^{d(x-20)})I_x + A_2e^{b_2(x-20)} + C_2e^{d_2(x-20)} + \\
 & (Ae^{bz} + Ce^{dz})I_z + A_2e^{b_2z} + C_2e^{d_2z} + \\
 & (Ae^{b(z-20)} + Ce^{d(z-20)})I_z + A_2e^{b_2(z-20)} + C_2e^{d_2(z-20)}
 \end{aligned} \tag{6.1}$$

where  $x$  is the distance ( $mm$ ) between  $C_1$  and  $PM_1$ , and  $z$  is the distance ( $mm$ ) between  $C_4$  and  $PM_4$  in Figure 6.2.

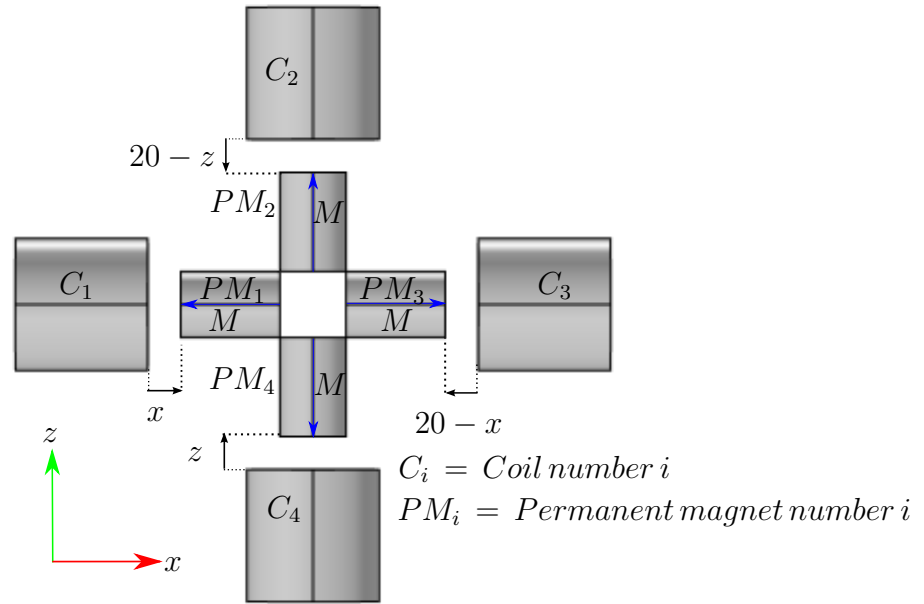


Figure 6.2: Configuration of the magnetic actuator at all axial air gaps.

## 6.2 Force Measurement Results

To validate the model, the results obtained from the closed form model eq 4.18 are compared with those of the experiment. The magnetic force between an electromagnetic coil and a cylindrical permanent magnet was measured using an ATI force sensor. The experimental setup is shown in Figure 6.3.

An electromagnetic coil and permanent magnet were used to validate the force model, having the following dimensions and specifications:

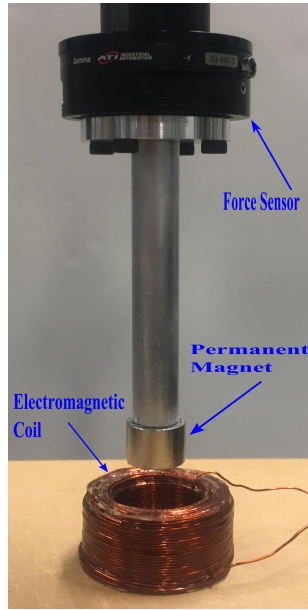


Figure 6.3: Force measurement experimental setup.

Table 6.1: Dimension and specifications of experimental setup.

Coil specifications		Permanent magnet specifications	
$l_c$	$3.5\text{ cm}$	$l_m$	$2.54\text{ cm}$
$R_{ci}$	$2\text{ cm}$	$R_m$	$1.27\text{ cm}$
$R_{co}$	$3.25\text{ cm}$	$B_r$	$1.32\text{ Tesla}$
$V_c$	$71.12\text{ cm}^3$	$V_m$	$12\text{ cm}^3$
Wire and winding specifications			
			AWG17
$R_w$			$0.575\text{ mm}$
$N_z$			30 turn
$N_r$			8 turn
$N$			240 turn

The same procedures were used to obtain the coefficients in eq 4.18 for the new configuration. Figure 6.4 shows a comparison of the experimental results, FEM results, and results obtained from the model in eq 4.18.

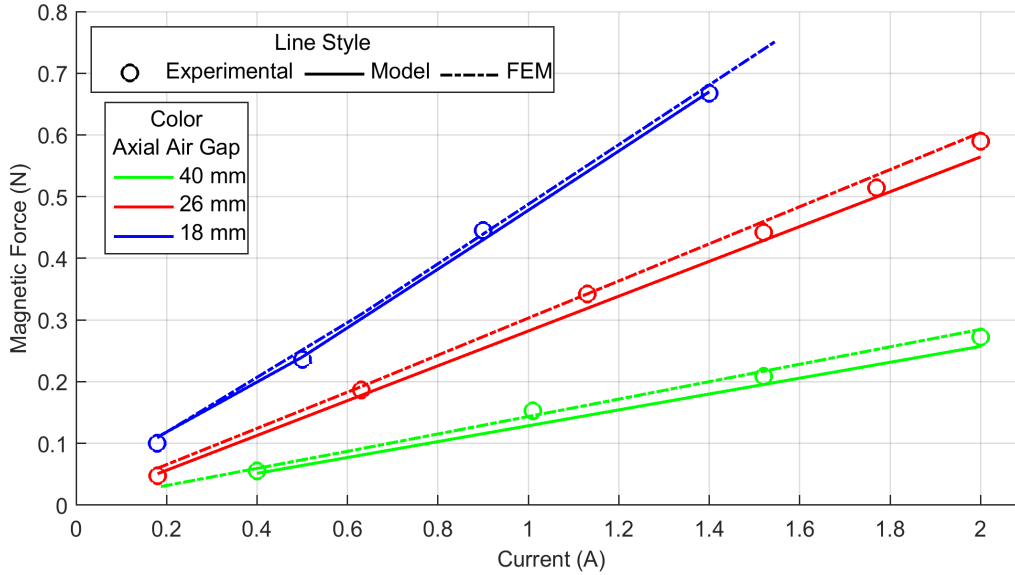


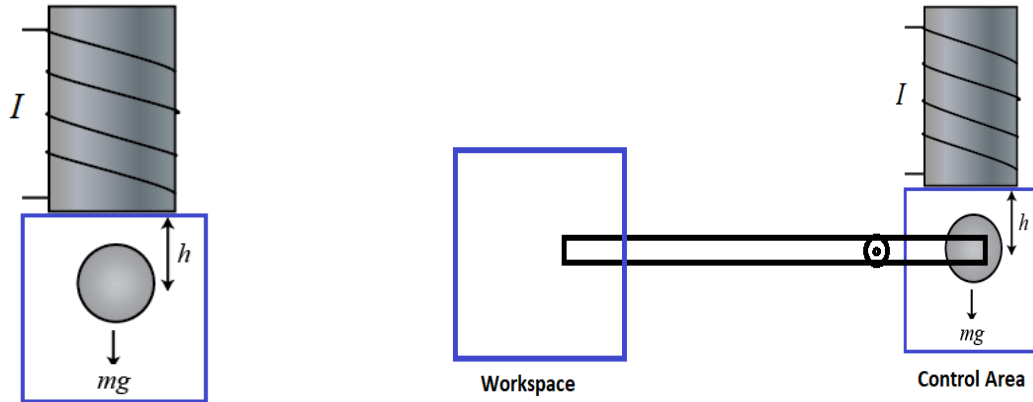
Figure 6.4: A comparison of magnetic force versus excitation current for different axial air gaps based on experimental, analytical, and FEM results.

The model data are in good agreement with the experimental and FEM results over the selected range. The error difference between simulation, experimental, and model data is less than  $0.05\text{ N}$ . These findings demonstrate that the proposed model can be used with an acceptable error to calculate the magnetic force between a cylindrical magnet and a thick electromagnetic coil. Coefficients in eq 4.18 depend on the geometry of the electromagnetic coil and permanent magnet, and future work will focus on the modeling of these coefficients for any given geometry.

### 6.3 Design Advantages

In this work, a new design of an electromagnetic manipulator was presented which has a high actuation force, large workspace, and small drive unit. The system can be considered as a modified version of magnetically levitated robots with a larger workspace and a smaller drive unit. The design has many advantages over other electromagnetic micromanipulators presented in the literature as it has a smaller drive unit and larger workspace. Only five electromagnetic coils were used which is fewer compared to other similar works found in literature.

To demonstrate the effectiveness of the design, comparison of the magnetic levitation ball system which is a benchmark example of freely levitated systems shown in Figure 6.5a below with our system shown in Figure 6.5b is presented.



(a) Magnetic levitation ball system.

(b) Our system.

Figure 6.5: General magnetic levitation system.

Researchers were able to control the magnetic levitation ball system through a range of approximately 1 cm in the vertical axis. This range, in our system, represents  $X_{ix}$  and

$X_{iz}$  in equations (3.16) and (3.17). By multiplying this by  $\frac{15+\beta}{6}$ , given that  $\beta = 3$ , one can achieve a three times larger workspace. In addition, the proposed manipulators in other similar works found in the literature are levitated inside the magnetic field, i.e., the control area is the same as the workspace area, while in our system the end-effector is completely isolated from the controlled magnetic field. In many medical applications this is preferable as the external magnetic field might disturb or interact with other devices or affect the human body. Additionally, due to our design having an isolated workspace from the controlled magnetic field there is lower heating effect in the workspace. Heating effect might affect the manipulated objects in industrial manipulation or affect cells in medical applications.

## 6.4 Position Tracking without payload variations

### 6.4.1 Simulation Results

The dynamic model for the  $z$  axis in Eq (5.8) with the PID controller was simulated using the MatLab-Simulink environment. The PID controllers gains are:  $K_T = 0.6$ ,  $K_P = 300$ ,  $K_I = 5000$  and  $K_D = 1.8$ . The system response for step inputs is shown in Figure 6.6. The response is a second order with a bit of oscillation before reaching the steady state value.



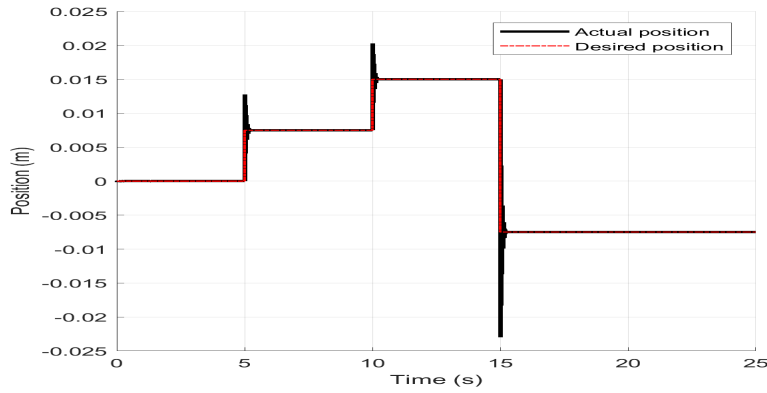


Figure 6.6: Simulation results in the  $z$  axis for the whole workspace.

Similarly, the dynamic model for the  $x$  axis in Eq (5.20) and the dynamic model for the  $y$  axis in Eq (5.23) were simulated for step inputs. The PID controllers gains in the  $x$  axis are:  $K_T = 1$ ,  $K_P = 600$ ,  $K_I = 9500$  and  $K_D = 1.45$ , and in the  $y$  axis are:  $K_P = 85$ ,  $K_D = 0.05$ ,  $K_I = 7500$ ,  $K_T = -0.5$ . The system response for step inputs is shown in Figures 6.7 and 6.8. In both axes, the system is stable and is able to reach the final desired position.

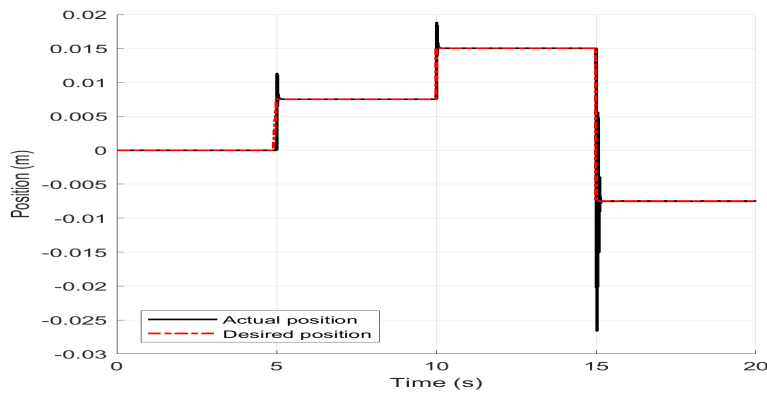


Figure 6.7: Simulation results in the  $x$  axis for the whole workspace.

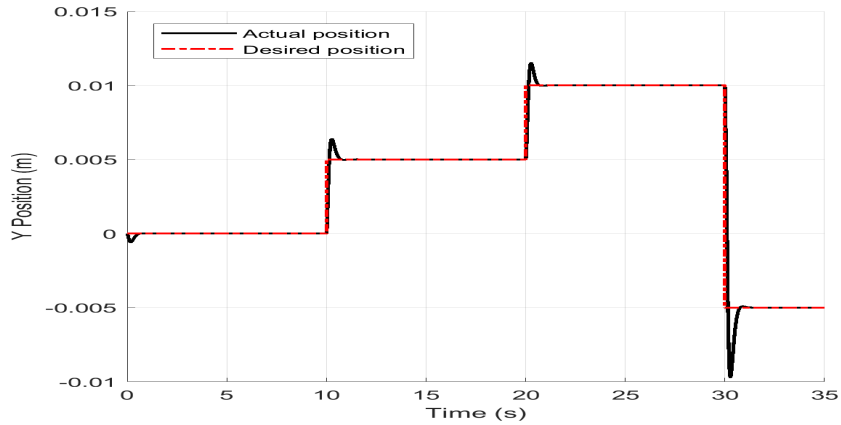


Figure 6.8: Simulation results in the  $y$  axis for the whole workspace.

## 6.4.2 Experimental Setup

The schematic of the experimental setup shown in Figure 6.9 consists of four main components. A main workstation computer that has LabVIEW software to analyze signals and control the instrumentation was used. The computer consists of a National Instrument (NI) 8 slot controller (model PXI-1042) that was used to generate and receive signals. Two laser sensors from KEYENCE (model LK-2101) were used to detect the position of the finger in all axes. Also, a current amplifier that was developed at the University of Waterloo was used to drive the electromagnetic coils.

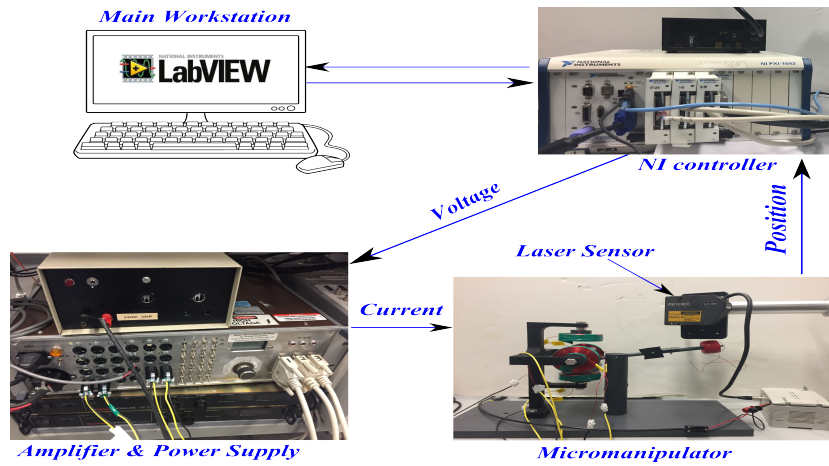


Figure 6.9: Schematic of the experimental setup.

### 6.4.3 PID Controller Experimental Results

The results of the experiment for the  $z$  axis are shown in Figures 6.10, 6.11, and 6.12. Figure 6.10, shows the system response for step inputs similar to the simulation. In general, the response is similar to the simulation results shown in Figure 6.6. However, the oscillation period in the experimental results is a bit larger than the simulation response. This difference may have been caused by incorrect modeling for moment of inertia  $I_x$ .

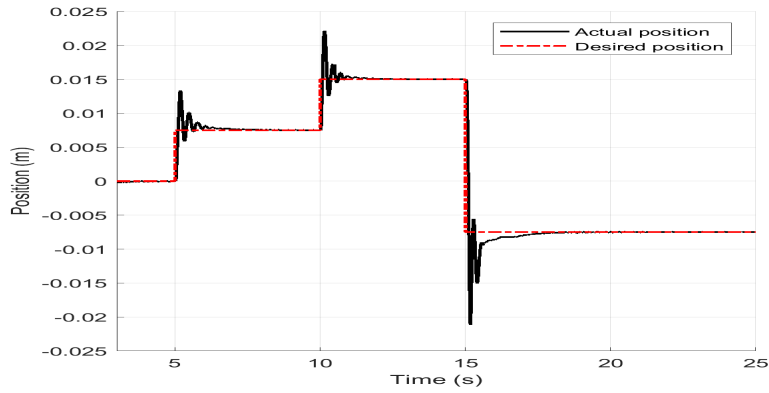


Figure 6.10: Experimental results in the  $z$  axis for the whole workspace.

The system response for ramp type inputs is presented in Figures 6.11 and 6.12. The reference increases from  $-1$  to  $1$   $mm$  in 40 seconds as shown in Figure 6.11, and from  $-2$  to  $2$   $mm$  in 40 seconds as shown in Figure 6.12. As can be seen in both Figures, the micromanipulator is able to follow the reference position with a smooth motion over the whole range of operation.

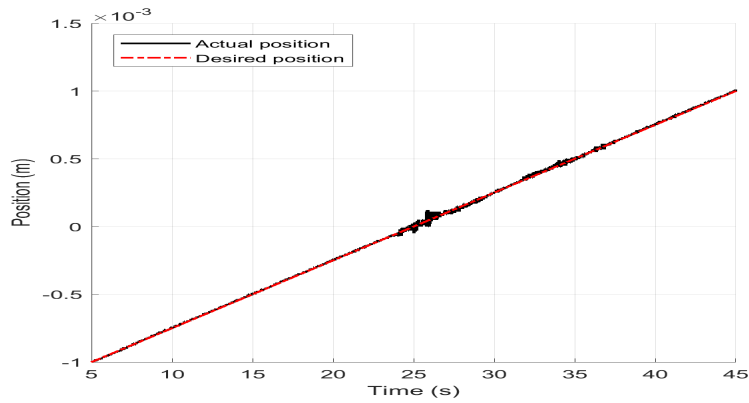


Figure 6.11: Experimental results in the  $z$  axis for a ramp input ( $2$   $mm$  increase).

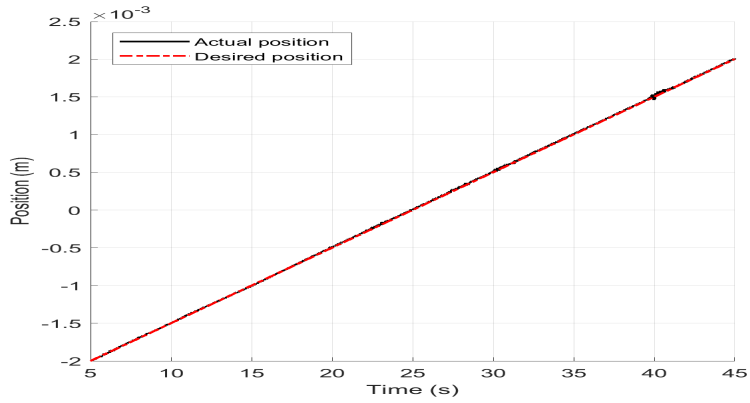


Figure 6.12: Experimental results in the  $z$  axis for a ramp input ( $4\text{ mm}$  increase).

Similarly, the motion of the micromanipulator is also verified experimentally in the  $x$  axis. Figure 6.13 shows the system response for step inputs similar to the simulation presented in Figure 6.7. It is shown that the micromanipulator can follow the desired reference position in the  $x$  axis in a fast and smooth motion with an overshoot and with a zero steady-state error. The response is a second order system as can be seen from eq (5.20).

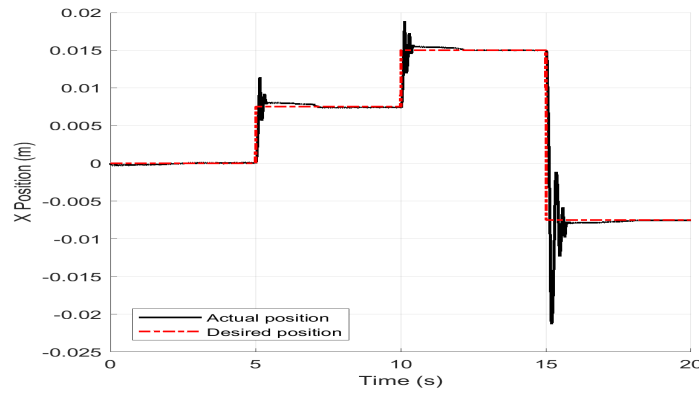


Figure 6.13: Experimental results in the  $x$  axis for the whole workspace.

Figures 6.14 and 6.15 present the motion of the micromanipulator in the  $x$  axis following ramp inputs. In both Figures, the micromanipulator is able to follow the desired path of movement within a negligible error.

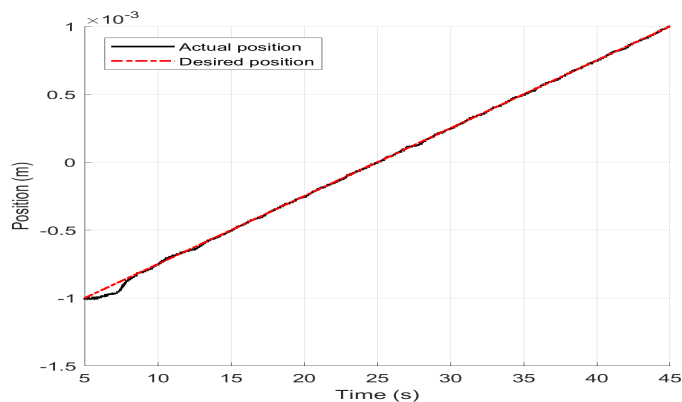


Figure 6.14: Experimental results in the  $z$  axis for a ramp input ( $2\text{ mm}$  increase).

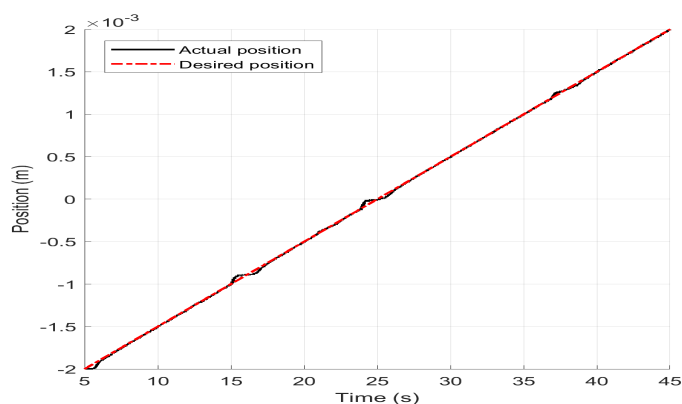


Figure 6.15: Experimental results in the  $x$  axis for a ramp input ( $4\text{ mm}$  increase).

Experimental results for the  $y$  axis are shown in Figures 6.16. Figure 6.16, shows the system response for step inputs similar to the simulation. In general, the response is similar

to the simulation results shown in Figure 6.8. However, the difference between the laser sensor sampling time and the simulation sampling time may explain the undesired motion in the experimental results.

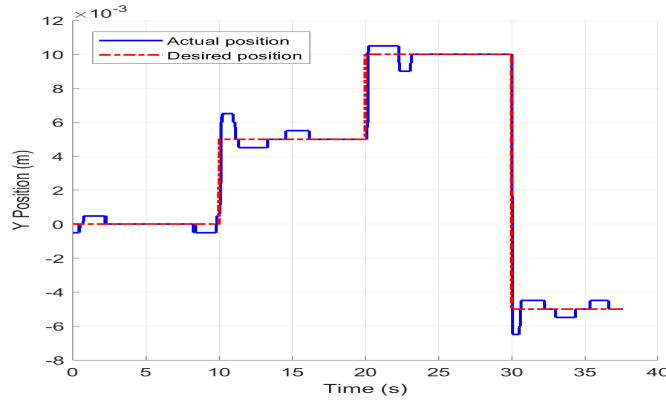


Figure 6.16: Experimental results in the  $y$  axis for the whole workspace.

Table 6.2 compares the performance of the motion in the  $x$ ,  $y$ , and  $z$  axes, where,  $T_p$ ,  $T_r$ , and  $T_s$  are peak time, rise time, and settling time, respectively.  $P.O\%$  is the percentage of overshoot and RMS is the root mean square error in  $m$ . The results, as shown in Table 6.2, indicate that the micromanipulator can follow the desired path and was able to follow rapid movements quickly and with a good response. The tracking error in all axes converges to less than  $10\ \mu\text{m}$ . PID controller gains can be further tuned to improve the settling and peak times at the expense of increased overshoot.

Table 6.2: Performance comparison in  $x$ ,  $y$ , and  $z$  motion.

Performance Criteria		$x$ axis	$z$ axis	$y$ axis
$T_p$	[s]	0.16	0.19	0.22
$T_r$	[s]	0.10	0.11	0.13
$T_s$	[s]	0.95	0.6	3.5
$P.O$	[%]	52	77	20
$RMS$	[m]	$0.21 \times 10^{-3}$	$0.24 \times 10^{-3}$	$0.3 \times 10^{-3}$
Steady-state error	[ $\mu\text{m}$ ]	< 10	< 10	< 10

#### 6.4.4 Workspace Analysis

In the  $x$  and  $z$  axes, the controlling variable is the distance between the permanent magnet and the four way connector which is  $X_{ix}$  and  $X_{iz}$  in equations 3.16 and 3.17 respectively. The maximum controlled motion obtained experimentally was  $\pm 5\text{ mm}$ , and based on that, the micromanipulator end-effector can achieve up to  $\pm 15\text{ mm}$  of workspace in the  $x$  and  $z$  axes. The results obtained show an improvement in motion accuracy and stability compared to similar works mentioned in Chapter 2.

#### 6.4.5 Frequency Domain Analysis

Experiments have been conducted for a range of frequencies less than  $20\text{ Hz}$ . The micromanipulator was programmed to follow the following sine waves:  $0.5 \sin(\omega t)$ ,  $1 \sin(\omega t)$ , and  $2 \sin(\omega t)$ . For each sine wave, the experiment was conducted with the following frequencies:  $f = [0.1, 1, 2, 4]\text{ Hz}$ . In each experiment the excitation signal and the micro-



manipulator position were plotted. In addition, each time the magnitude and phase shift were also plotted. The results are shown in Figures 6.17 to 6.22. Based on them, the micromanipulator bandwidth was found to be  $4\text{ Hz}$ .

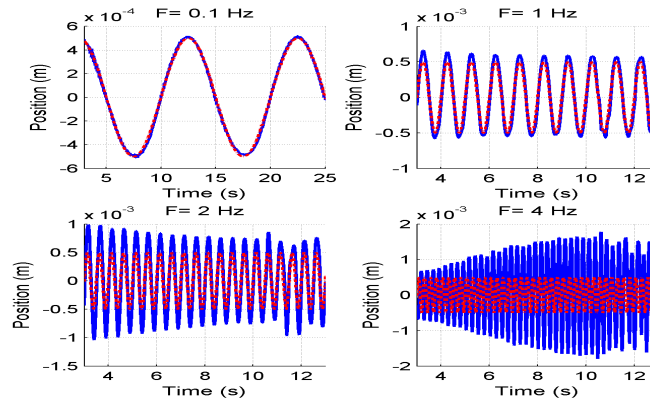


Figure 6.17: Experimental results in the  $z$  axis for  $0.5\sin(\omega t)$  input.

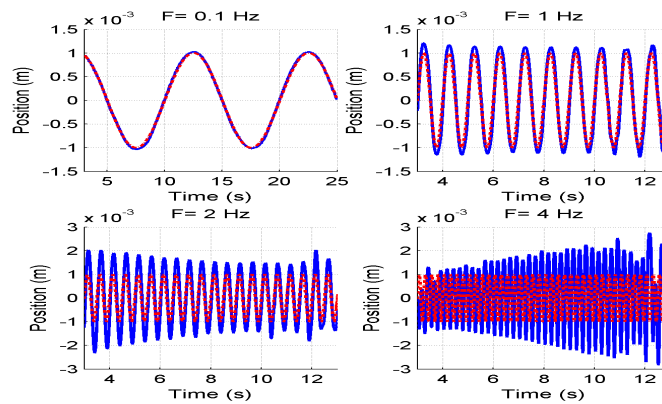


Figure 6.18: Experimental results in the  $z$  axis for  $1\sin(\omega t)$  input.

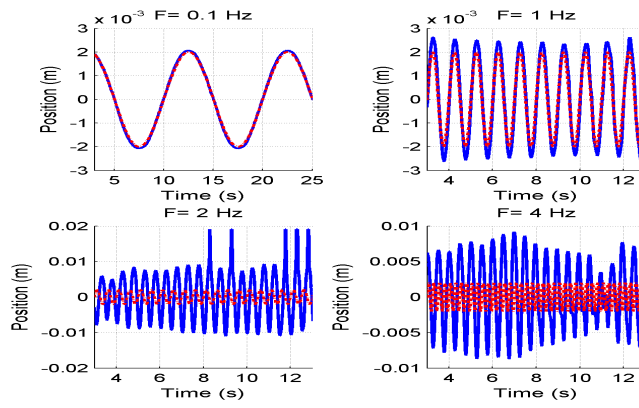


Figure 6.19: Experimental results in the  $z$  axis for  $2\sin(\omega t)$  input.

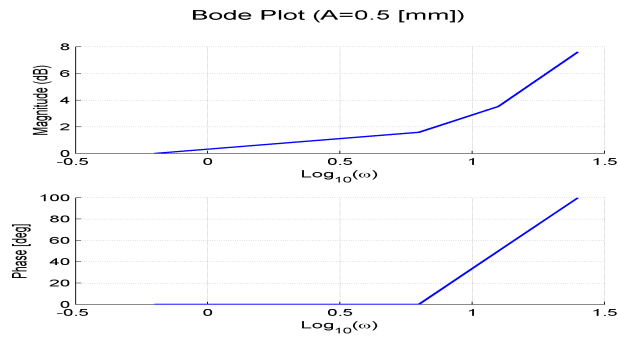


Figure 6.20: Experimental Bode plot in the  $z$  axis for  $0.5\sin(\omega t)$  input.

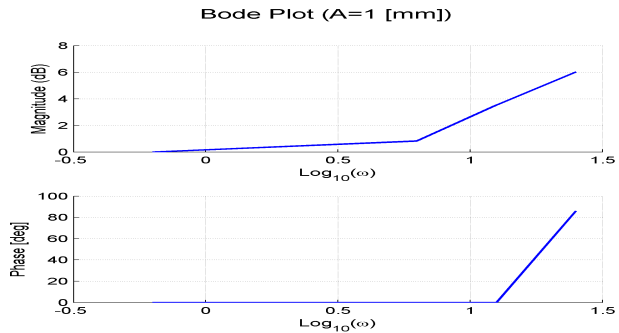


Figure 6.21: Experimental Bode plot in the  $z$  axis for  $1\sin(\omega t)$  input.

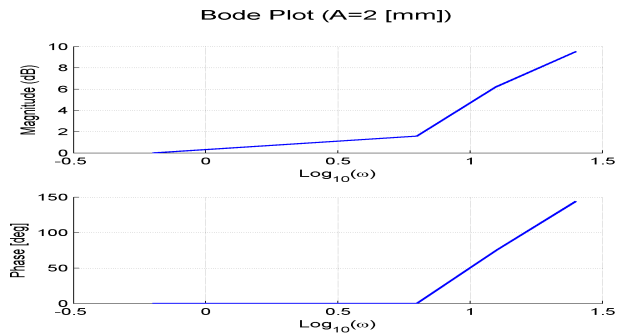


Figure 6.22: Experimental Bode plot in the  $z$  axis for  $2\sin(\omega t)$  input.

## 6.5 Position Tracking with payload variations

### 6.5.1 PID Controller Experimental Results

The system response without any payloads is shown in Figure 6.23. As shown in this Figure, the PID controller is stable and able to guide the micromanipulator to the desired position. As seen in Figures 6.24, and 6.25, when payloads are 25, and 75 g respectively, any changes in the payload affect the performance of the PID control strategy. As noted,

the PID controller suffers from large overshoot, and in order to reduce this overshoot, real-time tuning is required to avoid this undesired performance.

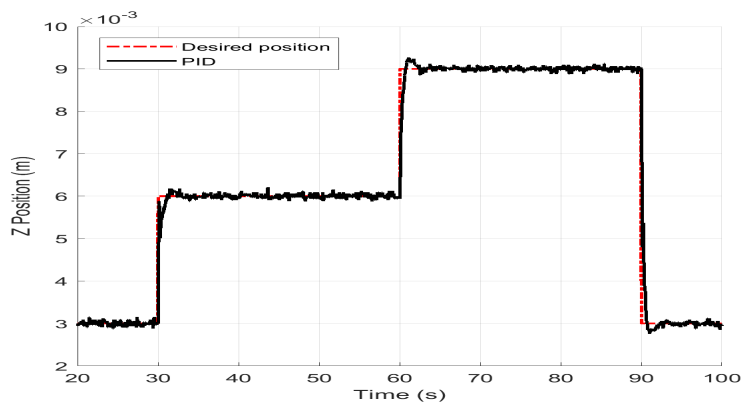


Figure 6.23: Experimental results showing the performance of the PID controller without payload.

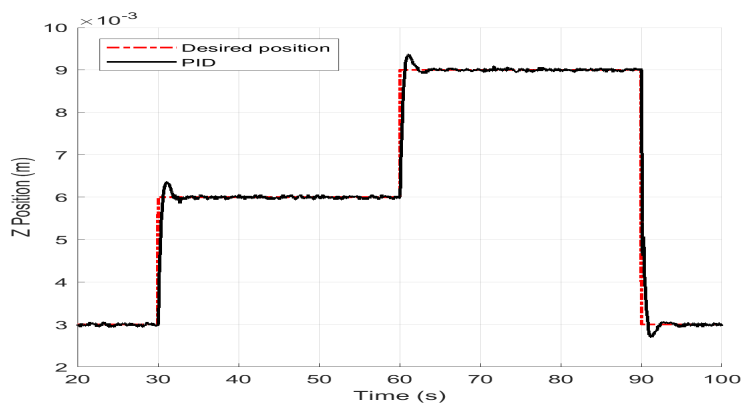


Figure 6.24: Experimental results showing the performance of the PID controller when payload is 25 g.

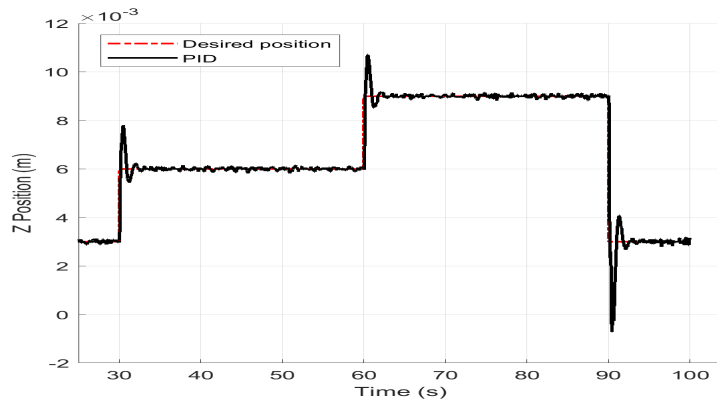


Figure 6.25: Experimental results showing the performance of the PID controller when payload is 75 *g*.

### 6.5.2 State-Feedback Controller Experimental Results

The system response without any payloads is shown in Figure 6.26. As shown, the micro-manipulator motion is stable and smooth, and the micromanipulator follows the desired trajectory with minimum tracking error.

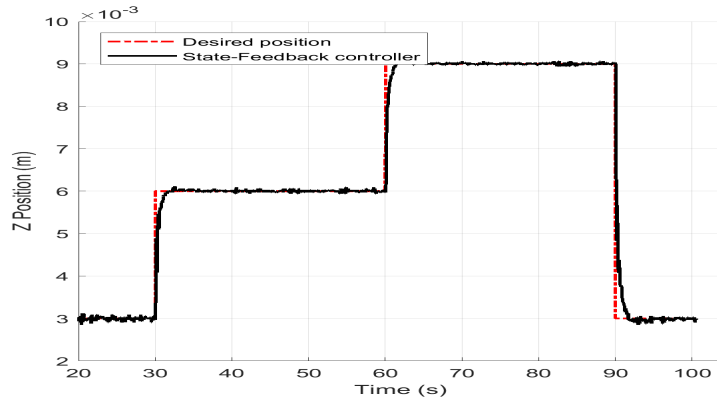


Figure 6.26: Experimental results showing the performance of the state-feedback control algorithm without payload.

As seen in Figures 6.27, and 6.28, when payloads are 25, and 75 *g* respectively, the motion of the micromanipulator becomes not smooth, in addition to having large overshoot. The reason for this undesired motion is that a state-feedback controller requires full pre-knowledge of a system’s dynamic model and linearises it to behave like a linear system. When the payload varies, the system’s dynamic model is changed and that means the state-feedback linearization is not valid anymore, which sequentially affects the motion accuracy and positioning performance.

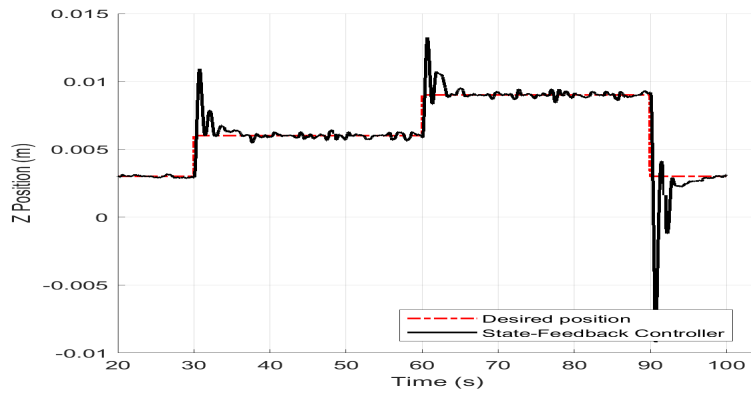


Figure 6.27: Experimental results showing the performance of the state-feedback control algorithm when payload is 25 *g*.

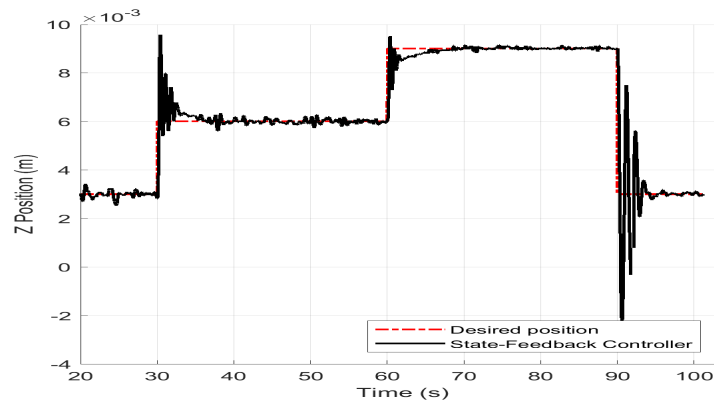


Figure 6.28: Experimental results of the performance of the state-feedback control algorithm when payload is 75 *g*.

As a conclusion, the state-feedback controller that was derived in 5.3 depends on the dynamic model when there is no payload, thus the accuracy of this control strategy affects the overall positioning performance which can be seen in the large overshoot when payloads increase.

### 6.5.3 Adaptive Controller Experimental Results

Figures 6.29, 6.30, and 6.31 show the results of the MRAC adaptive controller when payloads are 0, 25, and 75 g respectively. As seen in these Figures, MRAC response follows the step response regardless of any change in payload. The parameters for the MRAC controller are tuned in the first step response (when time is less than 30 seconds) to compensate for any payload variation. The design parameters chosen for the reference model in eq (5.30) are as follows:  $\omega_n = 1.88 \text{ rad/s}$ , and  $\zeta = 0.71$ . Lastly, the adaptation gain in eq (5.36) was chosen to be  $\gamma = 0.5$ .

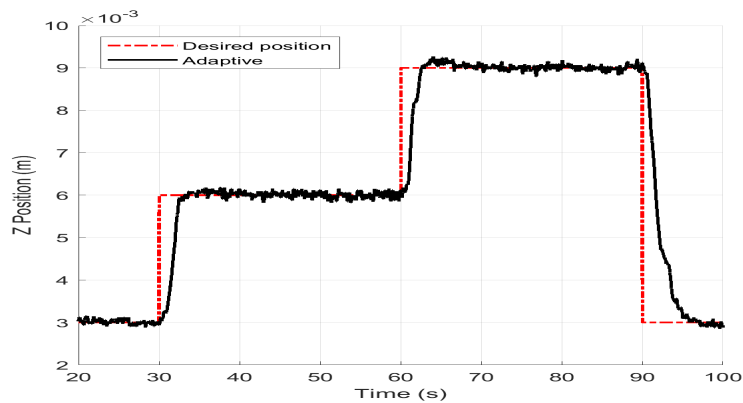


Figure 6.29: Experimental results showing the performance of the adaptive controller without payload.



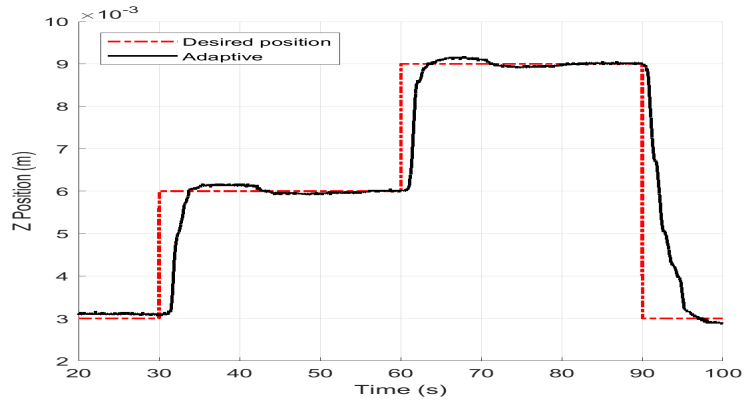


Figure 6.30: Experimental results showing the performance of the adaptive controller when payload is 25 g.

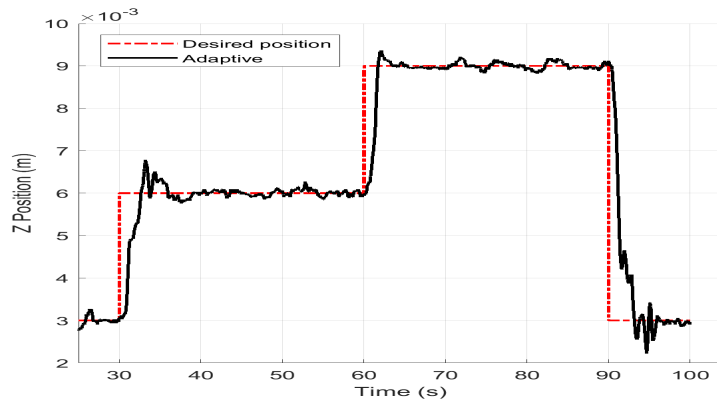


Figure 6.31: Experimental results showing the performance of the adaptive controller when payload is 75 g.

### 6.5.4 Comparison

Table 6.3 compares performance criteria of the PID and the MRAC controllers when the payloads are 0 and 75 g.  $T_p$ ,  $T_r$ , and  $T_s$  are peak time, rise time, and settling time, respec-

tively. Also,  $P.O\%$ , and  $P.U\%$  are the percentage of overshoot and undershoot respectively, and  $RMS$  is the root mean square error in  $mm$ . The results, as shown in Table 6.3, indicate that the manipulator follows the desired position in both control strategies with an acceptable root square error less than  $0.2mm$ . Despite the fact that the PID controller is faster as can be seen from  $T_p$ ,  $T_r$ , and  $T_s$ , it tends to have very large overshoot and undershoot compared to the MRAC controller. Payload variations influence the PID controller response and yield a non smooth motion and may even produce an unstable system. The performance of the MRAC controller, conversely remains almost the same with payload variations. The motion of the manipulator under the MRAC control strategy is smooth regarding the payload variations. Most of the pick-and-place operations require a smooth motion and high stability which make the MRAC controller more preferable compared to the PID controller. As the damping ratio  $\zeta$  in the reference model was chosen to be 0.71, the  $RMS$  using the MRAC controller was high. This value can be decreased in order to lower the  $RMS$  error, however, this would be at the cost of having an underdamped system.

### 6.5.5 Adaptive Controller using the MIT Rule

As found in the literature, MRAC using MIT rule is dependent on the amplitude of the desired input [114, 115]. In order to overcome this problem, a modified MIT rule was used to make the adaptive law independent of the desired input. Using the modified MIT rule, the adaptive law in (5.36) is:

$$\frac{\partial \theta}{\partial t} = \frac{-\gamma e \frac{\partial e}{\partial \theta}}{\alpha + \frac{\partial e^T}{\partial \theta} \frac{\partial e}{\partial \theta}} \quad (6.2)$$

where the parameter  $\alpha$  is a positive number that is used to avoid zero division when  $\frac{\partial e}{\partial \theta}$

Table 6.3: Comparison of performance criteria using PID and MRAC controllers.

Performance Criteria		Without Payload		75 g Payload	
		<i>PID</i>	<i>Adaptive</i>	<i>PID</i>	<i>Adaptive</i>
$T_p$	[s]	0.48	3.69	1.46	3.22
$T_r$	[s]	0.09	1.4	0.65	1.68
$T_s$	[s]	2.27	3.11	2.0	3.67
$P.O$	[%]	3	1.5	30	13
$P.U$	[%]	6	3	124	15
$RMS$	[mm]	0.096	0.129	0.085	0.195

is small. To verify this, we test the performance of the MRAC and the MRAC using the modified MIT rule when following a sinusoidal trajectory with a period of 20 seconds and peak-to-peak amplitude of 6 mm. Figure 6.32 shows the experimental results using the MRAC and the MRAC using modified MIT rule after the learning and self adaptive time (time > 30 s). It can be seen that the manipulator tracks the given sinusoidal trajectory path using the MRAC with modified MIT rule. Figure 6.32 also indicates that the MRAC controller is sensitive to the change in the desired inputs as the manipulator was not able to follow the desired trajectory. Overall, these results indicate that the MRAC using modified MIT rule can guide the manipulator to the desired location regardless of the variation in the desired trajectory.

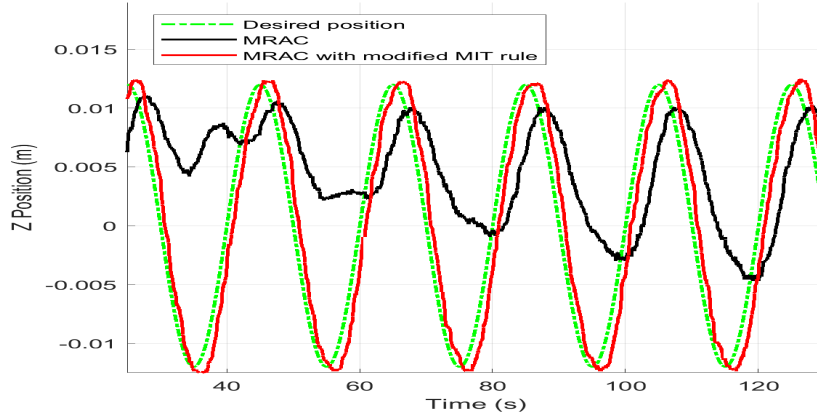


Figure 6.32: Experimental results of MRAC and MRAC with modified MIT rule subjected to a sinusoidal input.

As stated earlier, one of the potential applications of the manipulator is in pick-and-place operations. In order to show the robustness of the system, the system performance for picking and placing an object was tested between two points in the workspace. In this experiment, the manipulator was programmed to pick a 25 g object and move in a straight line from point  $(-0.01, 0, -0.01) m$  to point  $(0.01, 0, 0.01) m$ . Figure 6.33 shows the experimental results using the MRAC controller with modified MIT rule. As seen in the figure, the manipulator reached the final position in a stable and smooth motion.

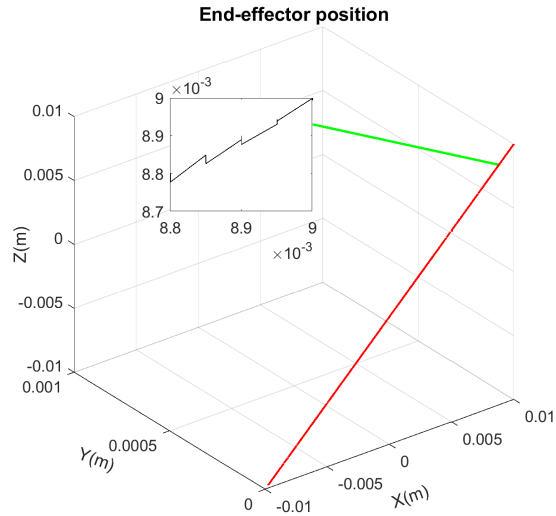


Figure 6.33: Pick-and-place experimental results when payload is 25 *g*.

## 6.6 Load Capacity Analysis

To validate the load capacity capabilities of the presented system, an experiment was conducted to validate equation 3.15. The output force at the end-effector tip was measured using a force sensor with different excitation currents at a fixed air gap of 10 *mm*. The results were compared with the model from equations 3.15, and 5.2, and the results are shown in Figure 6.34. Overall, these results indicate that the system can manipulate objects up to 160 gram.

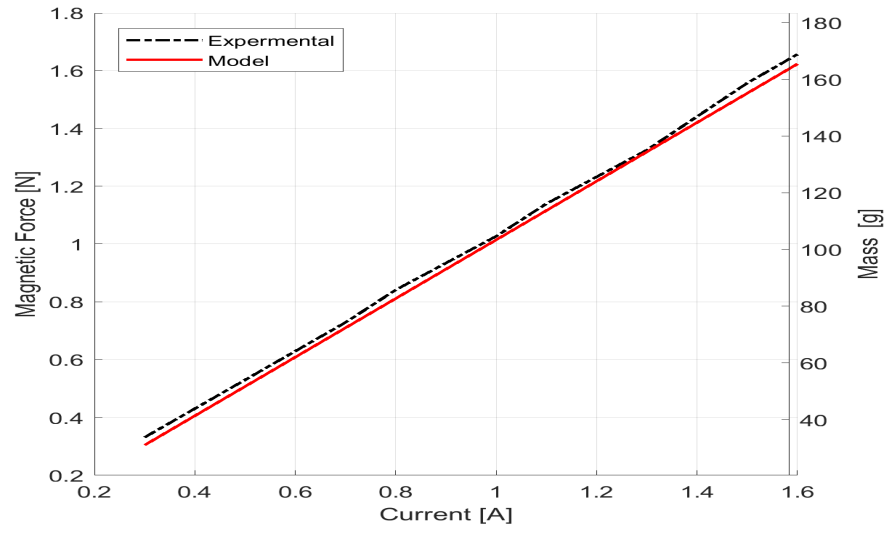


Figure 6.34: Load capacity comparison.

# Chapter 7

## Conclusions and Recommendations

### 7.1 Conclusions

In several applications, electromagnetic actuators are most desirable when performing specific tasks. As found in the literature, most of the proposed magnetically actuated micromanipulators are designed to have a large volume of electromagnetic coils surrounded by a micro-size permanent magnet micromanipulator. In these cases, the micromanipulator has a small workspace area relative to the overall system volume, in addition to the inability to handle heavy payloads, and the need for a large drive unit compared to the size of the levitated object. To overcome these limitations, a novel magnetically levitated manipulator was designed that was adapted from the well-known spherical robot design.

The design has no mechanical gears, which eliminates friction and singularities, and ensures smooth motion in the working environment. As there is no mechanical contact between the drive unit and the levitated manipulator, the system has the ability to be controlled remotely. The overall goal of this research project was to design, optimize, and

build a portable M-DOF magnetically actuated finger micromanipulator, that is small and portable, produces no backlash, can handle heavy loads, and still has a large working space.

The overall system consists of two main subsystems: a magnetic actuator and an electromagnetic end-effector that is connected to the magnetic actuator by a needle. The magnetic actuator consists of four permanent magnets paired with four electromagnetic coils. A finger mechanism with two revolute joints was designed to allow the micromanipulator to move in the workspace. The system is a three DOF micromanipulator that moves along the  $x$  and  $z$  axes, and also moves linearly along the  $y$  axis. Firstly, the design and optimization procedures of the magnetic actuator part was introduced in order to maximize the actuation force. Using the optimized geometry, the generated magnetic force (14.4  $N$ ) was large enough compared to the end-effector desired force. The manipulator needle length is also adjustable to allow a large workspace area and large force ratio. Additionally, a closed form model was developed for the magnetic actuation force. The model was compared and validated with experimental and FEM results. The error difference between the FEM, experimental, and model data was approximately 0.05  $N$ .

The development and experimental characterization for building the micromanipulator were also introduced. The micromanipulator system can be used to address several applications and needs, especially those requiring high-precision, such as, pick-and-place operations, micro assembly, and cell manipulation. The micromanipulator system can be remotely operated by transferring magnetic energy from the outside drive unit. The micromanipulator Jacobian, the micromanipulator workspace, and the micromanipulator kinematic and dynamic models were calculated. The dynamic model was not linear and it was linearized around the operating point. In addition, the position of the end-effector in the  $x$ ,  $y$ , and  $z$  axes was controlled. Therefore, three control algorithms were designed to compute control input currents that are able to control the position of the end-effector in



all axes. The designed controllers were: the PID controller, the state-feedback controller, and the adaptive controller. The experimental results showed that the micromanipulator was able to track the desired trajectory in the  $x$ ,  $y$ , and  $z$  axes with a steady-state error less than  $10\ \mu\text{m}$ .

Lastly, control algorithms were implemented in order to demonstrate the ability of the proposed micromanipulator to address pick-and-place operations for unknown payloads. The manipulator motion under various payloads was tested using PID control, state-feedback control, and model reference adaptive control. For payload free conditions, the experimental results showed the ability of the micromanipulator to follow a desired motion trajectory in all control strategies with a root mean square error less than  $0.2\ \text{mm}$ . Moreover, the results demonstrated a strong effect of payload variations on the PID controller performance and the state feedback controller, while it had no effect on the performance of the model reference adaptive controller.

The micromanipulator successfully handled payloads up to 75 grams and the motion range was  $\pm 15\ \text{mm}$  in each axis. Importantly, the results provided evidence for using the proposed system as a potential manipulator that targets industrial manipulation. Future studies are recommended to allow replication of results at the micro scale level.

## 7.2 Recommendations

Electromagnetic actuation technology, providing frictionless motions and precise motion control, has promising potential applications in many fields. Although the proposed micromanipulator was successfully tested experimentally to address pick-and-place operations for unknown payloads and the obtained results are promising, it is evident that much future research is required to be done in order to improve the micromanipulator performance in terms of motion, speed, and accuracy.

First, the position controller loop can be enhanced with a 3D position sensor attached to the micromanipulator in order to track the location of the end-effector position. Using separate laser sensors in each axis would positively influence the motion coupling accuracy.

Second, force model correction schemes in the case of motion coupling can be designed that would improve the controller performance. The controller herein used the derived force model to guide the micromanipulator in the workspace. The axial magnetic force between a cylindrical magnet and electromagnetic coil was modeled, but during motion the force is not axially aligned and therefore implementing a force model correction would enhance the motion and force accuracy.

Third, the micromanipulator can be used as a mass or force sensing device at the end-effector tip. Therefore, implementing robust techniques to estimate the payload variations at the end-effector tip and indirectly include them in the position control loop would definitely improve the manipulation motion and accuracy. In addition, a hybrid position and force controller could be applied and that would broaden the application range of the system.

# APPENDICES

# Appendix A

## The Shell Method Calculations

The axial magnetic force  $F_m$  between a cylindrical magnet and electromagnetic coil can be found using the shell method as follows in A.1:

$$F_m = \frac{1}{N_r} \sum_{n_r=1}^{N_r} F_s(R_m, r(n_r), l_m, l_c, z + \frac{l_m + l_c}{2}) \quad (\text{A.1})$$

Where:

$$r(n_r) = R_{ci} + \frac{n_r + 1}{N_r + 1} (R_{co} - R_{ci}) \quad (\text{A.2})$$

$$F_s(R_m, r, l_m, l_c, z + \frac{l_m + l_c}{2}) = \frac{J_1 J_2}{2M_0} \sum_{e_1=1}^{e_1=2} \sum_{e_2=3}^{e_2=4} e_1 e_2 m_1 m_2 m_3 F_x \quad (\text{A.3})$$

$$J_2 = \frac{\mu_0 N_z I}{l_c} \quad (\text{A.4})$$

$$J_1 = B_r \tag{A.5}$$

$$F_x = K(m_4) - \frac{1}{m_2}E(m_4) + \left[\frac{m_1^2}{m_3^2} - 1\right] \Pi\left(\frac{m_4}{1 - m_2} \mid m_4\right) \tag{A.6}$$

$$m_1 = z + \frac{l_m + l_c}{2} - \frac{1}{2}e_1 l_m + \frac{1}{2}e_1 l_c \tag{A.7}$$

$$m_2 = \frac{(R_m - r)^2}{m_1} + 1 \tag{A.8}$$

$$m_3 = \sqrt{(R_m + r)^2 + m_1^2} \tag{A.9}$$

$$m_4 = \frac{4R_m r}{m_3} \tag{A.10}$$

# Appendix B

## The Micromanipulator CAD Drawing

The micromanipulator complete CAD drawing is shown in the following Figure B.1:

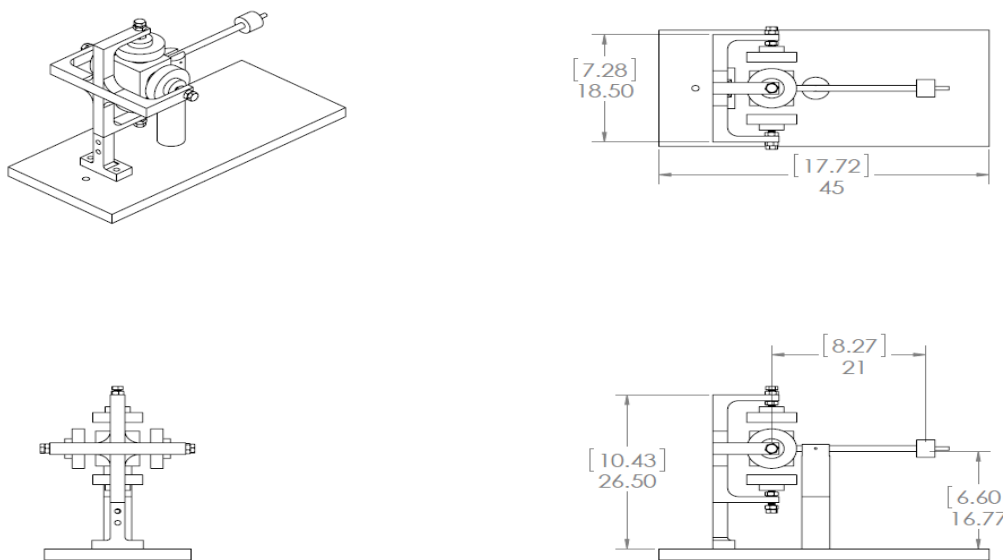


Figure B.1: Schematic CAD drawing of the micromanipulator.

# Letter of Copyright Permissions

**SPRINGER NATURE**

**Accept your approved request**

Dear Mr. Mohammad Al Mashagbeh,

Springer Nature has approved your recent request described below. Before you can use this content, **you must accept** the license fee and terms set by the publisher.

Use this [link](#) to accept (or decline) the publisher's fee and terms for this order.

**Order Summary**


Licensee: Mr. Mohammad Mashagbeh  
Order Date: May 30, 2018  
Order Number: 501404212  
Publication: Microsystem Technologies  
Title: Design and optimization of a novel magnetically-actuated micromanipulator  
Type of Use: Thesis/Dissertation

View or [print complete details](#) of your request.

Sincerely,  
Copyright Clearance Center

Tel: +1-855-239-3415 / +1-978-646-2777  
customerare@copyright.com  
<https://myaccount.copyright.com>

 Copyright Clearance Center

 RightsLink®

# References

- [1] M. P. Kummer, J. J. Abbott, B. E. Kratochvil, R. Borer, A. Sengul, and B. J. Nelson, “Octomag: An electromagnetic system for 5-dof wireless micromanipulation,” *IEEE Transactions on Robotics*, vol. 26, no. 6, pp. 1006–1017, 2010.
- [2] E. Avci, K. Ohara, T. Takubo, Y. Mae, and T. Arai, “A new multi-scale micromanipulation system with dexterous motion,” in *Micro-NanoMechatronics and Human Science, 2009. MHS 2009. International Symposium on*, pp. 444–449, IEEE, 2009.
- [3] X. Zhang and M. B. Khamesee, “Magnetically driven microrobotics for micromanipulation and biomedical applications,” in *Advanced Mechatronics and MEMS Devices II*, pp. 613–635, Springer, 2017.
- [4] M. De Volder, F. Ceyssens, D. Reynaerts, and R. Puers, “A pdms lipseal for hydraulic and pneumatic microactuators,” *Journal of Micromechanics and microengineering*, vol. 17, no. 7, p. 1232, 2007.
- [5] M. De Volder and D. Reynaerts, “Pneumatic and hydraulic microactuators: a review,” *Journal of Micromechanics and microengineering*, vol. 20, no. 4, p. 043001, 2010.



- [6] S. R. Pandian, Y. Hayakawa, Y. Kanazawa, Y. Kamoyama, and S. Kawamura, “Practical design of a sliding mode controller for pneumatic actuators,” *Journal of dynamic systems, measurement, and control*, vol. 119, no. 4, pp. 666–674, 1997.
- [7] Q.-M. Wang, Q. Zhang, B. Xu, R. Liu, and L. E. Cross, “Nonlinear piezoelectric behavior of ceramic bending mode actuators under strong electric fields,” *Journal of Applied Physics*, vol. 86, no. 6, pp. 3352–3360, 1999.
- [8] H. P. Syahputra, H. M. Yang, B. M. Chung, and T. J. Ko, “Dual-stage feed drive for precision positioning on milling machine,” in *International Precision Assembly Seminar*, pp. 81–88, Springer, 2012.
- [9] B. M. Badr and W. G. Ali, “Applications of piezoelectric materials,” in *Advanced Materials Research*, vol. 189, pp. 3612–3620, Trans Tech Publ, 2011.
- [10] D. Wang, Q. Yang, and H. Dong, “A monolithic compliant piezoelectric-driven micro-gripper: Design, modeling, and testing,” *IEEE/ASME Transactions on mechatronics*, vol. 18, no. 1, pp. 138–147, 2013.
- [11] S. I. Company, “Mm-33 micromanipulator.” <http://www.sutter.com/MICROMANIPULATION/index.html>.
- [12] N. Group., “Emm-3nv three-axis motorized micromanipulator.” <http://products.narishige-group.com/group1/EMM-3NV/electro/english.html>.
- [13] S. Co, “hydraulic joystick driven micromanipulators.” <http://www.stoeltingco.com/neuroscience/micromanipulators/hydraulic/hydraulic-joystick-driven.html>.

- [14] W. P. Instruments., “Miniature piezo micromanipulator.” <https://www.wpiinc.com/products/top-products/sn-pz-501-miniature-piezo-micromanipulator-lh/>.
- [15] J. Wang, N. Jiao, S. Tung, and L. Liu, “Automatic path tracking and target manipulation of a magnetic microrobot,” *Micromachines*, vol. 7, no. 11, p. 212, 2016.
- [16] T. Mei, Y. Chen, G. Fu, and D. Kong, “Wireless drive and control of a swimming microrobot,” in *Robotics and Automation, 2002. Proceedings. ICRA’02. IEEE International Conference on*, vol. 2, pp. 1131–1136, IEEE, 2002.
- [17] Y. Ko, S. Na, Y. Lee, K. Cha, S. Y. Ko, J. Park, and S. Park, “A jellyfish-like swimming mini-robot actuated by an electromagnetic actuation system,” *Smart Materials and Structures*, vol. 21, no. 5, p. 057001, 2012.
- [18] Q. Zhang, Y. Wang, and E. S. Kim, “Electromagnetic energy harvester with flexible coils and magnetic spring for 1–10 hz resonance,” *Journal of Microelectromechanical Systems*, vol. 24, no. 4, pp. 1193–1206, 2015.
- [19] N. Garbin, C. Di Natali, J. Buzzi, E. De Momi, and P. Valdastri, “Laparoscopic tissue retractor based on local magnetic actuation,” *Journal of Medical Devices*, vol. 9, no. 1, p. 011005, 2015.
- [20] M. Simi, R. Pickens, A. Menciassi, S. D. Herrell, and P. Valdastri, “Fine tilt tuning of a laparoscopic camera by local magnetic actuation: two-port nephrectomy experience on human cadavers,” *Surgical innovation*, vol. 20, no. 4, pp. 385–394, 2013.
- [21] Y. Dong, F. Gao, and Y. Yue, “Modeling and experimental study of a novel 3-rpr parallel micro-manipulator,” *Robotics and Computer-Integrated Manufacturing*, vol. 37, pp. 115–124, 2016.

- [22] M. Han, Q. Yuan, X. Sun, and H. Zhang, “Design and fabrication of integrated magnetic mems energy harvester for low frequency applications,” *Journal of Microelectromechanical Systems*, vol. 23, no. 1, pp. 204–212, 2014.
- [23] Y. Li, J. Kim, M. Kim, A. Armutlulu, and M. G. Allen, “Thick multilayered micromachined permanent magnets with preserved magnetic properties,” *Journal of Microelectromechanical Systems*, vol. 25, no. 3, pp. 498–507, 2016.
- [24] Q. Zhang and E. S. Kim, “Micromachined energy-harvester stack with enhanced electromagnetic induction through vertical integration of magnets,” *Journal of Microelectromechanical Systems*, vol. 24, no. 2, pp. 384–394, 2015.
- [25] W. P. Taylor, O. Brand, and M. G. Allen, “Fully integrated magnetically actuated micromachined relays,” *Journal of Microelectromechanical Systems*, vol. 7, no. 2, pp. 181–191, 1998.
- [26] J. W. Judy and R. S. Muller, “Magnetically actuated, addressable microstructures,” *Journal of Microelectromechanical systems*, vol. 6, no. 3, pp. 249–256, 1997.
- [27] M. B. Khamesee, N. Kato, Y. Nomura, and T. Nakamura, “Design and control of a microrobotic system using magnetic levitation,” *IEEE/ASME transactions on mechatronics*, vol. 7, no. 1, pp. 1–14, 2002.
- [28] P. Berkelman and M. Dzadovsky, “Magnetic levitation over large translation and rotation ranges in all directions,” *IEEE/ASME Transactions on Mechatronics*, vol. 18, no. 1, pp. 44–52, 2013.
- [29] H. Choi, J. Choi, S. Jeong, C. Yu, J.-o. Park, and S. Park, “Two-dimensional locomotion of a microrobot with a novel stationary electromagnetic actuation system,” *Smart Materials and Structures*, vol. 18, no. 11, p. 115017, 2009.

- [30] X. Xiao, Y. Li, and S. Xiao, "Development of a novel large stroke 2-dof micromanipulator for micro/nano manipulation," *Microsystem Technologies*, pp. 1–11, 2016.
- [31] X. Xiao and Y. Li, "Development of an electromagnetic actuated microdisplacement module," *IEEE/ASME Transactions on Mechatronics*, vol. 21, no. 3, pp. 1252–1261, 2016.
- [32] G. Go, D. Kwak, L. Piao, H. Choi, S. Jeong, C. Lee, B. J. Park, S. Y. Ko, J.-o. Park, and S. Park, "Manipulation of micro-particles using a magnetically actuated microrobot," *Mechatronics*, vol. 23, no. 8, pp. 1037–1043, 2013.
- [33] H. Technologies, "Voice coil actuators." <https://www.h2wtech.com/article/voice-coil-actuators-vs-solenoids>.
- [34] L. Zheng, L.-g. Chen, H.-b. Huang, X.-p. Li, and L.-l. Zhang, "An overview of magnetic micro-robot systems for biomedical applications," *Microsystem Technologies*, pp. 1–17, 2016.
- [35] K. Ikuta, S. Makita, and S. Arimoto, "Non-contact magnetic gear for micro transmission mechanism," in *Micro Electro Mechanical Systems, 1991, MEMS'91, Proceedings. An Investigation of Micro Structures, Sensors, Actuators, Machines and Robots. IEEE*, pp. 125–130, IEEE, 1991.
- [36] C. Liu, T. Stakenborg, S. Peeters, and L. Lagae, "Cell manipulation with magnetic particles toward microfluidic cytometry," *Journal of Applied Physics*, vol. 105, no. 10, p. 102014, 2009.
- [37] J. F. Testa and C. C. Camuso, "Magnetic tool and object holder," June 2 1998. US Patent 5,760,668.

- [38] M. Li, V. T. Rouf, M. J. Thompson, and D. A. Horsley, “Three-axis lorentz-force magnetic sensor for electronic compass applications,” *Journal of Microelectromechanical Systems*, vol. 21, no. 4, pp. 1002–1010, 2012.
- [39] M. Andriollo, G. Martinelli, and A. Tortella, “Optimization of an electrodynamic linear actuator for biometric applications,” *IEEE Transactions on Magnetics*, vol. 51, no. 8, pp. 1–6, 2015.
- [40] K. Weise, M. Carlstedt, M. Ziolkowski, H. Brauer, and H. Toepfer, “Lorentz force on permanent magnet rings by moving electrical conductors,” *IEEE Transactions on Magnetics*, vol. 51, no. 12, pp. 1–11, 2015.
- [41] A. Okyay, M. B. Khamesee, and K. Erkorkmaz, “Design and optimization of a voice coil actuator for precision motion applications,” *IEEE Transactions on Magnetics*, vol. 51, no. 6, pp. 1–10, 2015.
- [42] D. G. Seo, W. Han, and Y.-H. Cho, “A compact electromagnetic micro-actuator using the meander springs partially exposed to magnetic field,” *Microsystem Technologies*, vol. 21, no. 6, pp. 1233–1239, 2015.
- [43] S. Guo, Q. Pan, and M. B. Khamesee, “Development of a novel type of microrobot for biomedical application,” *Microsystem Technologies*, vol. 14, no. 3, pp. 307–314, 2008.
- [44] B. G. Hosu, K. Jakab, P. Bánki, F. I. Tóth, and G. Forgacs, “Magnetic tweezers for intracellular applications,” *Review of Scientific Instruments*, vol. 74, no. 9, pp. 4158–4163, 2003.

- [45] A. H. de Vries, B. E. Krenn, R. van Driel, and J. S. Kanger, “Micro magnetic tweezers for nanomanipulation inside live cells,” *Biophysical journal*, vol. 88, no. 3, pp. 2137–2144, 2005.
- [46] M. Dkhil, A. Bolopion, S. Régnier, and M. Gauthier, “Modeling and experiments of high speed magnetic micromanipulation at the air/liquid interface,” in *2014 IEEE/RSJ International Conference on Intelligent Robots and Systems*, pp. 4649–4655, IEEE, 2014.
- [47] F. Niu, W. Ma, H. K. Chu, H. Ji, J. Yang, and D. Sun, “An electromagnetic system for magnetic microbead’s manipulation,” in *2015 IEEE International Conference on Mechatronics and Automation (ICMA)*, pp. 1005–1010, IEEE, 2015.
- [48] M. Mehrtash, N. Tsuda, and M. B. Khamesee, “Bilateral macro–micro teleoperation using magnetic levitation,” *IEEE/ASME Transactions on Mechatronics*, vol. 16, no. 3, pp. 459–469, 2011.
- [49] M. Mehrtash and M. B. Khamesee, “Optimal motion control of magnetically levitated microrobot,” in *2010 IEEE International Conference on Automation Science and Engineering*, pp. 521–526, IEEE, 2010.
- [50] S. Tarao, M. Mehrtash, N. Tsuda, and M. B. Khamesee, “Motion simulator for a multi-degree-of-freedom magnetically levitated robot,” in *System Integration (SII), 2011 IEEE/SICE International Symposium on*, pp. 869–874, IEEE, 2011.
- [51] M. Mehrtash, M. B. Khamesee, N. Tsuda, and J.-Y. Chang, “Motion control of a magnetically levitated microrobot using magnetic flux measurement,” *Microsystem technologies*, vol. 18, no. 9-10, pp. 1417–1424, 2012.

- [52] X. Zhang, M. Mehrtash, and M. B. Khamesee, “Dual-axial motion control of a magnetic levitation system using hall-effect sensors,” *IEEE/ASME Transactions on Mechatronics*, vol. 21, no. 2, pp. 1129–1139, 2016.
- [53] M. Mehrtash, X. Zhang, and M. B. Khamesee, “Bilateral magnetic micromanipulation using off-board force sensor,” *IEEE/ASME Transactions on Mechatronics*, vol. 20, no. 6, pp. 3223–3231, 2015.
- [54] S. Afshar, M. B. Khamesee, and A. Khajepour, “Optimal configuration for electromagnets and coils in magnetic actuators,” *IEEE Transactions on Magnetics*, vol. 49, no. 4, pp. 1372–1381, 2013.
- [55] M. Farina, A. Ballerini, G. Torchio, G. Rizzo, D. Demarchi, U. Thekkedath, and A. Grattoni, “Remote magnetic switch off microgate for nanofluidic drug delivery implants,” *Biomedical microdevices*, vol. 19, no. 2, p. 42, 2017.
- [56] A. Mohammadi, D. Samsonas, F. Leong, Y. Tan, D. Thiruchelvam, P. Valdastrri, and D. Oetomo, “Modeling and control of local electromagnetic actuation for robotic-assisted surgical devices,” *IEEE/ASME Transactions on Mechatronics*, vol. 22, no. 6, pp. 2449–2460, 2017.
- [57] H. S. Zad, T. I. Khan, and I. Lazoglu, “Design and adaptive sliding-mode control of hybrid magnetic bearings,” *IEEE Transactions on Industrial Electronics*, vol. 65, no. 3, pp. 2537–2547, 2018.
- [58] L. Zhuchong, L. Kun, and Z. Wei, “Inertially stabilized platform for airborne remote sensing using magnetic bearings,” *IEEE/ASME Transactions on Mechatronics*, vol. 21, no. 1, pp. 288–301, 2016.

- [59] C. Pacchierotti, F. Ongaro, F. Van den Brink, C. Yoon, D. Prattichizzo, D. H. Gracias, and S. Misra, “Steering and control of miniaturized untethered soft magnetic grippers with haptic assistance,” *IEEE transactions on automation science and engineering*, vol. 15, no. 1, pp. 290–306, 2018.
- [60] H. Zhou, H. Deng, and J. Duan, “Hybrid fuzzy decoupling control for a precision maglev motion system,” *IEEE/ASME Transactions on Mechatronics*, 2017.
- [61] U. Hasirci, A. Balikci, Z. Zabar, and L. Birenbaum, “A novel magnetic-levitation system: design, implementation, and nonlinear control,” *IEEE Transactions on Plasma Science*, vol. 39, no. 1, pp. 492–497, 2011.
- [62] Y. Xie, Y. Tan, and R. Dong, “Nonlinear modeling and decoupling control of xy micropositioning stages with piezoelectric actuators,” *IEEE/ASME Transactions on Mechatronics*, vol. 18, no. 3, pp. 821–832, 2013.
- [63] J. Pinskiere, B. Shirinzadeh, L. Clark, Y. Qin, and S. Fatikow, “Design, development and analysis of a haptic-enabled modular flexure-based manipulator,” *Mechatronics*, vol. 40, pp. 156–166, 2016.
- [64] Y. Li and Z. Wu, “Design, analysis and simulation of a novel 3-dof translational micromanipulator based on the prb model,” *Mechanism and Machine Theory*, vol. 100, pp. 235–258, 2016.
- [65] I. S. Park, J. H. Shin, Y. R. Lee, and S. K. Chung, “On-chip micromanipulation using a magnetically driven micromanipulator with an acoustically oscillating bubble,” *Sensors and Actuators A: Physical*, vol. 248, pp. 214–222, 2016.



- [66] A. AbuZaiter, M. Nafea, and M. S. M. Ali, “Development of a shape-memory-alloy micromanipulator based on integrated bimorph microactuators,” *Mechatronics*, vol. 38, pp. 16–28, 2016.
- [67] J. Yu, Y. Xie, Z. Li, and G. Hao, “Design and experimental testing of an improved large-range decoupled xy compliant parallel micromanipulator,” *Journal of Mechanisms and Robotics*, vol. 7, no. 4, p. 044503, 2015.
- [68] B. Gonenc, E. Feldman, P. Gehlbach, J. Handa, R. H. Taylor, and I. Iordachita, “Towards robot-assisted vitreoretinal surgery: Force-sensing micro-forceps integrated with a handheld micromanipulator,” in *Robotics and Automation (ICRA), 2014 IEEE International Conference on*, pp. 1399–1404, IEEE, 2014.
- [69] Y. Ohya, T. Arai, Y. Mae, K. Inoue, and T. Tanikawa, “Development of 3-dof finger module for micro manipulation,” in *Intelligent Robots and Systems, 1999. IROS’99. Proceedings. 1999 IEEE/RSJ International Conference on*, vol. 2, pp. 894–899, IEEE, 1999.
- [70] R. Yeh, E. J. Kruglick, and K. S. Pister, “Surface-micromachined components for articulated microrobots,” *Journal of Microelectromechanical Systems*, vol. 5, no. 1, pp. 10–17, 1996.
- [71] S. Hasanzadeh, F. Janabi-Sharifi, and P. Keenan, “Backlash characterization and position control of a robotic catheter manipulator using experimentally-based kinematic model,” *Mechatronics*, vol. 44, pp. 94–106, 2017.
- [72] C.-L. Kuo, T.-H. S. Li, and N. R. Guo, “Design of a novel fuzzy sliding-mode control for magnetic ball levitation system,” *Journal of intelligent and Robotic Systems*, vol. 42, no. 3, pp. 295–316, 2005.

- [73] R. Morales, V. Feliu, and H. Sira-Ramirez, “Nonlinear control for magnetic levitation systems based on fast online algebraic identification of the input gain,” *IEEE Transactions on Control Systems Technology*, vol. 19, no. 4, pp. 757–771, 2011.
- [74] Z.-J. Yang, K. Miyazaki, S. Kanae, and K. Wada, “Robust position control of a magnetic levitation system via dynamic surface control technique,” *IEEE Transactions on Industrial Electronics*, vol. 51, no. 1, pp. 26–34, 2004.
- [75] S. Xiao and Y. Li, “Optimal design, fabrication, and control of an  $xy$  micropositioning stage driven by electromagnetic actuators,” *IEEE transactions on Industrial Electronics*, vol. 60, no. 10, pp. 4613–4626, 2013.
- [76] M. U. Khan, N. Bencheikh, C. Prelle, F. Lamarque, T. Beutel, and S. Buttgenbach, “A long stroke electromagnetic  $xy$  positioning stage for micro applications,” *IEEE/ASME Transactions on Mechatronics*, vol. 17, no. 5, pp. 866–875, 2012.
- [77] S. Verma, W.-J. Kim, and H. Shakir, “Multiaxis maglev nanopositioner for precision manufacturing and manipulation applications,” in *Industry Applications Conference, 2004. 39th IAS Annual Meeting. Conference Record of the 2004 IEEE*, vol. 3, pp. 2084–2091, IEEE, 2004.
- [78] V. H. Nguyen and W.-j. Kim, “Two-phase lorentz coils and linear halbach array for multiaxis precision-positioning stages with magnetic levitation,” *IEEE/ASME Transactions on Mechatronics*, vol. 22, no. 6, pp. 2662–2672, 2017.
- [79] R. L. Hollis, S. E. Salcudean, and A. P. Allan, “A six-degree-of-freedom magnetically levitated variable compliance fine-motion wrist: design, modeling, and control,” *IEEE Transactions on Robotics and Automation*, vol. 7, no. 3, pp. 320–332, 1991.

- [80] S. T. E. Salcudean, “6-dof magnetically levitated haptic interface.” <http://www.ece.ubc.ca/~tims/maglev.html>.
- [81] T. Nakamura, Y. Kogure, and K. Shimamura, “A micro operation hand and its application to microdrawing,” in *Robotics and Automation, 2000. Proceedings. ICRA’00. IEEE International Conference on*, vol. 2, pp. 1095–1100, IEEE, 2000.
- [82] S. Krishnan and L. Saggere, “A multi-fingered micromechanism for coordinated micro/nano manipulation,” *Journal of Micromechanics and Microengineering*, vol. 17, no. 3, p. 576, 2007.
- [83] D. J. Cappelleri and Z. Fu, “Towards flexible, automated microassembly with caging micromanipulation,” in *Robotics and Automation (ICRA), 2013 IEEE International Conference on*, pp. 1427–1432, IEEE, 2013.
- [84] M. Khamesee and E. Shameli, “Regulation technique for a large gap magnetic field for 3d non-contact manipulation,” *Mechatronics*, vol. 15, no. 9, pp. 1073–1087, 2005.
- [85] H. Nagaraj, “Investigation of magnetic fields and forces arising in open-circuit-type magnetic bearings,” *Tribology Transactions*, vol. 31, no. 2, pp. 192–201, 1988.
- [86] E. Furlani, “A formula for the levitation force between magnetic disks,” *IEEE Transactions on magnetics*, vol. 29, no. 6, pp. 4165–4169, 1993.
- [87] E. Furlani, “Formulas for the force and torque of axial couplings,” *IEEE Transactions on Magnetism*, vol. 29, no. 5, pp. 2295–2301, 1993.
- [88] R. Ravaud, G. Lemarquand, S. Babic, V. Lemarquand, and C. Akyel, “Cylindrical magnets and coils: Fields, forces, and inductances,” *IEEE Transactions on Magnetism*, vol. 46, no. 9, pp. 3585–3590, 2010.

- [89] W. Robertson, B. Cazzolato, and A. Zander, "A simplified force equation for coaxial cylindrical magnets and thin coils," *IEEE Transactions on Magnetics*, vol. 47, no. 8, pp. 2045–2049, 2011.
- [90] W. Robertson, B. Cazzolato, and A. Zander, "Axial force between a thick coil and a cylindrical permanent magnet: Optimizing the geometry of an electromagnetic actuator," *IEEE Transactions on Magnetics*, vol. 48, no. 9, pp. 2479–2487, 2012.
- [91] H. Zhu, C. K. Pang, and T. J. Teo, "Analysis and control of a 6 dof maglev positioning system with characteristics of end-effects and eddy current damping," *Mechatronics*, vol. 47, pp. 183–194, 2017.
- [92] A. Ghosh, T. R. Krishnan, P. Tejaswy, A. Mandal, J. K. Pradhan, and S. Ranasingh, "Design and implementation of a 2-dof pid compensation for magnetic levitation systems," *ISA transactions*, vol. 53, no. 4, pp. 1216–1222, 2014.
- [93] C.-A. Bojan-Dragos, S. Preitl, R.-E. Precup, S. Hergane, E. G. Hughiet, and A.-I. Szedlak-Stinean, "State feedback and proportional-integral-derivative control of a magnetic levitation system," in *Intelligent Systems and Informatics (SISY), 2016 IEEE 14th International Symposium on*, pp. 111–116, IEEE, 2016.
- [94] S. Yadav, S. Verma, and S. Nagar, "Optimized pid controller for magnetic levitation system," *IFAC-PapersOnLine*, vol. 49, no. 1, pp. 778–782, 2016.
- [95] J. Yang, J. Su, S. Li, and X. Yu, "High-order mismatched disturbance compensation for motion control systems via a continuous dynamic sliding-mode approach," *IEEE Transactions on Industrial Informatics*, vol. 10, no. 1, pp. 604–614, 2014.

- [96] N. Boonsatit and C. Pukdeboon, “Adaptive fast terminal sliding mode control of magnetic levitation system,” *Journal of Control, Automation and Electrical Systems*, vol. 27, no. 4, pp. 359–367, 2016.
- [97] D. Ginoya, C. M. Gutte, P. Shendge, and S. Phadke, “State-and-disturbance-observer-based sliding mode control of magnetic levitation systems,” *Transactions of the Institute of Measurement and Control*, vol. 38, no. 6, pp. 751–763, 2016.
- [98] A. Nath, J. Samantaray, and S. Chaudhury, “Magnetic ball levitation system control using sliding mode control and fuzzy pd+ i control: a comparative study,” in *Energy, Power and Environment: Towards Sustainable Growth (ICEPE), 2015 International Conference on*, pp. 1–5, IEEE, 2015.
- [99] P. Korondi, C. Budai, H. Hashimoto, and F. Harashima, “Tensor product model transformation based sliding mode design for lpv systems,” in *Recent Advances in Sliding Modes: From Control to Intelligent Mechatronics*, pp. 277–298, Springer, 2015.
- [100] M. Mehrtash, E. Shameli, and M. B. Khamesee, “Magnetic telemanipulation device with mass uncertainty: Modeling, simulation and testing,” *International Journal of Applied Electromagnetics and Mechanics*, vol. 34, no. 4, pp. 211–223, 2010.
- [101] A. El Hajjaji and M. Ouladsine, “Modeling and nonlinear control of magnetic levitation systems,” *IEEE Transactions on industrial Electronics*, vol. 48, no. 4, pp. 831–838, 2001.
- [102] T. Schuhmann, W. Hofmann, and R. Werner, “Improving operational performance of active magnetic bearings using kalman filter and state feedback control,” *IEEE Transactions on Industrial Electronics*, vol. 59, no. 2, pp. 821–829, 2012.

- [103] H. Wang, X. Zhong, and G. Shen, “Analysis and experimental study on the maglev vehicle-guideway interaction based on the full-state feedback theory,” *Journal of Vibration and Control*, vol. 21, no. 2, pp. 408–416, 2015.
- [104] A. M. Benomair and M. O. Tokhi, “Nonlinear full-order observer-based controller design for active magnetic levitation via lqr-feedback linearisation,” *International Journal of Modelling, Identification and Control*, vol. 26, no. 1, pp. 59–67, 2016.
- [105] I. Ahmad and M. A. Javaid, “Nonlinear model & controller design for magnetic levitation system,” *Recent advances in signal processing, robotics and automation*, pp. 324–328, 2010.
- [106] J. P. Hespanha, *Linear systems theory*. Princeton university press, 2009.
- [107] S. Basovich, S. A. Arogeti, Y. Menaker, and Z. Brand, “Magnetically levitated six-dof precision positioning stage with uncertain payload,” *IEEE/ASME Transactions on Mechatronics*, vol. 21, no. 2, pp. 660–673, 2016.
- [108] C.-M. Lin, M.-H. Lin, and C.-W. Chen, “Sopc-based adaptive pid control system design for magnetic levitation system,” *IEEE Systems journal*, vol. 5, no. 2, pp. 278–287, 2011.
- [109] R. Morales, H. Sira-Ramírez, and V. Feliu, “Adaptive control based on fast online algebraic identification and gpi control for magnetic levitation systems with time-varying input gain,” *International Journal of Control*, vol. 87, no. 8, pp. 1604–1621, 2014.
- [110] Z.-J. Yang, K. Kunitoshi, S. Kanae, and K. Wada, “Adaptive robust output-feedback control of a magnetic levitation system by k-filter approach,” *IEEE transactions on industrial electronics*, vol. 55, no. 1, pp. 390–399, 2008.

- [111] U. Sadek, A. Sarjaš, A. Chowdhury, and R. Svečko, “Improved adaptive fuzzy backstepping control of a magnetic levitation system based on symbiotic organism search,” *Applied Soft Computing*, vol. 56, pp. 19–33, 2017.
- [112] N. Sun, Y. Fang, and H. Chen, “Tracking control for magnetic-suspension systems with online unknown mass identification,” *Control Engineering Practice*, vol. 58, pp. 242–253, 2017.
- [113] X. Zhang and M. B. Khamesee, “Adaptive force tracking control of a magnetically navigated microrobot in uncertain environment,” *IEEE/ASME Transactions on Mechatronics*, vol. 22, no. 4, pp. 1644–1651, 2017.
- [114] M. Valentini, S. Munk-Nielsen, F. V. Sanchez, and U. M. De Estibariz, “A new passive islanding detection method for grid-connected pv inverters,” in *Power Electronics, Electrical Drives, Automation and Motion, 2008. SPEEDAM 2008. International Symposium on*, pp. 223–228, IEEE, 2008.
- [115] K. Vinther, C. H. Lyhne, E. Baasch, H. Rasmussen, *et al.*, “Evaporator superheat control with one temperature sensor using qualitative system knowledge,” in *American Control Conference (ACC), 2012*, pp. 374–379, IEEE, 2012.